Measurement of α_s from scaling violations in fragmentation functions in e^+e^- annihilation [1]

Cristóbal Padilla Aranda
Universitat Autònoma de Barcelona
Institut de Física d'Altes Energies
Edifici C
E-08193 Bellaterra (Barcelona) Spain

September 1995

[1] Ph Dissertation

Contents

List of Figures

List of Tables

Chapter 1

Introduction

The theory of Quantum Chromodynamics (QCD) is a field theory describing the interactions of quarks and gluons. It constitutes the part of the Standard Model of the strong and electroweak interactions, based on a $SU(3) \otimes SU(2) \otimes U(1)$ local gauge symmetry, that describes the strong interactions.

Apart from the tests to confirm SU(3) as the gauge symmetry group of the theory, tests of the theory can be performed comparing different measurements of the only free parameter of the theory: the strong coupling constant, α_s. Its value appears in the description of a very large number of observables like the total e^+e^- annihilation cross section, the hadronic width of the Z boson, the τ lepton lifetime, the jet structure at LEP, etc.

The four LEP experiments have extensively studied the hadronic decays of the Z boson up to now. The strong coupling constant, α_s, has been measured with a lot of different methods giving a precision that is now below 4%. The errors are larger than the typical quoted uncertainties in other Standard Model parameters The reason is the difficulty of performing QCD calculations, both at higher order in perturbation theory and in the non-perturbative regime, where effects due to hadronization are important.

This thesis presents a new test of QCD based on a new measurement of α_s from the study of scaling violations in fragmentation functions. The study of scaling violations in structure functions in deep-inelastic lepton-nucleon scattering played a fundamental role in establishing QCD as the theory of strong interactions.

QCD predicts similar scaling violations in the fragmentation functions of quarks and gluons. In an electron-positron collider this translates into the fact that the distributions of the scaled-energy $x \equiv 2E/\sqrt{s}$ of final state particles in hadronic events depend on the centre-of-mass energy, $\sqrt{s}$. These scaling violations come about because with increasing $\sqrt{s}$ more phase space for gluon radiation and thus final state particle production becomes available, leading to a softer scaled energy distribution. As the probability for gluon radiation is proportional to the strong coupling constant, a measurement of the scaled-energy distributions at different centre-of-mass energies compared to the QCD prediction allows to determine the only free parameter of QCD, α_s.

In principle, variations with energy of the x distributions would establish the existence of scaling violations and allow the determination of α_s. However, the fact that the final state flavour composition depends strongly on the centre-of-mass energy (abundance of u-type quarks at PEP and PETRA energies and majority of d-type quarks at LEP energies), and that the fragmentation functions depend on the quark mass, means that the effect would be biased by differences between fragmentation functions for the different quark flavours. Therefore, in order to disentangle scaling violations arising from gluon radiation from effects due to the changing flavour composition independently of Monte Carlo modeling, final state flavour identification is needed.

Problems come also from the difficulty of measuring the fragmentation functions directly. These fragmentation functions would contain only the particles produced after the fragmentation of the original quarks produced in the e^+e^- annihilation. Instead, the scaled-energy distributions contain particles produced on the decay of the hadrons coming from the fragmentation process. The effect on the scaling violations of considering the particles after fragmentation and decay has to be controlled in order to have a reliable measurement of the strong coupling constant.

Other effects that must be controlled are the corrections that the fragmentation of the quarks (a non-perturbative phenomenon) can induce in the perturbative equations describing the scaling violations.

The work presented here uses inclusive scaled-energy distributions of stable charged particles measured at PEP, PETRA, TRISTAN and LEP together with ALEPH measurements of the distributions in bottom-, charm- and light-quark enriched samples, an inclusive sample, and a gluon jet sample. These data, obtained in 1992 and 1993, correspond to approximately 40 pb^{-1} taken at a centre-of-mass energy around 91.2 GeV. They amount to close to 1.2 million hadronic decays of the Z.

Chapter 2 describes the theoretical framework of the analysis, which is based on the Dokshitzer-Gribov-Lipatov-Altarelli-Parisi (DGLAP) evolution equations with splitting kernels and coefficient functions computed to next-to-leading order. Chapter 3 gives a description of the ALEPH detector, emphasizing the parts of the apparatus used for the analysis. The tracking reconstruction and special flavour tagging algorithms needed for the analysis are described in chapter 4. The measurement of the ALEPH data used in the analysis is described in chapter 5. The Chapter 6 provides a description of the the scaling violations analysis and the results. The final summary and conclusions are given in chapter 7. A list of appendices give some more detailed information on the formulae and data used.

Chapter 2

Theoretical Framework

This chapter describes the necessary ingredients for the analysis of scaling violations of fragmentation functions and the measurement of the strong coupling constant from them. After a brief introduction on the theory of Quantum Chromodynamics with special emphasis in the running coupling constant in section 2.1, section 2.2 describes how the fragmentation functions are related to the measurable scaled energy distributions. This relation is obtained using the mass-factorization procedure, which is also described there. This leads to $\sqrt{s}$ dependent fragmentation functions. The change of these fragmentation with the energy is described by perturbative QCD, and is discussed in section 2.3. This can allow to extract α_s from the measurement of the scaled energy distribution at different energies. Section 2.4 describes some effects that could change the perturbative energy evolution of the fragmentation functions and that have to be taken into account in order to get a reliable measurement of the strong coupling constant. Finally, section 2.5 gives a scheme of the analysis performed to measure the strong coupling constant.

2.1 QCD

The theory of Quantum Chromodynamics was formulated about twenty years ago [1]. It constitutes the part of the Standard Model [2] that describes the strong interactions of coloured spin 1/2 quarks with massless coloured spin 1 gluons.

The fermions of the theory were formally introduced as constituents of mesons and baryons in the Gell-Mann-Zweig model [3]. It was realized that quarks are naturally associated with the pointlike constituents, called partons [4], discovered in deep inelastic lepton-nucleon scattering [5].

The concept of colour [6] was introduced in order to avoid spin statistics problems appearing in baryons made out of three quarks with the same flavour, as the Δ^{++} resonance. Assigning to the quarks a new quantum number, colour, corresponding to a new symmetry, solved this problem. The number of colours was measured from the partial decay width of neutral pions into photons, which is proportional to N_c^2 [7], and from the total hadronic cross section in e^+e^- annihilations, proportional to N_c [8].

The gauge bosons of QCD are called gluons. They were introduced to explain hadrons as dynamically bound quark states. An important fact of QCD is that gluons carry colour charge. Thus, they couple to other gluons, as well as to the quarks. As a consequence, vacuum polarization effects produce an anti-screening of the bare QCD charges, which results in a strong interaction at large distances and weaker at short distances. This explains the fact that quarks are not observed as free particles and leads to the concepts of confinement [9] and asymptotic freedom [10].

2.1.1 QCD lagrangian

The QCD Lagrangian density is the Yang-Mills Lagrangian for an unbroken SU(3) local gauge invariant symmetry. It can be written as

$$\mathcal{L} = -\frac{1}{4} G^a_{\mu\nu} G^{\mu\nu}_a + \overline{q_\alpha}(i \not{D} - \mathbf{m}) q^\alpha + \mathcal{L}^{\mathrm{GF}} + \mathcal{L}^{\mathrm{Ghost}} \tag{2.1}$$

with

$$G^a_{\mu\nu} = \partial_\mu A^a_\mu - \partial_\nu A^a_\nu + g\, f^{abc}\, A^b_\mu\, A^c_\nu \tag{2.2}$$

$$D_\mu = \partial_\mu - ig\, A^a_\mu\, T^a_F. \tag{2.3}$$

$q_\alpha = \{\mathrm{u}_\alpha, \mathrm{d}_\alpha, \mathrm{s}_\alpha, \mathrm{c}_\alpha, \mathrm{b}_\alpha, \mathrm{t}_\alpha\}$ represents the quark fields with colour α, α having N_c (three) degrees of freedom. $\mathbf{m} = \{m_{\mathrm{q}}\}$ represents the quarks masses. A^a_μ is the gluon field, a being the gluon colour index that has $N_c^2 - 1$ (eight) degrees of freedom. f^{abc} are the group structure constants and T^a_F, the N_c-dimension group generators in the fundamental representation. g is a gauge coupling constant related with the strong coupling constant, α_s, through $\alpha_s = g^2/4\pi$.

$\mathcal{L}^{\rm GF}$ and $\mathcal{L}^{\rm Ghost}$ are, respectively, the gauge fixing and ghost terms. The gauge fixing term is included to allow the inversion of the gluon propagator, as in any gauge theory with massless gauge bosons. The ghost term has to be included in non-abelian theories, where the gauge bosons interact among themselves, to cancel non-physical contributions in those diagrams where these interactions appear. They are given by

$$\begin{aligned}
\mathcal{L}^{\rm GF} &= -\frac{1}{2\xi}(\partial^\mu G^a_\mu)\,(\partial^\nu G^a_\nu) &(2.4)\\
\mathcal{L}^{\rm Ghost} &= \partial^\mu \overline{\varphi_a}\,\nabla^\mu_{ab}\varphi^b &(2.5)\\
\nabla^\mu_{ab} &= \delta_{ab}\,\partial^\mu - g\,f_{abc}\,A^\mu_c &(2.6)
\end{aligned}$$

being ξ a gauge fixing constant, which is, for example $\xi = 1$ in the t'Hooft-Feynman gauge and $\xi = 0$ in the Landau gauge, and φ^b massless, hermitian, scalar fields with Fermi-Dirac statistics called ghosts fields.

The Feynman rules deduced from this Lagrangian can be found in any text-book [11]. From them, it can be deduced that the amplitude for a quark changing its colour from α to β by emitting a gluon of type c is proportional to $g(T^c_F)_{\alpha\beta}$, and that the one for a gluon of type a changing to b by emitting a gluon of type c is proportional to gf^{abc}. From these dependences, it can be seen that the group structure constants and generators play an important role in strong interactions and deserve a more careful study.

2.1.2 Group structure and colour factors

The predictions that can be made with the Lagrangian of eq. (2.1) are dependent of the gauge group used to construct it. It is well established that the gauge group of QCD is SU(3). However, it is instructive to formulate the dependence on the group in a more general way.

The structure constants of any group are related to the generators of the group, T^a, through the relation

$$\left[T^a, T^b\right] = i f^{abc}\,T_c. \tag{2.7}$$

Two important representations of the group are the fundamental $(N_F \times N_F) = (N_c \times N_c)$ representation, which, in the case of SU(3) is

$$(T^a_F)_{\alpha\beta} = \frac{\lambda^a_{\alpha\beta}}{2} \tag{2.8}$$

begin λ^a the Gell-Mann matrices, and the adjoint $(N_A \times N_A) = (N_c^2 - 1 \times N_c^2 - 1)$ representation,

$$(T_A^a)_{bc} = -if_{abc}. \tag{2.9}$$

The following relations between the generators of the group can be deduced

$$\mathrm{Tr}\left(T_F^a T_F^b\right) = T_F \delta^{ab} \quad , \quad \mathrm{Tr}\left(T_A^a T_A^b\right) = C_A \delta^{ab} \quad , \quad (T_F^a T_F^a)_{\alpha\beta} = C_F \delta^{\alpha\beta} \tag{2.10}$$

being C_F the Casimir factor of the fundamental (fermion) representation, C_A the Casimir factor of the adjoint (gluon) representation and, T_F the factor that connects both representations through $T_F = N_F C_F / N_A$. They are called 'colour factors' and depend only on the gauge group of the theory. In QCD (SU(3)) they are given by

$$C_F = \frac{N_c^2 - 1}{2N_c} = \frac{4}{3} \quad , \quad C_A = N_c = 3 \quad , \quad T_F = \frac{1}{2}. \tag{2.11}$$

Since a factor C_F frequently appears accompanying the coupling constant α_s, it is common practice to define

$$a = \frac{\alpha_s C_F}{2\pi} \quad , \quad X = \frac{C_A}{C_F} \quad , \quad Z = n_f \frac{T_F}{C_F} \tag{2.12}$$

which are the so-called couplant and the factors that parametrize the gauge structure of the underlying theory. n_f is the number of active flavours, ie., the number of different quarks that can be produced at the energy in which the QCD calculations are being done. Physically, they correspond to the ratio of the gluon-self coupling to the quark-gluon coupling (X) and the ratio of the gluon to $\mathrm{q\overline{q}}$ splitting to the quark-gluon coupling (Z). The two constants have been measured by the four LEP collaborations [12] and found in agreement with the SU(3) structure.

2.1.3 The running coupling constant and RGE

The Lagrangian (2.1) contains only a free parameter: the gauge coupling constant, g, or equivalently, α_s. Supposing this is a small number, perturbation theory can be applied in order to get physical predictions. When this is done, there appear calculations of Feynman diagrams that contain loops which are ultraviolet divergent. These divergences are first regularized [13] and then removed by absorbing them into the redefinition of the physical bare parameters through some renormalization procedure [14].

The renormalization scheme most widely used for QCD calculations is the Modified Minimal Subtraction scheme ($\overline{MS}$). In this scheme, the integrals are regularized following the dimensional regularization procedure computing the integrals in a D dimension space-time with $D = 4 - \epsilon$. In this scheme, when computing the ultraviolet divergences in the space of dimension D, there appear terms of the form

$$\frac{1}{\epsilon} + \ln 4\pi - \gamma_E \tag{2.13}$$

which are divergent when ϵ tends to zero. The $\overline{MS}$ renormalization scheme consists on absorbing the terms in eq. (2.13) into the redefinition of the physical bare parameters. In this procedure, an arbitrary scale, μ, appears in order to conserve the correct dimensions of the Lagrangian of eq. (2.1).

The regularization procedure allows, then, to define renormalized quantities, P, as functions of the unrenormalized ones, P_U, in the form

$$P(\alpha_s, \mathbf{m}, \mu) = Z_P(g_B, \mathbf{m}_B, \mu, \epsilon) \cdot P_U(g_B, \mathbf{m}_B) \tag{2.14}$$

which are finite when the regularization parameter ϵ tends to zero.

In the renormalization procedure, the dependence on the arbitrary parameter μ is introduced. Since any physical quantity must not depend on the value of μ, provided bare parameters $g_B, \mathbf{m}_B$, are kept fixed, the total derivative with respect to μ of eq. (2.14) must be zero:

$$\mu^2 \frac{d}{d\mu^2} P(\alpha_s, \mathbf{m}, \mu)\Big|_{g_B, \mathbf{m}_B} =$$
$$\left[\mu^2 \frac{\partial}{\partial \mu^2} + \beta(\alpha_s(\mu)) \frac{\partial}{\partial \alpha_s} + \sum_i 2\overline{m}_i^2 \gamma_{m_i}(\alpha_s(\mu)) \frac{\partial}{\partial \overline{m}_i^2}\right] P(\alpha_s, \mathbf{m}, \mu)\Big|_{g_B, \mathbf{m}_B} \equiv 0. \tag{2.15}$$

This is the renormalization group equation (RGE). $\overline{m}_i = \overline{m}_i(\mu)$ are the running masses and $\alpha_s(\mu)$ is the running coupling constant. $\gamma_{m_i}(\alpha_s(\mu))$ is the mass anomalous dimension that will determine the functional form of the running masses with the scale μ. It is given by the expression [15]

$$\mu^2 \frac{d\overline{m}_i(\mu)}{d\mu^2}\Big|_{g_B, \mathbf{m}_B} = \overline{m}_i(\mu) \gamma_{m_i}(\alpha_s(\mu)). \tag{2.16}$$

The β-function controls the renormalization scale dependence of α_s through

$$\mu^2 \frac{d\alpha_s(\mu)}{d\mu^2}\Big|_{g_B, \mathbf{m}_B} = \beta(\alpha_s) = -\sum_{i \geq 0} \beta_i \left(\frac{\alpha_s}{\pi}\right)^{i+2}. \tag{2.17}$$

The expansion of (2.17) is known up to three loops [16]. In the analysis, the two first coefficients are needed

$$\beta_0 = \left(11 - \frac{2}{3}n_f\right)\Big/ 4 \quad (2.18)$$

$$\beta_1 = \left(102 - \frac{38}{3}n_f\right)\Big/ 16, \quad (2.19)$$

which turn out to be independent of the regularization scheme used. These expressions and eq. (2.17) allow to write an explicit solution for the running of α_s:

$$\alpha_s(\sqrt{s}) = \frac{\alpha_s(\mu)}{w}\left(1 - \frac{\beta_1}{\beta_0}\frac{\alpha_s(\mu)}{4\pi}\frac{\ln w}{w}\right) \quad (2.20)$$

with

$$w = 1 - \beta_0 \frac{\alpha_s(\mu)}{4\pi}\ln\frac{\mu^2}{s}, \quad (2.21)$$

which is exact to leading and next-to-leading logarithm accuracy, i.e. it contains all terms of the full solution of the type $\alpha_s^n(\mu)\ln^m(\mu^2/s)$ with $m = n-1, n-2$.

The scale Λ at which the strong coupling constant becomes infinite is implicitly defined as

$$\alpha_s(\mu) = \frac{4\pi}{\beta_0 L}\left(1 - \frac{\beta_1}{\beta_0}\frac{\ln L}{L}\right) \quad (2.22)$$

with

$$L = \ln\frac{\mu^2}{\Lambda^2}. \quad (2.23)$$

Equation (2.22) is renormalization scheme independent. However, the expressions for the physical cross-sections are scheme dependent, and therefore, the fitted value of Λ depends on the renormalization scheme.

In this analysis of scaling violations, a representation is chosen that expresses the running couplant, $a(s)$, as a function of the strong couplant at a reference scale, M_Z, through

$$a(s) = \frac{a(M_Z^2)}{w}\left(1 - a(M_Z^2)\frac{b_1}{b_0}\frac{\ln w}{w}\right) \quad (2.24)$$

with

$$w = 1 - a(M_Z^2) b_0 \ln(\frac{M_Z^2}{s}) \quad (2.25)$$

where

$$b_0 = \frac{2}{C_F}\beta_0 \quad \text{and} \quad b_1 = \left(\frac{2}{C_F}\right)^2 \beta_1. \quad (2.26)$$

2.2 Scaled energy distributions

The single inclusive particle spectrum produced in the process $e^+e^- \to$ hadrons can be written as a sum of a 'transverse' (T), a 'longitudinal' (L) and an 'asymmetric' (A) cross section:

$$\frac{d^2\sigma(s)}{dx\, d\cos\theta} = \frac{3}{8}(1+\cos^2\theta)\frac{d\sigma^T(s)}{dx} + \frac{3}{4}\sin^2\theta\frac{d\sigma^L(s)}{dx} + \frac{3}{4}\cos\theta\frac{d\sigma^A(s)}{dx} \tag{2.27}$$

Here θ is the polar angle of the produced particle with respect to the beam direction. The Lorentz-invariant variable x is defined through $x = 2(k\cdot Q)/(Q\cdot Q)$ where k is the 4-momentum of the produced hadron and Q the 4-momentum of the virtual photon or Z. In the centre-of-mass frame of the collision (which is the laboratory frame of an e^+e^- collider if initial state radiation can be neglected) it reduces to $x = E/E_{beam}$.

The first term, proportional to $(1+\cos^2\theta)$, has its origin in fragmentation of the original quarks while the second one would not be present in a theory without gluon radiation. A physical insight on their origin can be given considering the initial and final spin states. In high energy e^+e^- annihilation, the electron and positron spins are oriented along the beam line in such a way that the system is in a state of angular momentum of the form $|J, J_z> = |1, \pm 1>$ corresponding to the transverse polarizations of the virtual boson formed in the collision. Then, two particles are emitted forming an angle θ with the beam line in a state of angular momentum characterized by $|J, J_{z'}> = |1, \pm 1>$, where z' is the axis defined by the direction of the outgoing particles. The transition amplitude for this event to happen is then proportional to

$$<1, \pm 1|e^{-i\theta J_y}|1, \pm 1> = d^1_{\pm 1, \pm 1} = \frac{1}{2}(1 \pm \cos\theta) \tag{2.28}$$

which, averaging its square over the initial states, gives the expected angular behaviour. If now, a gluon (of spin 1) is radiated from one of the outgoing quarks, the final state could be characterized by $|J, J_{z'}> = |1, 0>$, thus giving terms proportional to

$$d^1_{0,\pm 1} = \pm\frac{\sin\theta}{\sqrt{2}}, \tag{2.29}$$

which are the ones appearing in the longitudinal term in eq. (2.27).

The third term, proportional to $\cos\theta$, has its origin in parity-violating terms that will not be used in this analysis.

Integration over $\cos\theta$ of eq. (2.27) yields the scaled energy spectrum.

$$\frac{1}{\sigma_{\rm tot}}\frac{d\sigma(s)}{dx} = \frac{1}{\sigma_{\rm tot}}\frac{d\sigma^T(s)}{dx} + \frac{1}{\sigma_{\rm tot}}\frac{d\sigma^L(s)}{dx}, \tag{2.30}$$

which carries most of the weight in this analysis of scaling violations.

2.2.1 Fragmentation functions

In perturbative QCD, an expression can be computed for the transverse and longitudinal cross-sections. In the naive parton model, the transverse differential cross-sections is given by

$$\frac{d\sigma^T(s)}{dx} = 2\sigma_0(s)\cdot \sum_{i={\rm u,d,s,c,b}} w_i(s)\,\mathcal{D}_{0,i}(x) \tag{2.31}$$

and the longitudinal cross-section is zero. In eq. (2.31), $\sigma_0(s)$ is the Born cross section at a centre-of-mass energy $\sqrt{s}\equiv Q$, $w_i(s)$ are the relative electro-weak cross sections for the production of primary quarks of type i, given in appendix A, and $\mathcal{D}_{0,i}(x)$ are the bare fragmentation functions that give the probability of having a hadron of fractional beam energy x coming from the fragmentation of a quark or an antiquark q_i and defined as the mean of the fragmentation function of a quark and an antiquark of the same flavour, as

$$\mathcal{D}_{0,i}(x) = \frac{1}{2}\left(\mathrm{q_i}(x) + \overline{\mathrm{q}}_{\mathrm{i}}(x)\right). \tag{2.32}$$

The fact that the total energy carried out by all fragments is equal to that of the original parton implies the following sum rule for the bare fragmentation functions

$$\int_0^1 dx\, x\,\mathcal{D}_{0,i}(x) = 1. \tag{2.33}$$

Proceeding beyond the zeroth order in α_s, before the quark fragments into the hadron, it can radiate a gluon. Therefore, the differential probability that a parton with scaled energy between z and $z+dz$ is produced, and then fragments to a hadron with scaled energy between y and $y+dy$ can be written as

$$\left(\frac{d\sigma_{\rm q}^{T,L}}{dz}(s)\right) dz\,\mathcal{D}_{0,\rm q}(y)\,dy + \left(\frac{d\sigma_g^{T,L}}{dz}(s)\right) dz\,\mathcal{D}_{0,g}(y)\,dy \tag{2.34}$$

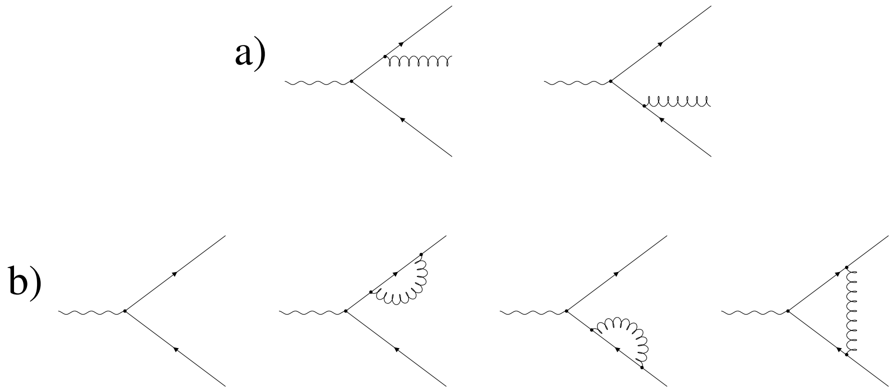

Figure 2.1: Feynman graphs for the parton subprocess $Z \to q\overline{q}g$. The two real gluon emission diagrams (a), and the virtual corrections (b) have to be added.

where $(d\sigma^{T,L}_{q(g)}/dz(s))dz$ is the probability of finding a quark (gluon) with energy

$$E_{q(g)} = \frac{1}{2}z\sqrt{s} \tag{2.35}$$

in an angular momentum final state $|1, \pm 1>$ (transverse) or $|1, 0>$ (longitudinal), and $\mathcal{D}_{0,q(g)}(y)\,dy$ is the probability that this quark (gluon) fragments into a hadron carrying fractional energy

$$y = E_h/E_{q(g)}. \tag{2.36}$$

The integration of eq. (2.34) over the internal variables results in the scaled energy distributions of eq. (2.30):

$$\frac{d\sigma^{T,L}}{dx}(s) = \int_0^1 dz \int_0^1 dy\, \delta(x - yz) \cdot \left[\frac{d\sigma^{T,L}_{q}}{dz}(s)\mathcal{D}_{0,q}(y) + \frac{d\sigma^{T,L}_{g}}{dz}(s)\mathcal{D}_{0,g}(y)\right]. \tag{2.37}$$

The experimental variable, x, is related to the two inside parton variables through

$$y = x/z. \tag{2.38}$$

The cross sections for the production of real quarks or gluons are given by the Feynman diagrams of figure 2.1(a). Their calculation contains infrared or soft divergences, and collinear or mass singularities. The first ones occur when the energy of the emitted gluon goes to zero. The second ones occur when the gluon is emitted parallel to the quark, ie., the mass of the quark tends to zero. The virtual diagrams of figure 2.1(b) contain, on top, ultraviolet divergences that cancel after renormalization. However, some infrared divergences and mass singularities remain. All the divergences will cancel when the total cross-section is computed (the integral over x of the scaled energy distribution), but the differential cross-section of eq. (2.37) leads to a functional form

$$\begin{aligned} \frac{d\sigma^{T,L}}{dx}(s) &= 2\sigma_0(s)\int_x^1 \frac{dz}{z}\sum_{i=\mathrm{u,d,s,c,b}} w_i(s)\mathcal{D}_{0,i}\left(\frac{x}{z}\right)\cdot \\ & \left[\delta(1-z)+\frac{\alpha_s}{2\pi}R_q^{T,L}(z)\ln\left(\frac{s}{m^2}\right)+\alpha_s f_{\mathrm{q}}^{T,L}(z)\right] + \text{Gluon terms} \end{aligned} \tag{2.39}$$

where the contribution coming from the gluon fragmentation functions is not specified for simplicity. m is a scale that appears in the regularization of the mass singularities.

The coefficient accompanying the logarithmic part does not depend on the regularization scheme used but the f_{q} functions do. Moreover, the formula is not only regularization scheme dependent but is also divergent as $m \to 0$. Since the cross-section is a measurable quantity, the bare fragmentation functions, which cannot be measured, should have some mass dependence that cancels the mass singularities.

The way to solve the problem consists in factorizing all the mass singularities in a redefinition of the fragmentation functions, which then become

$$\begin{aligned} D_i(z,\mu_F^2) &= \int_z^1 \frac{dy}{y}\mathcal{D}_{0,i}\left(\frac{z}{y}\right)\cdot \\ & \left[\delta(1-y)+\frac{\alpha_s}{2\pi}R_{\mathrm{q}}^{T,L}(y)\ln\left(\frac{\mu_F^2}{m^2}\right)+\alpha_s g_{\mathrm{q}}^{T,L}(y)\right] \end{aligned} \tag{2.40}$$

and are scale dependent. $D_i(z,\mu_F^2)$ are called the effective fragmentation functions. Introducing the expression (2.40) into eq. (2.39) gives

$$\begin{aligned} \frac{d\sigma^{T,L}(s)}{dx} &= 2\sigma_0(s)\int_x^1 \frac{dz}{z}\cdot\sum_{i=\mathrm{u,d,s,c,b}} w_i(s)\,D_i(x/z,\mu_F^2)\cdot \\ & \left[\delta(1-z)+\alpha_s c_{1\mathrm{q}}^{T,L}(z,\alpha_s,\mu_F^2/s)\right] + \text{Gluon terms} \end{aligned} \tag{2.41}$$

where $c_{1\mathrm{q}}^{T,L}$ is defined as

$$c_{1\mathrm{q}}^{T,L}(z,\alpha_s,\mu_F^2/s) = f_{\mathrm{q}}^{T,L}(z) - g_{\mathrm{q}}^{T,L}(z) - \frac{1}{2\pi}R_{\mathrm{q}}^{T,L}(z)\ln\left(\frac{\mu_F^2}{s}\right) \tag{2.42}$$

and contains all the non-divergent terms that have not been absorbed in the definition of the effective fragmentation functions. This procedure is called mass factorization and its validity is ensured by the general factorization theorem [17]. The separation of the singular part in eq. (2.39) from the remaining finite part takes place at a factorization scale, μ_F, which relates the short distance ('partonic') to the long distance ('hadronic') effects. The functional form of the $c_{1\mathrm{q}}^{T,L}(z, \alpha_s, \mu_F^2/s)$ depends on the factorization scheme adopted and the regularization procedure used to control the infrared divergences.

After the inclusion of the gluon terms in eq. (2.39) and absorbing the $\delta(1-z)$ of eq. (2.41) into the redefinition of the so-called coefficient functions, $C_{\mathrm{q}}^{T,L}$, the transverse and longitudinal cross-section have the general form

$$\begin{aligned} \frac{d\sigma^{T,L}(s)}{dx} &= 2\sigma_0(s)\int_x^1 \frac{dz}{z} C_{\mathrm{q}}^{T,L}(z, \alpha_s(\mu_F), \mu_F^2/s) \sum_{i=\mathrm{u,d,s,c,b}} w_i(s)\, D_i(x/z, \mu_F^2) \\ &+ 2\sigma_0(s)\int_x^1 \frac{dz}{z} C_g^{T,L}(z, \alpha_s(\mu_F), \mu_F^2/s)\, D_g(x/z, \mu_F^2)\ . \end{aligned} \tag{2.43}$$

Formula (2.43) reduces to the parton model formula, (2.31), at first order. The coefficient functions have been computed up to next-to-leading order and their expressions are given in section B.1 in appendix B for the factorization scheme used in this analysis. In first order, the only one not equal to zero is $C_{\mathrm{q}}^T = \delta(1-z)$.

Since what is usually measured is the scaled energy distribution, $1/\sigma_{\mathrm{tot}} d\sigma/dx$, expression (2.43) will contain the ratio of the total cross section, σ_{tot}, to the Born cross section, σ_0. This can be computed with the explicit expressions for the coefficient functions and integrating the differential cross-sections (2.43). Up to first order in α_s, the integrals give

$$\sigma_T = \sigma_0 \quad , \quad \sigma_L = \frac{\alpha_s}{\pi}\sigma_0. \tag{2.44}$$

Thus, the ratio of the two cross sections is given by

$$\frac{\sigma_{\mathrm{tot}}}{\sigma_0} = 1 + \frac{3}{2}\frac{\alpha_s}{2\pi}C_F = 1 + \frac{3}{2}a. \tag{2.45}$$

Equations (2.44) and (2.45) show that, up to first order in α_s, the total correction to σ_{tot} comes only from the longitudinal cross section. Higher orders have been computed for the α_s corrections to the total cross section [18], but not the contributions of the transverse and longitudinal cross sections separately.

2.3 Evolution of the fragmentation functions

Although the effective fragmentation functions cannot be computed perturbatively, their change with energy is predicted in perturbative QCD. Equation (2.40) already suggests a logarithmic dependence with some energy scale. The change of the effective fragmentation functions with energy is governed by the Dokshitzer-Gribov-Lipatov-Altarelli-Parisi (DGLAP) evolution equations [19] that can be written as

$$\frac{dD_j(x,s)}{d\ln s} = \sum_{i=\mathrm{u,d,s,c,b},g} \int_x^1 \frac{dz}{z} P_{ij}(z, \alpha_s(\mu_R), \mu_R^2/s)\, D_i(x/z, s)\,, \tag{2.46}$$

where the splitting kernels P_{ij} are known to next-to-leading order accuracy

$$P_{ij}(x, \alpha_s(\mu_R), \mu_R^2/s) = \frac{\alpha_s(\mu_R)}{2\pi} P_{ij}^{(0)}(x) + \left(\frac{\alpha_s(\mu_R)}{2\pi}\right)^2 P_{ij}^{(1)}(x, \frac{\mu_R^2}{s}) \tag{2.47}$$

The renormalization scale, μ_R, relates the splitting functions at a given scale $\sqrt{s}$ to the strong coupling constant at the renormalization point μ_R. The indices i, j run over all active quark flavours and the gluon. Equation (2.46) shows that the logarithmic energy change in the effective fragmentation functions is due to processes in which a quark or a gluon (partons) with a given scaled energy higher than x (the scaled energy of the observed hadron) radiate becoming another parton of fractional energy z (the probability of this being proportional to the corresponding splitting kernel) that afterwards fragments into the hadron. The probability of the last fragmentation is given by the probability of having a hadron of scaled energy x in a jet of energy $z \cdot E_{\mathrm{beam}}$. The integral takes into account all the cases with $z > x$.

Up to first order in α_s, the dependence on $\ln s$ of the quark fragmentation functions is due to two processes: the quarks can radiate a gluon and then fragment; or they can radiate a gluon which then fragments to the hadron. Analogously, the change in the gluon fragmentation function can be due to the gluon that produces two quarks that then fragment, or it can produce two gluons which then fragment to the observed hadrons. Since in the expression (2.43) for the measurable cross sections, the gluon fragmentation function enters to order α_s, the change of the gluon fragmentation function is already next-to-leading order.

In higher order, other possibilities arise. A quark can split into a quark of a different flavour, or to an antiquark of the same or different flavour before the fragmentation takes place.

The evolution equations resum all the leading logarithmic terms of the solution of the fragmentation functions. Thus, they contain all the diagrams with any number of single gluon emission and before the fragmentation takes place. These diagrams are called ladder diagrams.

It is most convenient to write the coupled system of evolution equations in (2.46) in terms of singlet and non-singlet parts defined as

$$S(x,s) = \frac{1}{n_f} \cdot \sum_{i=\mathrm{u,d,s,c,b}} x\, D_i(x,s) \quad \text{and} \quad N_i(x,s) = x\, D_i(x,s) - S(x,s) \tag{2.48}$$

where the singlet and non-singlet components have been defined with the x-weighted particle spectra. This definition, which slightly deviates from common practice, results in a less singular behaviour for $x \to 0$. The evolution equations then become

$$s\frac{d}{ds}N_i(x,s) = \int_x^1 dz P_N(z, \alpha_s(\mu_R), \mu_R^2/s)\, N_i(\frac{x}{z}, s) \tag{2.49}$$

for the non-singlet components, while the energy evolution of the singlet components is described by the coupled system

$$\begin{aligned} s\frac{d}{ds}G(x,s) &= \int_x^1 dz \left[P_{GG}(z,s,\mu_R)G(\frac{x}{z},s) + P_{GQ}(z,s,\mu_R)S(\frac{x}{z},s)\right] \\ s\frac{d}{ds}S(x,s) &= \int_x^1 dz \left[P_{QG}(z,s,\mu_R)G(\frac{x}{z},s) + P_{QQ}(z,s,\mu_R)S(\frac{x}{z},s)\right] \end{aligned} \tag{2.50}$$

where $G(x,s) \equiv x\, D_G(x,s)$ is used. The terms containing P_{QQ} and P_{GG} are called the diagonal parts, and P_{GQ} and P_{QG}, the off-diagonal parts. The expressions of the splitting kernels used in the analysis are given in section B.2 in appendix B.

2.4 Power-law corrections

The theory described in section 2.3 concerning the energy evolution of the fragmentation functions is not complete. All the equations were developed with the assumption of zero quark mass. Also, the coefficient functions of eq. (2.43) given in the appendix B are deduced with this hypothesis. This may not be a good approximation, at least for charm and bottom quarks, and the effects of their masses in the change of the functional form of the effective fragmentation with the energy could induce some corrections that should be controlled. The fact that the theory describes energy evolution of scaled-energy distributions and that what is usually measured is the scaled-momentum distributions can also produce some corrections.

The fragmentation functions have been defined after the fragmentation stage. It is known that heavy flavour quarks fragment in a heavy hadron that carries most of the initial quark momentum and some light hadrons that share the rest of the initial momentum. This would produce a hard fragmentation function that, after decay, would finally give the softer observed fragmentation function for these flavours. The decay step is not governed by QCD and it should not be considered in the scaling violations analysis. Since the fragmentation functions before the decay are not easy to measure, it is necessary to work with some redefined fragmentation functions that include the decay of the heavy hadrons. The fact that the energy evolution is made in the final fragmentation function is only a practical matter and, again, the effects should be studied and controlled.

Finally the fragmentation itself is a non-perturbative phenomena. Therefore, there can be non-perturbative corrections to the energy evolution of the fragmentation functions. This is a less known effect that has to be parametrized somehow.

2.4.1 Kinematic corrections

The simplest power-law correction appears when the momentum fraction, $x_p = 2p/\sqrt{s}$, of the charged particle is used instead of the energy fraction, $x_E = 2E/\sqrt{s}$. The relation between the two approaches is given by

$$x_E = x_p + \frac{2m^2}{x_p s} + \mathcal{O}(1/s^2). \tag{2.51}$$

The largest corrections come from considering the minimum values of x and energies in the analysis. However, even for values of $x_p \sim 0.1$, which are the lowest values used, and for $\sqrt{s} = 22\,\mathrm{GeV}$ and taking m as the mass of the proton, the correction is not larger than the bin width of the distributions measured by the experiments. For any other values of m and x_p used in the analysis, the correction would be substantially smaller than the bin width. Thus, this correction is believed to be small for the range of values of x_p and centre-of-mass energies used in the analysis.

2.4.2 Heavy quark masses

The coefficient functions and splitting kernels presented in section 2.2 assumed no mass for the quark production and fragmentation. This is a good approximation for the light quarks, but for heavy quarks, and especially for the b quark fragmentation, this could not be the case.

In case the masses of the quarks are considered, the coefficient functions have to be recomputed. In [20] a full list of all the coefficient functions up to order α_s is given.

As an example, the coefficient function C_g^L is modified to

$$\begin{aligned} C_g^L(z,\alpha_s(\mu_F),\mu_F^2/s) &= \frac{a(\mu_F)}{2\sigma_0(s)}\cdot\left\{\sigma^{(a)}(s)\left[\rho\frac{\rho+z^2+2z-4}{z}\ln\frac{1+\beta_z}{1-\beta_z}\right.\right. \\ &\qquad \left. +2\beta_z(2+\rho)\frac{1-z}{z}\right] \\ &\qquad \left.+\sigma^{(v)}(s)\left[-\frac{2\rho}{z}\ln\frac{1+\beta_z}{1-\beta_z}+4\beta_z\frac{1-z}{z}\right]\right\} \end{aligned} \tag{2.52}$$

where $\beta_z = \sqrt{1-\rho/(1-z)}$ and $\rho = 4m^2/s$ being m the mass of the heavy quark, and $\sigma^{(v),(a)}(s)$ the vector and axial contributions to the electroweak Born cross section (appendix A). When the mass is set to zero, $\rho \to 0$ and $\beta_z \to 1$, and expression (2.52) reduces to the one given in eq. (B.1).

From eq. (2.52) it can be seen that all the corrections coming from using the zero-mass coefficient functions instead of eq. (2.52) are of order ρ, that is, at least $\mathcal{O}(m^2/s)$. Thus, these corrections are expected to be small. Since they can be reabsorbed into the definition of the fragmentation functions at one energy, they only affect the evolution process.

The expressions for the other coefficient functions can be found in [20]. The conclusion that the corrections goes as m^2/s also holds for the rest of coefficient functions. Thus, in the analysis of scaling violation, the coefficient functions given in appendix B, which assume zero quark mass, are going to be used for all the quark flavours and the remaining differences will be included in a global parametrization of the power-law corrections.

2.4.3 Heavy quark decays

The evolution equations will be applied to the total fragmentation functions, after decay of the heavy hadrons. The corrections resulting from the use of these fragmentation functions instead of the ones that would result from the quark fragmentation alone, before decay, are described in this section.

The probability of finding a particle with scaled energy x after fragmentation and decay of a quark is defined by

$$T_i(x,s) = \int_0^1 D_i(y,s)dy \int_0^1 \varphi_i(z,s)dz \cdot \delta(x-yz), \tag{2.53}$$

where $\varphi_i(z,s)$ is the energy distribution of the decay products scaled to the energy of the parent hadron. $x = 2E_d/\sqrt{s}$ is the fractional energy of the final decay product, $y = 2E_h/\sqrt{s}$ is the fractional energy taken by the hadron right after fragmentation, and $z = E_d/E_h = x/y$. The index i refers to the different quark species. The total fragmentation function is then given by

$$T_i(x,s) = \int_x^1 \frac{dy}{y}\, D_i(y,s)\, \varphi_i\left(\frac{x}{y},s\right). \tag{2.54}$$

The evolution equations hold for the fragmentation functions $D_i(y,s)$. But the measured cross sections are related with $T_i(x,s)$. The derivative of the latter with respect to $\ln s$ can be decomposed in two terms

$$\frac{\partial T_i(x,s)}{\partial \ln s} = A + B, \tag{2.55}$$

with the following definitions

$$A \equiv \int_x^1 \frac{dy}{y}\, \varphi_i\left(\frac{x}{y},s\right) \frac{\partial D_i(y,s)}{\partial \ln s} \tag{2.56}$$

$$B \equiv \int_x^1 \frac{dy}{y}\, D_i(y,s)\, \frac{\partial \varphi_i(x/y,s)}{\partial \ln s}. \tag{2.57}$$

The evolution equations can be applied to A, which can be written as

$$A = \int_x^1 \frac{dy}{y}\, \varphi_i\left(\frac{x}{y},s\right) \sum_j \int_y^1 \frac{dz}{z}\, P_{ij}(z,\alpha_s(\mu_R),\mu_R^2/s)\, D_j\left(\frac{y}{z},s\right). \tag{2.58}$$

Delta and step functions can be introduced in (2.58) and the order of integration can be exchanged in such a way that A can be written as

$$\begin{aligned} A &= \sum_j \int_x^1 \frac{dz}{z}\, P_{ij}(z,\alpha_s(\mu_R),\mu_R^2/s) \int_{x/z}^1 \frac{d\eta}{\eta}\, D_j(\eta,s)\, \varphi_j\left(\frac{x/z}{\eta}\right) \\ &= \sum_j \int_x^1 \frac{dz}{z} P_{ij}(z,\alpha_s(\mu_R),\mu_R^2/s)\, T_j\left(\frac{x}{z},s\right). \end{aligned} \tag{2.59}$$

The left side of (2.55) together with the result in (2.59) have the same structure as the DGLAP evolution equations applied to the total fragmentation functions,

T_i. Thus, the term in B would constitute a non-QCD correction to the evolution equations coming from the decay effects included in T_i. The B term contains a derivative of the decay function, φ_i, which can be written as

$$\int d\xi\, \delta\left(\xi - \frac{x}{y}\right)\, \frac{\partial \varphi_i(\xi, s)}{\partial \ln s}. \tag{2.60}$$

The decay spectrum, $\varphi_i(\xi, s)$, can be computed as the Lorentz boost of the rest frame spectrum, $\Phi_i(E^\star)$. If $E^\star$ is the energy of the decay product in the heavy hadron rest frame and $\Theta^\star$ the angle of the decay particle with respect to the line of flight of the heavy hadron in the centre-of-mass frame, the observed energy of the decay product can be written as

$$E = \frac{1}{2}\xi\sqrt{s} = \gamma\, E^\star\,(1 + \beta\cos\Theta^\star), \tag{2.61}$$

where $\gamma = E_h/m$ and $\beta = \sqrt{1 - 1/\gamma^2}$, being E_h and m the energy and mass of the heavy hadron, respectively. This allows to write φ_i as

$$\begin{aligned} \varphi_i(\xi, s) \;\; &= \;\; \int d\cos\Theta^\star\, \theta(1 - \cos\Theta^\star)\, \theta(\cos\Theta^\star + 1)\cdot \\ &\quad\;\; \int dE^\star\, \Phi_i(E^\star)\, \delta\left[\xi - 2\frac{\gamma E^\star}{\sqrt{s}}(1 + \beta\cos\Theta^\star)\right], \end{aligned} \tag{2.62}$$

which can be integrated over $\cos\Theta^\star$ to finally have the following expression:

$$\frac{\partial \varphi_i(x/y, s)}{\partial \ln s} = \frac{\partial}{\partial \ln s}\int_{E/\alpha}^{E\alpha} \frac{dE^\star}{E^\star}\Phi_i(E^\star)\frac{\sqrt{s}}{2}\frac{1}{\gamma\beta} \tag{2.63}$$

where α is defined as

$$\alpha = \sqrt{\frac{1+\beta}{1-\beta}}. \tag{2.64}$$

The amount of correction can be explicitly obtained if a decay to two particles is considered. In this case, eq. (2.63) can be simplified so that B from eq. (2.57) can be written as:

$$B = \int_x^1 \frac{dy}{y}\, D_i(y, s) s \frac{\partial}{\partial s}\left[\frac{2}{y}\left(1 - \frac{4m^2}{y^2 s}\right)^{-1/2}\right] \tag{2.65}$$

whose first term is of order m^2/s.

In [20], a different approach based in the moments of the total fragmentation functions arrives to the same conclusion, ie., that the power-law correction coming from the decay of heavy hadrons is of order m^2/s. At LEP energies, for example, this correction is of the order of 0.2% multiplied by the fraction of $\mathrm{b\overline{b}}$.

2.4.4 Hadronization effects

The hadronization effects are the least well known effects in the evolution. They have not been computed explicitly for the fragmentation functions neither for their evolution. In deep-inelastic scattering, they are known to go as $1/Q^2$ [21]. However, no clear statement on their dependence with Q has been given for the case of e^+e^- collisions.

Nevertheless, the fact that corrections to the thrust and sphericity variables have been shown to go as $1/Q \equiv 1/\sqrt{s}$ [22, 23], suggests that the corrections to the evolution of the fragmentation functions could also follow the same behaviour.

A simple hadronization model can help to have an insight in this hypothesis. The model [20] is given by a colour-connected pair of partons that produces light hadrons which occupy a tube in (y, p_t)-space, being y and p_t the rapidity and the transverse momentum of the produced hadrons with respect to the line in which the partons move away. Defining $\rho(p_t)$ as the density of hadrons in the (y, p_t)-space, the energy and momentum of a tube of length Y is given by

$$E = \int_0^Y dy\, d^2p_t\, \rho(p_t)\, p_t \cosh y = \lambda \sinh Y \tag{2.66}$$

$$P = \int_0^Y dy\, d^2p_t\, \rho(p_t)\, p_t \sinh y = \lambda(\cosh Y - 1) \sim E - \lambda \tag{2.67}$$

where

$$\lambda = \int d^2p_t\, \rho(p_t)\, p_t. \tag{2.68}$$

sets the hadronization scale.

The momentum of the system receives a correction of order $\lambda/E = 2\lambda/\sqrt{s}$. Thus, it is expected that the hadronization process introduces corrections of the order $1/\sqrt{s}$.

The hadronization corrections have not been explicitly computed for the evolution of the fragmentation functions. Their dependence with the energy is supported by some arguments as the one explained above. Thus, they have to be parametrized in the analysis. This parametrization will be explained in section 6.4.

2.5 Measurement of the strong coupling constant

In section 2.3, it has been shown that the effective fragmentation functions evolve with the energy in a way that is predictable by perturbative QCD. This evolution depends on α_s. Therefore, data at different centre-of-mass energies can be used to extract a value of the strong coupling constant in an analogous way as it is done in deep-inelastic scattering with the structure functions, which evolve following analogous evolution equations as the fragmentation functions in e^+e^- annihilation.

Schematically, a QCD test based on measurements of inclusive cross sections at different centre-of-mass energies, can be visualized as shown in figure 2.2. Assuming a given set of fragmentation functions is specified at an initial factorization scale μ_i, perturbative QCD relates those fragmentation functions to an observable cross section through eq. (2.43) which, after inclusion of the non-perturbative power-law corrections, can be compared with experimental data (horizontal arrows). The natural choice is $\mu_i = \sqrt{s_i}$ and $\mu_f = \sqrt{s_f}$. Since the fragmentation functions are not calculable in perturbative QCD they can be adjusted such that the theoretical prediction agrees with the data at a given energy. However, having once fixed the initial conditions, a QCD test can be performed by comparing the QCD prediction for various centre-of-mass energies to actual measurements. The energy evolution (vertical arrows) of the fragmentation functions is described by perturbative QCD through eq. (2.46). Here the renormalization scale μ_R appears, i.e. the energy variation of the fragmentation functions at the scale μ is expressed as function of μ and the renormalization point μ_R. The natural choice is $\mu_R = \mu$.

An important fact in the scheme presented is that there are evolution equations

$$
\begin{array}{ccccccccc}
\text{Input} & & & & & & \text{Measurement at } E_{cm} = \sqrt{s_i} & & \\
D(x,\mu_i^2) & \rightarrow & \mathrm{QCD}(\mu_i^2, s_i) & \rightarrow & \dfrac{d\sigma(s_i)}{dx} & \rightarrow & \mathrm{NP-terms} & \rightarrow & \dfrac{d\sigma(s_i)}{dx_e} \\
\downarrow & & & & & & & & \\
\mathrm{QCD}(\mu^2, \mu_R^2) & & & & & & & & \\
\downarrow & & & & & & \text{Measurement at } E_{cm} = \sqrt{s_f} & & \\
D(x,\mu_f^2) & \rightarrow & \mathrm{QCD}(\mu_f^2, s_f) & \rightarrow & \dfrac{d\sigma(s_f)}{dx} & \rightarrow & \mathrm{NP-terms} & \rightarrow & \dfrac{d\sigma(s_f)}{dx_e}
\end{array}
$$

Figure 2.2: Scheme of the scaling violations analysis

for fragmentation functions corresponding to each flavour and the gluon, and none of them have been isolated so far at any energy. In fact, they cannot be measured directly, but their value should be inferred from their relation to the measurable cross-sections as described above. The measurement of the fragmentation function for each flavour would have little importance if flavour composition would be the same at all the energies. But this is not the case as it is shown in figure A.1. Since the b quark fragmentation function is softer than the ones from the other flavours and the fraction of b quarks is larger at LEP, a softer scaled energy distribution would be measured at LEP even in the absence of QCD effects. This means that flavour-tagged distributions are needed, at least at one centre-of-mass energy, to fix the fragmentation function for different quark species and disentangle this effect from the QCD scaling violations.

Also, the measurement of the gluon fragmentation function is needed since it enters in the evolution equations at next-to-leading order level. A direct measurement of the gluon fragmentation function can be obtained from three-jet events, where jets from well separated gluons are tagged by default when the other two jets contain long-lived particles. Additional information on the gluon fragmentation function can be extracted from the longitudinal and transverse cross sections which are related to the gluon fragmentation function according to [20]

$$\frac{1}{\sigma_{\text{tot}}}\frac{d\sigma^L}{dx} = \frac{\alpha_s}{2\pi}\int_x^1 \frac{dz}{z}\left[\frac{1}{\sigma_{\text{tot}}}\frac{d\sigma^T}{dz} + 4\left(\frac{z}{x}-1\right)D_g(z)\right] + \mathcal{O}(\alpha_s^2), \tag{2.69}$$

with has yet uncalculated terms $\mathcal{O}(\alpha_s^2)$. Truncating the above expression at $\mathcal{O}(\alpha_s)$, the parameter α_s becomes an effective leading-order coupling constant which must not be confused with the next-to-leading order running coupling constant appearing in eqs. (2.43), (2.46). Because of this, it will be referred to as β_s in the following.

The measurement of all distributions needed for the analysis of scaling violations will be described in chapter 5. The following two chapters present the detector, and the main tools and algorithms needed to perform the measurement of the scaled energy distributions for different flavour enriched samples.

Chapter 3

The ALEPH detector

The ALEPH detector [24, 25] (ALEPH:'Apparatus for LEP PHysics') is one of the four large detectors installed in the LEP accelerator. The other three are DELPHI [26], L3 [27], and OPAL [28]. It was designed to study in detail the parameters of the Standard Electroweak model, to test QCD at large Q^2 and to search for new physics (such as the top quark, the Higgs boson or supersymmetric particles) in the e^+e^- interactions that take place in the LEP accelerator. The detector was conceived to be as hermetic as possible covering the maximum allowed solid angle and to collect as much information as possible from each event. This chapter describes the ALEPH detector with special emphasis in those parts used in the analysis.

3.1 LEP

The Large Electron Positron storage ring (LEP) [29], is a nearly circular accelerator sited at the European Centre of Nuclear Research (CERN) in Geneva. It is located inside a nearly horizontal tunnel of 26.7 km of circumference, at a depth between 80 and 137 m spanning the French and Swiss territories (figure 3.1). It consists of eight arcs and eight straight sections. The beams are formed by bunches of electrons and positrons that circulate inside the beam pipe. They are accelerated in opposite directions and cross in eight or sixteen points in case the number of bunches per beam is four or eight, respectively, although they are steered to collide only in the four points where the detectors are installed. The collisions in the other points are avoided by a system of electrostatic separators.

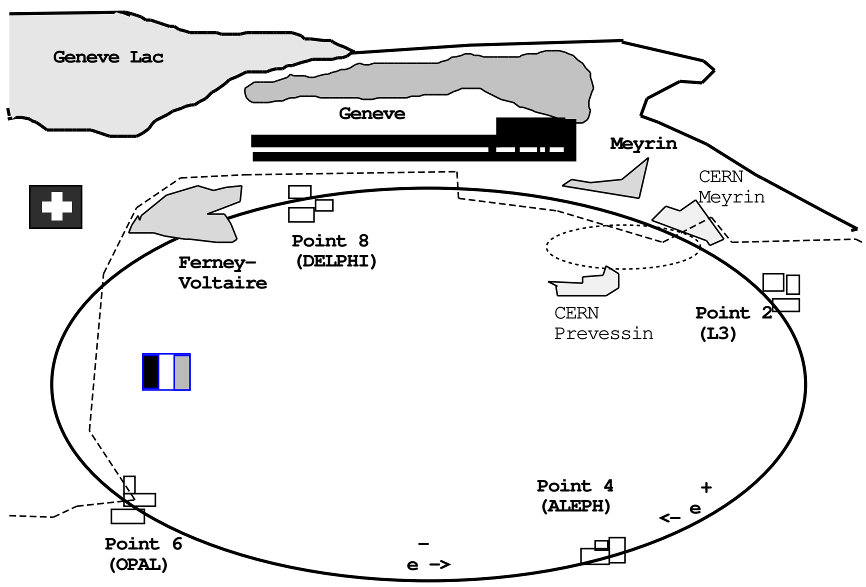

Figure 3.1: The LEP ring.

The accelerator program comprises two phases. In the first (current) phase, LEP accelerates, stores and collides electrons and positrons at a centre-of-mass energy around 90 GeV and produces Z bosons with a luminosity (the number of events per time per unit of cross-section) that has been growing every year and that is now above $10^{31}\,\mathrm{cm}^{-2}\mathrm{s}^{-1}$. In the second phase, to start in 1996, an increase of the centre-of-mass energy up to 180 GeV will allow the production of W pairs at a foreseen luminosity close to $10^{32}\,\mathrm{cm}^{-2}\mathrm{s}^{-1}$.

The LEP injection chain can be seen in figure 3.2. It starts with the LINear ACcelerator (LINAC) which accelerates electrons and positrons in two stages. The electrons are first accelerated up to 200 MeV. Part of the electrons are used to produce positrons and the rest, together with the positrons are accelerated up to 600 MeV. After the LINAC, the particles are inserted into a small circular e^+e^- accelerator (EPA). From there, they are inserted to the PS accelerator, where the energy is taken up to 3.5 GeV. The particles are injected to the SPS accelerator, rising to an energy of 20 GeV. Finally, they are injected to the LEP main ring and accelerated to an energy of $\simeq 45$ GeV with a current up to 6.0 mA per beam.

The running and optics configuration of LEP has changed with time trying

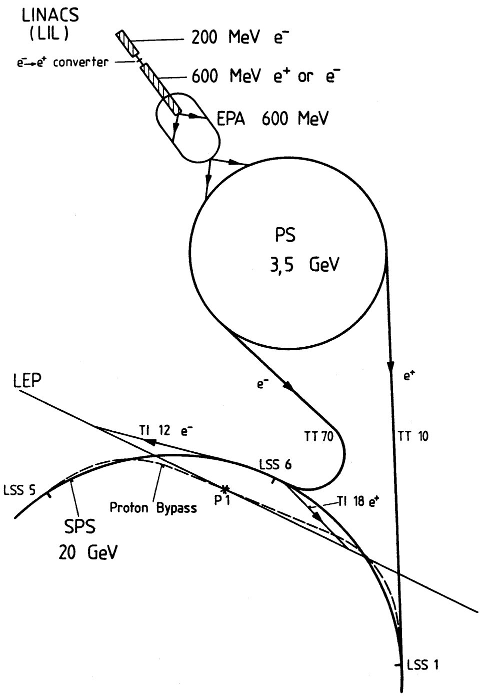

Figure 3.2: Scheme of the LEP injectors and accelerators.

to reach higher luminosities. While in the first years of operation (from 1989 to Oct. 1992), four bunches of electrons were circulating inside the accelerator and were colliding in the interaction points every $22\,\mu$sec, in the 1993 and 1994 running periods collisions of 8 bunches spaced $11\,\mu$sec gave a considerable increase in luminosity. For the 1995 running period, a scheme of four bunch trains of electrons and positrons consisting of two, three or four equally spaced wagons is expected to produce 50K Z per day in each collision point. Table 3.1 gives the main parameters of LEP.

3.2 The ALEPH detector: general description

The ALEPH detector is located at experimental point number 4 in a cavern 143 m under the surface. It is a 12 m diameter by 12 m length cylinder positioned around the beam pipe (tube of 10 cm of radius that forms part of the accelerator). In the ALEPH reference system, the z direction is along the beam line, positive in the

Parameter	Value
Circumference	26667.00m
Average radius	4242.893 m
Bending radius in the dipoles	3096.175 m
Depth	80-137 m
Number of interaction points	4
Number of bunches per beam	4-8
RMS bunch length	11.67 mm
Horizontal bunch sigma	200 μm
Vertical bunch sigma	12 μm
Injection energy	20 GeV
Maximum beam energy (phase I)	55 GeV
RF frequency	353 MHz
Maximum total current per beam	0.006 A
Luminosity	$10^{31}\mathrm{cm}^{-2}\mathrm{s}^{-1}$
Vertical β^*_V	5 cm
Horizontal β^*_H	$25\times\beta^*_V$ cm

Table 3.1: Main LEP parameters.

direction followed by the e^-, thereby slightly different from the local horizontal direction due to the fact that the accelerator is slightly tilted. The positive x direction points to the centre of LEP, and is horizontal by definition. The positive y direction is orthogonal to z and x and deviates 3.5875 mrad from the local vertical direction.

The detector consist of subdetectors, each of one specialized in a different task. The tracking devices allow to reconstruct the trajectories of charged particles and to classify them using the ionization left in the detectors. The electromagnetic and hadronic calorimeters give a measurement of the energy of the particles, being also the only detectors capable to give position information for the neutral particles. Muons are identified using the muon chambers and/or the final planes of the hadronic calorimeter. Specialized detectors situated at low angle give a precise measurement of the luminosity. Some other subdetectors monitor the luminosity and the background. Finally, the trigger and data acquisition system is used to manage everything and record the useful information. A brief description of these devices follows.

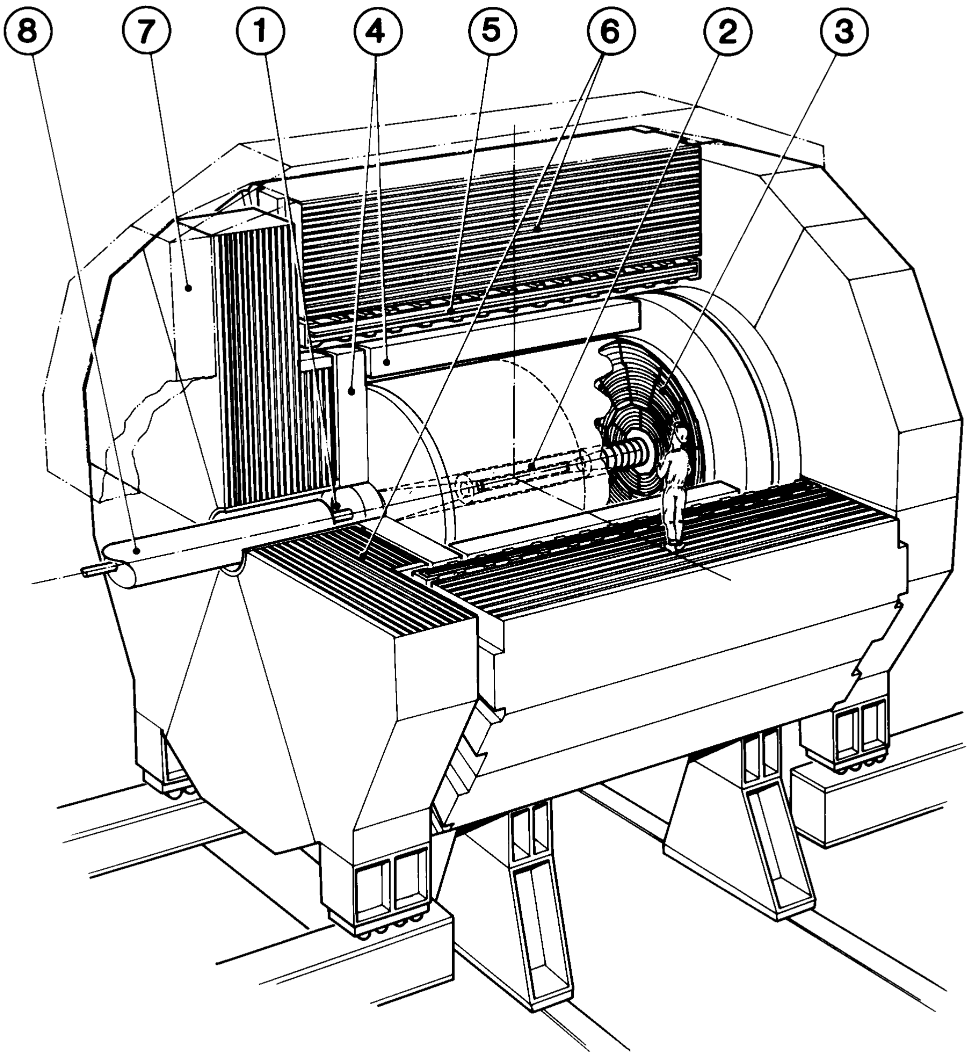

Figure 3.3: Schematic view of the ALEPH detector. (1) Luminosity Monitor. (2) Inner Tracking Chamber. (3) Time Projection Chamber. (4) Electromagnetic Calorimeter. (5) Superconducting Coil. (6) Hadronic Calorimeter. (7) Muon Chambers. (8) Beam Pipe.

Main detectors

A particle leaving the interaction point would encounter the following subdetectors (figure 3.3):

- The Mini Vertex DETector (VDET), fully operational since end 1991, is a double sided silicon strip device with two layers of strips parallel (z) and perpendicular ($r\phi$) to the beam, situated around the beam pipe, providing a very accurate vertex tagging of tracks coming from the interaction point. The coordinate spatial resolution is $10\,\mu$m in $r\phi$ and $13\,\mu$m in z.

- The Inner Tracking Chamber (ITC) is a cylindrical multiwire drift chamber. It contributes to the global ALEPH tracking and is also used for the triggering of charged particles coming from the interaction region. It can provide up to eight precise $r\phi$ coordinates per track, with an accuracy of $100\,\mu$m per coordinate.

- The Time Projection Chamber (TPC), the central track detector of ALEPH, is a very large three-dimensional imaging drift chamber. It provides up to 27 three dimensional coordinate points of each track. The single-coordinate resolution is $173\,\mu$m in the azimuthal direction and $740\,\mu$m in the longitudinal direction. From the curvature of the tracks in the magnetic field, the TPC gives a measurement of transverse particle momenta, p_T, with an accuracy of $\Delta p_T/p_T^2 = 0.6 \cdot 10^{-3}\,(\mathrm{GeV/c})^{-1}$ at 45 GeV, if it is used together with the ITC and the VDET. The chamber also contributes to particle identification through measurements of energy loss (dE/dx) derived from about 340 samples of the ionization for a track traversing the full radial range.

- The Electromagnetic CALorimeter (ECAL) is a sampling calorimeter consisting of alternating lead sheets and proportional wire chambers read out in projective towers. A granularity about $1^\circ \times 1^\circ$ is obtained. The ECAL measures the energy and position of electromagnetic showers. The high position and energy resolutions achieved lead to good electron identification and allow to measure photon energy even in the vicinity of hadrons.

- The superconducting coil is a liquid-Helium cooled superconducting solenoid creating, together with the iron yoke, a 1.5 T axial magnetic field in the central detector.

- The Hadronic CALorimeter (HCAL) is a sampling calorimeter made of layers of iron and streamer tubes. It measures energy and position for hadronic showers and, complemented with the muon chambers, acts as a muon detector. The readout is performed twice: using cathode pads forming projective towers and using digital readout of the streamer tubes for muon tracking and also for triggering. It also provides the main support of ALEPH, the large iron structure serving both as hadron absorber and as return yoke of the magnet.

- The MUON chambers (MUON), outside HCAL, are two double layers of limited streamer tubes which measure position coordinates of the muons, only detectable particles reaching this subdetector.

Luminosity and beam monitoring

An accurate luminosity measurement is required for the precise measurement of cross-sections. This is provided by four detectors for small angle Bhabha scattering installed around the beam pipe:

- The Luminosity CALorimeter (LCAL), is a lead/wire calorimeter similar to ECAL in its operation. It consists of two pairs of semi-circular modules placed around the beam pipe at each end of the detector.
- The SIlicon luminosity CALorimeter (SICAL) was installed in September 1992 on each side of the interaction region. It uses 12 silicon/tungsten layers to sample the showers produced by small angle Bhabhas. It improves the statistical precision of the luminosity measurement by sampling at smaller angles than LCAL. The systematic error of the luminosity is also reduced thanks mainly to the greater precision in the positioning of its components.
- The very small Bhabha CALorimeter (BCAL) located behind the final focus quadrupoles, is used to give a measurement of the instantaneous luminosity and also as a background monitor. It is a sampling calorimeter made of tungsten converter sheets sandwiched with sampling layers of plastic scintillator. A single plane of vertical silicon strips is used to locate the shower position.

The optimization of LEP performance needs also some monitoring of the beam conditions which is accomplished by:

- The Small Angle Monitor of BAckground (SAMBA) is positioned in front of the LCAL at either end of the detector. It consists of two multi-wire proportional chambers at each end, read out in two rings of 8 pads per ring. It is used as a background monitor.

– The Beam Orbit Monitors (BOMs), located around the circumference of LEP, measure the mean position and angle of the beam orbits which are used by LEP to optimize the beam conditions, and by ALEPH to determine the (x, y) position of the beam spot as a starting point for offline reconstruction of the primary vertex.

Trigger system

Not all the collisions that take place at LEP are useful for the physics that ALEPH is willing to study. The large amount of non-useful events have to be filtered out in order to avoid inefficiencies in the detector and a large amount of unused data. For example, if an event is decided to be recorded, it takes up to $45\,\mu$sec for the ionization electrons to reach the end-plates of the TPC and the electromagnetic calorimeter takes up to $61\,\mu$sec to be cleared and ready for the next event. Since three bunch crossings occur in this time, this operation must be performed only when the event will be useful, otherwise large inefficiencies would be introduced. The purpose of the trigger system is to produce a signal that starts the readout of the events. It is desirable to keep all the electron-positron collisions and to reduce as much as possible the rate of background events. The trigger system has been organized in a three-level scheme:

– **Level one** decides whether or not to read out all the detector elements. Its purpose is to operate the TPC at a suitable rate. The decision is taken approximately $5\,\mu$s after the beam crossing from pad and wire information from ECAL and HCAL and hit patterns from the ITC. The level one rate must not exceed a few hundred Hz. If the decision is not to take the event, the TPC is reset and kept ready for the next event.

– **Level two** refines the level one charged track triggers using the TPC tracking information. If the level one decision cannot be confirmed, the readout process is stopped and cleared. The decision is taken approximately $50\,\mu$s after the beam crossing (the time at which the TPC tracking information is available). The maximum trigger rate allowed for level two is about 10 Hz.

– **Level three** is performed by software. It has access to the information from all detector components and is used to reject background, mainly from beam-gas interactions and off-momentum beam particles. It ensures a reduction of the trigger rate to 3–4 Hz, which is acceptable for data storage.

This trigger scheme has to be rather flexible since it has to be able to reject the background and keep signals from possible new physics events. Therefore the available electronic signals from different ALEPH detector components allow for a variety of triggers which, together, cover all possible types of events.

Data Acquisition System and Event Reconstruction

The data acquisition system allows each subdetector to take data independently, process all the information taken by the detector, activates the trigger system at every beam crossing, writes the data in a storage system and monitorizes and regulates continuously all the detector and electronic system.

The DAQ [30] architecture is highly hierarchical. Following the data and/or control flow from the bunch crossing of the accelerator down to storage device, the components found and their tasks are briefly described below:

– Timing, Trigger and Main Trigger Supervisor: synchronize the readout electronics to the accelerator and inform the ReadOut Controllers (ROCs) about the availability of the data.

– ROCs: initialize the front-end modules, read them out and format the data.

– Event Builders (EBs): build a subevent at the level of each subdetector and provide a 'spy event' to a subdetector computer.

– Main Event Builder (MEB): collects the pieces of an event from the various EBs and ensures resynchronization and completeness.

– Level three trigger: as seen, performs a refined data reduction.

– Main host and subdetector computers: The main machine (an AXP Cluster) initializes the complete system, collects all data for storage and provides the common services. The subdetector computers get the 'spy events' and perform the monitoring of the large subdetectors (TPC, ECAL, HCAL).

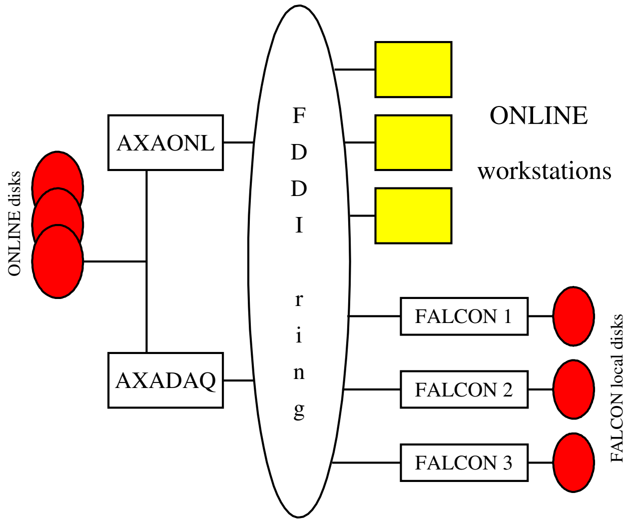

Figure 3.4: Schematic representation of the ONLINE and FALCON cluster.

The data taken by the online computers is called raw data and is reconstructed quasi online. In less than two hours after the data is taken, the event reconstruction and a check of the quality of the data is done, thus allowing ALEPH to have a fast cross-check of the data and correct possible detector problems. This task is performed by the Facility for ALeph COmputing and Networking (FALCON) [31].

The year by year continuous increase of CPU power of the machines has made the hardware and software of FALCON develop in order to accommodate to the available performance and requirements.

In its current configuration, FALCON consists of three processors (three DEC-AXP machines with a total power of $\simeq$ 60 CERN units [1]), connected as sketched in figure 3.4. Each of the processors runs the full ALEPH reconstruction program JULIA (Job to Understand Lep Interactions in ALEPH) [32] which, for each event of the raw data file, processes all the information from the different subdectectors. Other programs also run to compute the drift velocity in the TPC (PASS0), or to analyze the quality of the data taken (RunQuality).

After their reconstruction, the events are written in POT (Production Output Tape) data files and transmitted to the CERN computer center where they are

[1] A CERN unit is equivalent to an IBM 168 CPU unit, approximately 1/6 of an IBM 3090 processor or about 1.2 Mflops.

converted into different data types more suitable for physics analysis. The events are ready to be analyzed only a few hours after the raw data have been taken.

3.3 Subdetectors relevant to the analysis

The measurement of the scaled energy distributions and the selection of hadronic events need only the use of tracking devices, especially the TPC and the ITC that determine the polar angle and the momentum of the particles. However, the selection of flavour-tagged samples of events needs the VDET detector and also the use of the calorimeters.

The tracking detectors are described in detail in the following sections. Also a description of the electromagnetic and hadronic calorimeters is given, although less detailed due to their more limited importance for the analysis.

3.3.1 The Mini Vertex Detector

The VDET is formed by 96 silicon wafers each of dimension $(5.12 \times 5.12 \times 0.03)$ cm arranged in two coaxial cylinders around the beam pipe. The inner layer has nine wafers in azimuth, with average radius of 6.5 cm, and the outer has 15 wafers with average radius of 11.3 cm, both layers being four wafers long. Each wafer has $100\,\mu$m strip readout both parallel ($r\phi$) and perpendicular (rz) to the beam direction. Particles passing through a wafer deposit ionization energy, which is collected on each side of the wafer.

The advantage of the VDET is that it pinpoints a track's location in space quite near to the beam pipe. VDET hits are used by extrapolating a track found by the ITC and/or the TPC to the VDET and then refitting the track more precisely using VDET hits which are consistent with it. The addition of VDET to the tracking improved the momentum resolution at 45 GeV to $\Delta p_T/p_T^2 = 0.6 \cdot 10^{-3}\,(\mathrm{GeV/c})^{-1}$ from $\Delta p_T/p_T^2 = 0.8 \cdot 10^{-3}\,(\mathrm{GeV/c})^{-1}$ when only TPC and ITC were used [34].

Using VDET, together with the other tracking detectors, the spatial coordinates of the origin of a 45 GeV charged track's helix (impact parameter) can be found to within about $23\,\mu$m in the $r\phi$ view and $28\,\mu$m in the rz view measured from dimuon events. For lower momentum tracks, this parameter is measured from hadronic Z

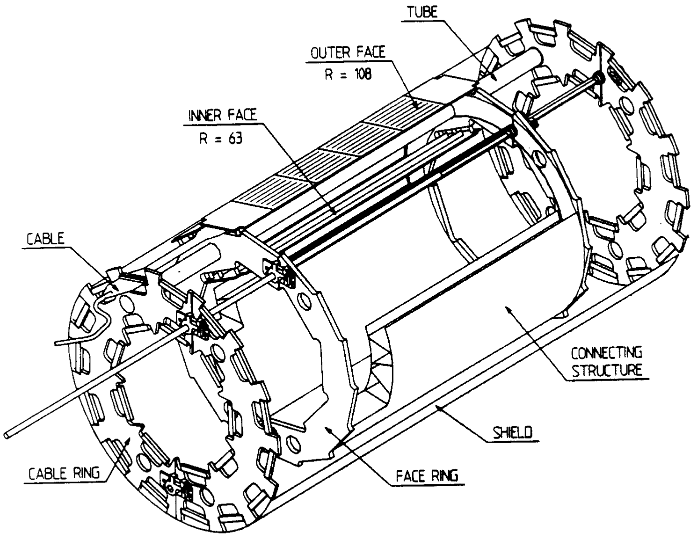

Figure 3.5: Cut-away view of the VDET.

decays. The resolution on the impact parameter can be parametrized as [35]

$$\sigma(\delta) = 25\,\mu\mathrm{m} + \frac{95\,\mu\mathrm{m}}{p}(\mathrm{GeV/c})^{-1}. \tag{3.1}$$

This allows tracks produced by decays of short-lived particles to be separated from those at the primary interaction point with good efficiency.

3.3.2 The Inner Tracking Chamber

The Inner Tracking Chamber (ITC) [36] using axial wires made of gold and tungsten provides up to eight $r\phi$ points for tracking in the radial region between 16 and 26 cm. It also provides the only tracking information for the level one trigger system. It is able to identify roughly the number and geometry of tracks, due to its fast response time (the trigger is available within 2–3 μs of a beam crossing) and allows non-interesting events to be quickly rejected.

The ITC is operated with a gas mixture of argon (50%) and ethane (50%) at atmospheric pressure.

The ITC is composed of 8 layers of sensing wires (operated at a positive potential in the range $1.8 - 2.5\,\mathrm{kV}$) running parallel to the beam direction, located

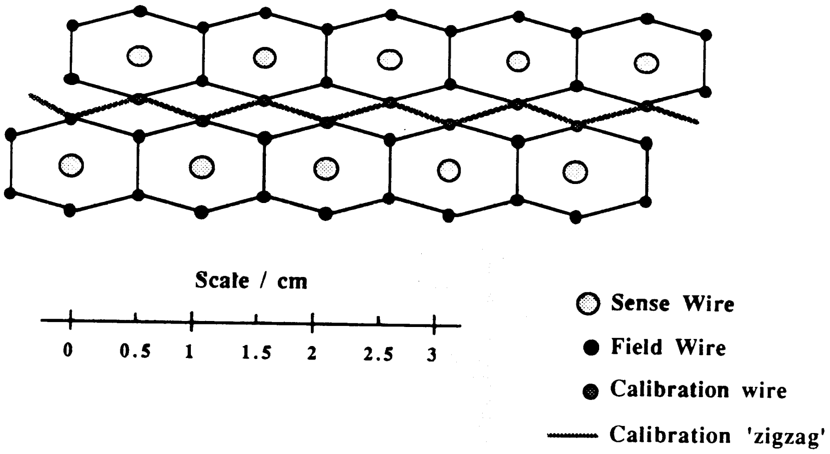

Figure 3.6: The ITC drift cells.

forming hexagonal cells with the central sense wire surrounded by six field wires held at ground potential (figure 3.6). The sense wires detect the ionization of particles passing close by. The measurement of the drift time gives the measurement of the $r\phi$ coordinate within about $150\,\mu$m. The z coordinate is found by measuring the difference in arrival times of pulses at the two ends of each sense wire, but with an accuracy of only about 3 cm. The particles with polar angles between 14 and 166 degrees pass through the 8 layers.

3.3.3 The Time Projection Chamber

The Time Projection Chamber (TPC) [37] was designed to obtain high precision measurements of the track coordinates, to get good momentum resolution and to measure the dE/dx depositions of charged particles.

The time projection chambers use the techniques of the ionization chambers to measure the transverse (x-y) coordinates, while measuring the time to detect each ionized bunch of electrons gives the position in the z coordinate. In the case of ALEPH, the charged particles create ionization in the gas that fills the TPC. The electrons produced in this ionization are driven by an electric field to the end-plates where wire chambers are located. There, a secondary ionization takes places and the position where this happens gives the $r\phi$ coordinate. The time needed for the electrons to reach the end-plate gives the z coordinate. Due to the 1.5 T magnetic field produced by a superconducting solenoid surrounding the TPC whose axis is parallel to the TPC symmetry axis, the trajectory of a charged particle inside the TPC is a helix, and its projection onto the end-plate is an arc of a circle. By measuring the sagitta of this arc, one obtains the curvature radius that is proportional to the modulus of the component of the momentum perpendicular to the magnetic field.

The TPC is a cylindrical structure of 4.4 m long with 35 cm and 180 cm of inner and outer radius, respectively (figure 3.7). Its volume is delimited by two coaxial cylinders which hold the end-plates. The dimensions were designed to reach 10% resolution in transverse momentum for the highest possible momenta (muon pairs produced at the LEP energy of 90 GeV per beam). The resolution Δp_T in transverse momentum p_T (GeV/c) is proportional to the resolution in the measurement of the

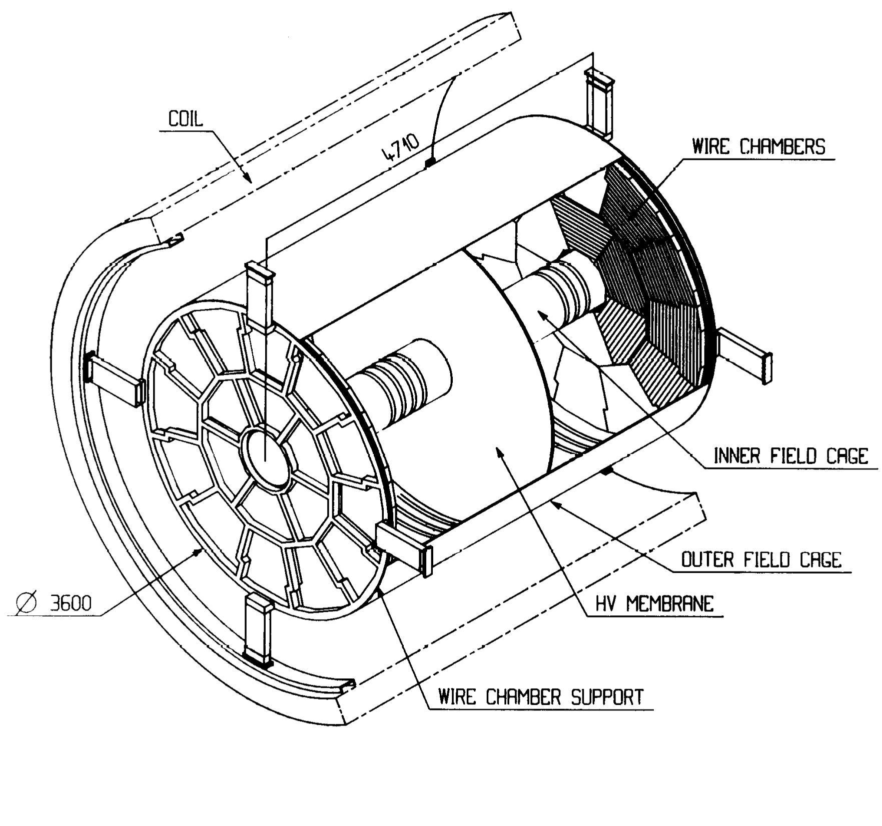

Figure 3.7: Scheme of the TPC.

sagitta Δs (mm):

$$\frac{\Delta p_T}{p_T} = 0.027 p_T \frac{\Delta s}{l^2 B} \tag{3.2}$$

where B(T) is the modulus of the magnetic field and l(m) is the length of the projected trajectory. This was optimized by choosing the largest practical lever arm $l = R_{max} - R_{min} \simeq 1.4\,\mathrm{m}$.

The device is divided into two half-detectors by a membrane which is situated in the plane perpendicular to the axis and midway between the end planes. This central membrane is held at a negative high voltage ($-26\,\mathrm{kV}$) and the end-plates are at a potential near ground. The curved cylindrical surfaces are covered with electrodes held at potentials such that the electric field in the chamber volume is uniform and parallel to the cylinder axis.

The TPC volume is filled with a nonflammable gas. Traversing particles will ionize it producing electrons that will be drifted towards one end-plate by the electric field of 110 V/cm. The argon(91%) + methane(9%) gas mixture was chosen because with this mixture is possible to reach high $\omega\tau$ values (ω = cyclotron frequency; τ = mean collision time of the drifting electrons). This causes the electrons to drift mainly along the magnetic field lines and thereby reduces the systematic displacements due to the electric field inhomogeneities.

The electrons produced by the ionization are amplified in the proportional wire chambers positioned in the end-plates. There are 18 wire chambers ('sectors') on each end-plate. In each end-plate, there are six sectors of type K (Kind), surrounded by a ring of alternating sectors of type M(Mann) and W(Weib). In order to get a minimum loss of tracks at boundaries, the sectors are arranged in the 'zig-zag' geometry that can be seen in figure 3.8 in order to get a minimum loss of tracks at boundaries. The gaps between the sectors must be as small as possible. High precision in the alignment of each chamber with the others is also required because each radial track is measured by two different wire chambers.

The wire chambers consist on three layers of wires (figure 3.9):

- The gating grid [38] prevents positive ions produced in the avalanches near the sense wires from entering the main volume of the TPC, distorting the electric field. Potentials of $V_g \pm \Delta V_g$ ($V_g \simeq -67\,\mathrm{V}$) are placed on alternative wires of the grid. A ΔV_g of 150 V was chosen to block both the passage of positive

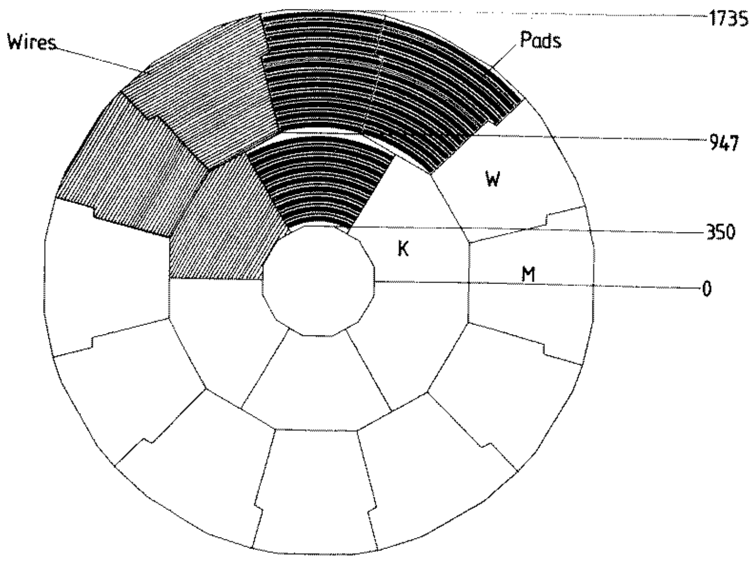

Figure 3.8: View of a TPC end-plate.

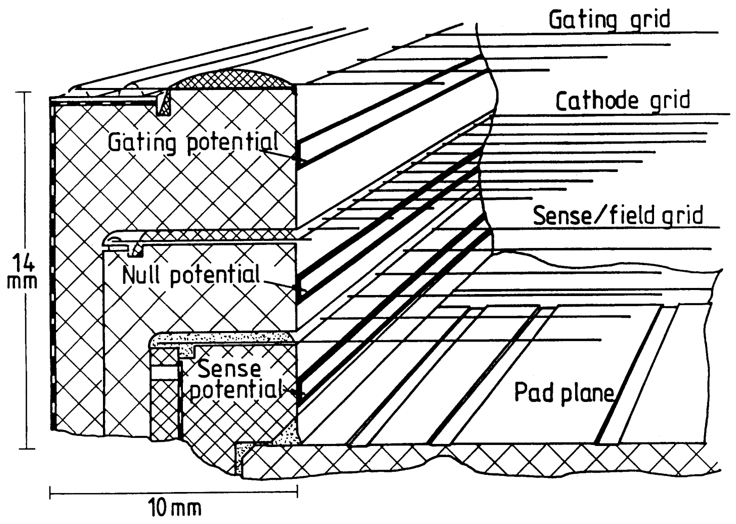

Figure 3.9: View of a TPC wire chamber.

ions to the drifting volume of the chambers and the incoming electrons in the wire region. The gate is opened $3\,\mu$s before every beam crossing. If a positive trigger signal arrives, the gate is kept open, otherwise the gate is closed after $\sim 5\,\mu$s.

- The cathode wires keep the end-plates at null potential and together with the central membrane create the electric drift field.

- The sense wires are read out to give the energy deposition (dE/dx) [39] for particle identification and the z measurement of the tracks. For the estimation of the dE/dx, a truncated mean algorithm is used, taking the mean of the 60% smaller pulses associated with a track. The achieved resolution is 4.6% for electrons in hadronic events (slightly better for low multiplicity events). The field wires are kept at null potential to create equipotential surfaces around the sense wires.

The ionization avalanches created around the sense wires are read out by the signal induced on cathode pads at a distance of 4 mm from the sense wires. The pads are connected to preamplifiers via wires passing through the structure which supports the wire grids.

3.3.4 The Electromagnetic and Hadronic Calorimeters

The electromagnetic [40] and hadronic calorimeters consist both of a barrel and two end-caps located around the TPC. While the electromagnetic calorimeter is placed inside the coil, the hadronic calorimeter is placed outside, which makes it be also the return of the magnetic flux of the magnet (figure 3.10).

Both are sampling calorimeters where the main active material is gas. Their barrels are divided into modules of $30°$ and $15°$ in azimuthal angle, ϕ, for the ECAL and HCAL, respectively. The end-caps of the ECAL and HCAL are also divided in modules of $30°$ and $60°$ in ϕ, respectively.

The barrel modules of the two calorimeters have a small rotation angle between them to avoid cracks in all the calorimeter system. The modules of the end-caps are also rotated with respect to the ones in the barrels.

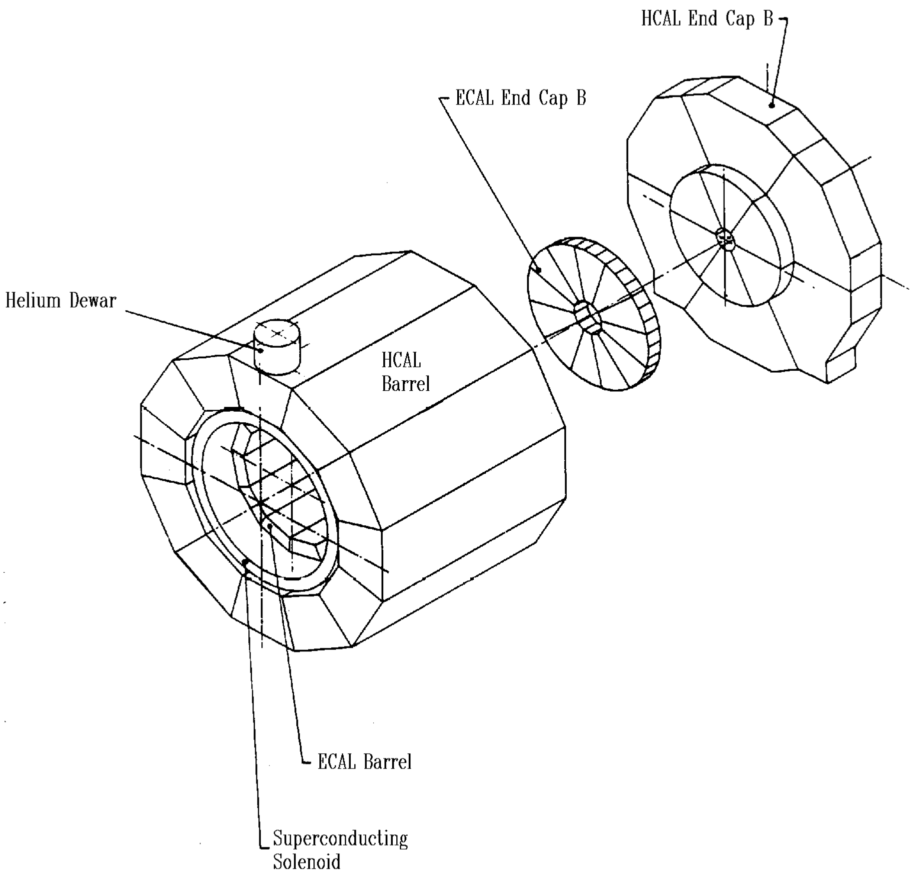

Figure 3.10: Overall view of the Electromagnetic and Hadronic calorimeters.

The barrels are 4.8 m and 6.3 m long for the ECAL and HCAL respectively. The ECAL extends from an inner radius of 1.85 m to an outer radius of 2.25 m and the HCAL from 3 m to 4.68 m.

The modules of the electromagnetic calorimeter, with a total thickness of 22 radiation lengths, consist on 45 layers of lead and wire chambers full with 80% xenon and 20% CO_2 gas. The structure of a single layer consists (figure 3.11) on a lead sheet, a wire chamber plane (anode plane) made of open-sided aluminium extrusions and a pad plane (cathode plane) covered by a graphited mylar sheet.

The cathode pads are connected internally forming towers which point to the

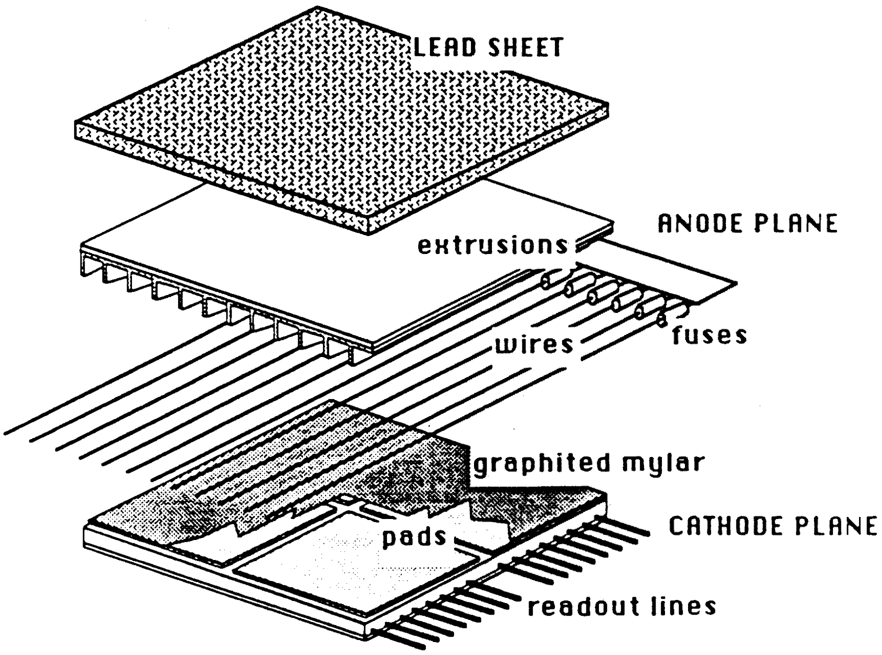

Figure 3.11: View of an ECAL stack layer.

interaction point. Each tower is read out in three sections in depth ('storeys'). The size of the pads is approximately $30 \times 30\,\mathrm{mm}^2$ leading to a high granularity (73728 towers). In addition to the signal of the pads, an analog signal is also available from each anode wire plane. These signals are used for testing and calibrating the modules and also for triggering.

The achieved energy resolution for electrons and photons is [35]

$$\frac{\sigma_E}{E} = \frac{0.178}{\sqrt{E/\mathrm{GeV}}} \oplus 0.019, \tag{3.3}$$

and the angular resolution for charged tracks with $|\cos\theta_{\mathrm{track}}| < 0.98$ is [35]

$$\sigma_{\theta,\phi} = \left(\frac{2.5}{\sqrt{E/\mathrm{GeV}}} + 0.25 \right) \mathrm{mrad}. \tag{3.4}$$

The hadronic modules have 22 iron sheets, each one with a width of 5 cm and an external plane of 10 cm, with a total amount of iron of 1.20 m (7.16 interaction lengths), which is enough to contain the hadronic showers at LEP energies. Between the iron sheets, there are modules of streamer tubes filled with a mixture of argon (21%), CO_2 (42%) and isobutane (37%).

Three different kinds of signals are read out in the hadronic calorimeter: signals from the pads situated outside the modules containing the streamer tubes, which are used to measure the energy of the showers; signals from the strips situated along the streamer tubes modules, which give the pattern of the streamer tubes in the event and are used as a 'tracking' of the showers; and the signal from the wires, which measures the energy released in the planes and is used mainly for triggering.

The energy resolution is given by [35]

$$\frac{\sigma_E}{E} = \frac{0.85}{\sqrt{E/\mathrm{GeV}}}. \tag{3.5}$$

Chapter 4

Event reconstruction and simulation

This chapter gives a description of the reconstruction processes and tagging algorithms needed in the measurement of the scaled energy distributions for charged tracks that will be described in chapter 5. The track reconstruction is described in section 4.1. A brief explanation of the energy and position reconstruction with the calorimeters is presented in section 4.2. The calorimeter and track information is used in the energy flow algorithm described in section 4.3, which is used by one of the event shape flavour tagging algorithms. This algorithm and the impact parameter tag algorithm are described in section 4.4. Finally, section 4.5 explains the Monte Carlo simulation chain in ALEPH and gives a brief description of the hadronic Monte Carlos used in the analysis.

4.1 Tracking in ALEPH

Before any measurement of the momentum and track parameters is performed, the raw data coming from the tracking detectors have to be processed and track coordinates have to be measured in order to join them together to finally form a track helix. The next sections describe the coordinate finding of the three subdetectors and the track reconstruction from them.

4.1.1 Coordinate finding

TPC The TPC measures the ionization induced by a charged particle traversing the gas volume of the chamber. The cloud of charge is projected onto the TPC end-plates (by the electric field) and is measured by the sense wires and the pads. The information coming from both is grouped in hits, which contain the pad or wire number, the pulse length and the arrival time of each pulse, and digitizations, that contain pulse-height samples, ie. the details of the pulse shapes [41].

The pad-hit data are grouped into two-dimensional clusters; starting with one pulse, another pulse on an adjacent pad is included if it overlaps the first by at least one sample. In order to separate, or at least recognize, within each cluster the contributions coming from different particles, all clusters are analyzed again, this time with the digitization information considered. Peaks that are sufficiently isolated from others form subpulses. For each subpulse, both a charge estimate and a time estimate are made from digitizations. These estimates are used by the coordinate algorithms. For each good subcluster a three dimensional coordinate is calculated and errors are determined from the widths, in space and time, of the subcluster. The $r\phi$ coordinates are calculated by using a Gaussian model of the pad response if only a few pads are involved, or simply by taking a charge-weighted average of the positions if many pads are involved. The z-coordinate is always determined from a charged weighted average of time estimates of the individual subpulses. All coordinates are corrected for misalignment and distortions of the drift field.

The cluster sizes in the end-plates are $\sim 1.5\,\mathrm{cm}$ in $r\phi$ and $\sim 2\,\mathrm{cm}$ in z. Thus, there are cases in which the clusters belong to more than one track. However, the probability that two tracks overlap all their clusters is small.

The $r\phi$ spatial resolution depends on the diffusion (which, in turn, depends on the drift distance), the alignment of the electric and magnetic fields, the localization of the avalanche in the sense wire, the angle to the track with respect to the pad and on electronic noise and errors in the calibration. An overall resolution $\sigma_{r\phi} = 173\,\mu\mathrm{m}$ is measured. The resolution in the z coordinate is $\sigma_z = 740\,\mu\mathrm{m}$.

ITC The ITC also produces three dimensional coordinates from the raw data consisting on the wire (channel) number, and the time values in $r\phi$ and z.

The z coordinate is reconstructed from the difference in the arrival times of the signals to the two ends of the wire.

To obtain the nominal $r\phi$ coordinate the wire number is used. The $r\phi$ TDC value is used to calculate the drift-time. The relationship between the drift-time and the distance is not linear. The drift-time value is used to generate two coordinates one on each side, azimuthally, of the anode wire. The proper location of the coordinate can only be obtained at the tracking stage when the angle of the track through the drift cell is known.

The $r\phi$ resolution depends on the drift time, the error being worse close to both anode and field wires than in between. The resolution is parametrized as a parabola in azimuthal drift-distance with the minimum of approximately $100\,\mu$m occurring mid-way between the anode and field wires.

VDET The raw data of the Vertex Detector contain the list of channels (and its pulse-height) in the event with a signal above a defined threshold and the seven channels at each side of it. Hits are reconstructed by averaging the charge-weighted position of adjacent strips that have at least three times the mean noise charge. The correlation between the charge measured in the two views is used to identify double-track clusters. Monte Carlo studies show that the vertex detector hit association is correct for 98% (90%) of the hadronic Z decay tracks with hits in both (one) layers.

4.1.2 Track reconstruction

Once all the coordinates have been found, the tracking [42, 43], is done starting in the TPC by first merging coordinates consistent with an arc of helix less than π radians to form a chain. The chains that are determined to belong to the same helix are linked together into a single track candidate.

Finally, the five helix parameters, as defined in figure 4.1, are determined by a fit of a helix to the pad coordinates within the first half turn of each track candidate. To account for multiple scattering within the fit, the coordinate error estimates are increased in accordance with the material traversed by the track from its origin. The fit is allowed to remove outlying coordinates and to break a track between two

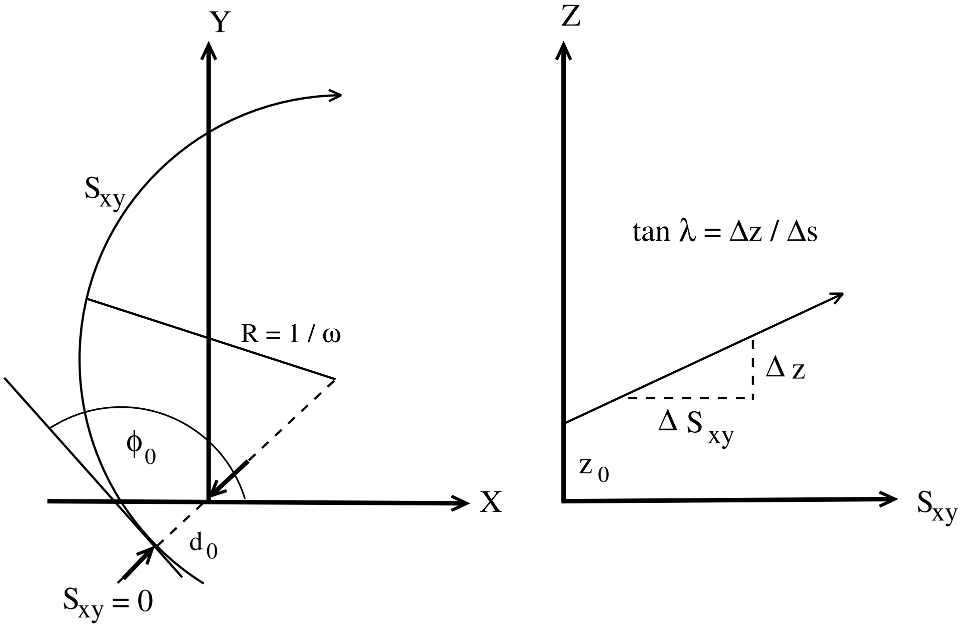

Figure 4.1: Helix parameters used in the TPC tracking programs: ω, inverse radius of curvature; d_0, distance of closest approach to the z axis; z_0, z coordinate where d_0 is measured; ϕ_0, ϕ at closest approach to the z axis, and $\tan\lambda$, tangent of the dip angle.

coordinates if there is evidence from the fit of a particle decay. What results, in the end, is a set of TPC-fitted tracks.

These track candidates are extrapolated to the inner detectors (ITC and VDET) where consistent hits are assigned. First, the TPC track trajectories are projected back into the ITC and a search is made for ITC coordinates around each trajectory. If more than three hits are found, a fit is performed and the ITC track is accepted if the fit satisfies a χ^2 cut. Afterwards, the same procedure is performed with VDET hits to associate them to the extrapolated ITC-TPC tracks using a χ^2 discriminator to decide which hit has to be associated to a given track.

Coordinate errors are determined using the preliminary track parameters. The final track fit, based on Kalman filter [44] techniques, uses these errors and takes into account multiple scattering between each measurement.

The track finding efficiency in the TPC has been studied using Monte Carlo simulation. In hadronic Z events, 98.6% of tracks that cross at least four pad rows in the TPC are reconstructed successfully. The small inefficiency is due to track overlaps and cracks. The Monte Carlo simulation has been found to reproduce the track efficiency to better than 10^{-3} by studying dilepton events from the data themselves. The efficiency of associating a vertex detector hit to an isolated track is about 94 % per layer, within the geometrical acceptance.

Systematic effects in the tracking parameters come from electric and magnetic field inhomogeneities, uncertainties in the small angle between the axes of the electric and magnetic fields, and from the systematic errors in the drift velocity. The distortions induced by these effects can be corrected and affect mainly the track parameters related with the position of the tracks.

A transverse momentum resolution of

$$\sigma(1/p_T) = 0.6 \times 10^{-3}\ (\mathrm{GeV}/c)^{-1} \tag{4.1}$$

is measured (for 45 GeV muons). At low momentum, multiple scattering dominates and adds a constant term of 0.005 to $\sigma(p_T)/p_T$.

4.2 Energy and position reconstruction with the calorimeters

To reconstruct the calorimetric energy, the hit storeys are combined to find topologic clusters (a cluster being a group of spatially connected storeys, having at least one corner in common). In the ECAL, the triggered storeys are scanned and the first cluster is created if the energy of the storey is larger than a certain amount ($t_{high} = 90\,\mathrm{MeV}$). Then the neighbouring storeys are scanned and they are added if their energy is larger than $t_{low} = 30\,\mathrm{MeV}$. In a similar fashion, in the HCAL, the tower information is also reconstructed in the form of clusters.

To associate clusters with charged tracks, the track is extrapolated step-by-step to the ECAL region. At each step, the ECAL geometry package is used to determine which storeys are intercepted by the track. Then the clustering algorithm is used to determine if the storey, or its neighbours, are hit and to which cluster they belong. A track and a cluster are associated if one point of this track is in one storey of the cluster or in a storey which has at least one corner in common with the cluster.

The position of the showers is calculated by an energy-weighted mean of the position of the individual storeys or towers in the cluster. This is corrected for the usual 'S-shape' distortions present in all the granular detectors that tend to bias the reconstructed position towards the center of the cell that has the maximum signal.

The information from the calorimeters is used in the particle identification algorithms giving good electron and muon identification efficiencies and photon and π^0 reconstructions.

4.3 Energy flow determination

The energy flow algorithm [35] is used in the event-shape algorithm for flavour tagging in hadronic events. A description of the algorithm is given in this section.

The simplest way to determine the energy flow of an event recorded in the ALEPH detector is to make the sum of the raw energy found in all calorimetric cells without performing any particle identification. This method yields a resolution of $\sigma_E/E = 1.2/\sqrt{E/\mathrm{GeV}}$ for hadronic decays of the Z. The energy flow algorithm developed in ALEPH improves this resolution by making use of track momenta and taking advantage of the photon, electron and muon identification capabilities.

A first cleaning procedure is done to eliminate poorly reconstructed tracks, V^0's not compatible to originate from the nominal collision point, and noisy channels and fake energy deposits in the calorimeter towers.

After the cleaning, the charged particle tracks are extrapolated to the calorimeters, and groups of topologically connected tracks and clusters (called 'calorimeter objects') are formed. Each calorimeter object is then processed using the following steps.

1. All the charged particle tracks coming from the nominal interaction point or belonging to a reconstructed V^0, are counted as charged energy assuming they are pions.

2. The charged particle tracks identified as electrons, are removed from the calorimeter object, together with the energy contained in the associated electromagnetic calorimeter towers. If the difference between this calorimeter

energy and the track momentum is larger than three times the expected resolution, this difference is assumed to come from a bremsstrahlung photon, and is counted as neutral electromagnetic energy.

3. The charged particle tracks identified as muons, are removed from the calorimeter object, together with a maximum of 1 GeV from the closest associated electromagnetic calorimeter cluster (if any) and a maximum of 400 MeV per plane fired around the extrapolation of the muon track from the corresponding hadron calorimeter cluster.

4. The photons and π^0's are counted as neutral electromagnetic energy and are removed from the calorimeter object.

5. At this stage, the only particles left in the calorimeter object should be charged and neutral hadrons. The charged hadron energy has already been determined in the first step, but the neutral hadron energy has not been accounted for. Although possible in principle via a specific pattern recognition, a direct identification of neutral hadrons is difficult and has not yet been attempted for the energy-flow reconstruction. Here, a neutral hadron is identified as a significant excess of calorimetric energy: in a given calorimeter object, the remaining energy left in the calorimeters is summed, after first scaling that from the electromagnetic calorimeter by the ratio of the calorimeter's response to electrons and pions. If this sum exceeds the energy of any remaining charged particle tracks, and the excess is both larger than the expected resolution on that energy when measured in the calorimeters, and greater than 500 MeV, then it is counted as neutral hadronic energy. The ratio of the electromagnetic calorimeter's response to electrons and pions has been determined to be ~ 1.3 with test-beam data. However, in order to account for the fact that low energy photons often escape identification in the preceding step of this analysis, the ratio is modulated according to the penetration of the particle and is taken as 1.0, 1.3 and 1.6 in the first, second and third segments in depth of the calorimeter, respectively.

This is repeated for all the calorimeter objects of the event and results in a set of 'energy-flow objects' (electrons, muons, photons, charged or neutral hadrons), also called particles, characterized by their energies and momenta. To this list are added

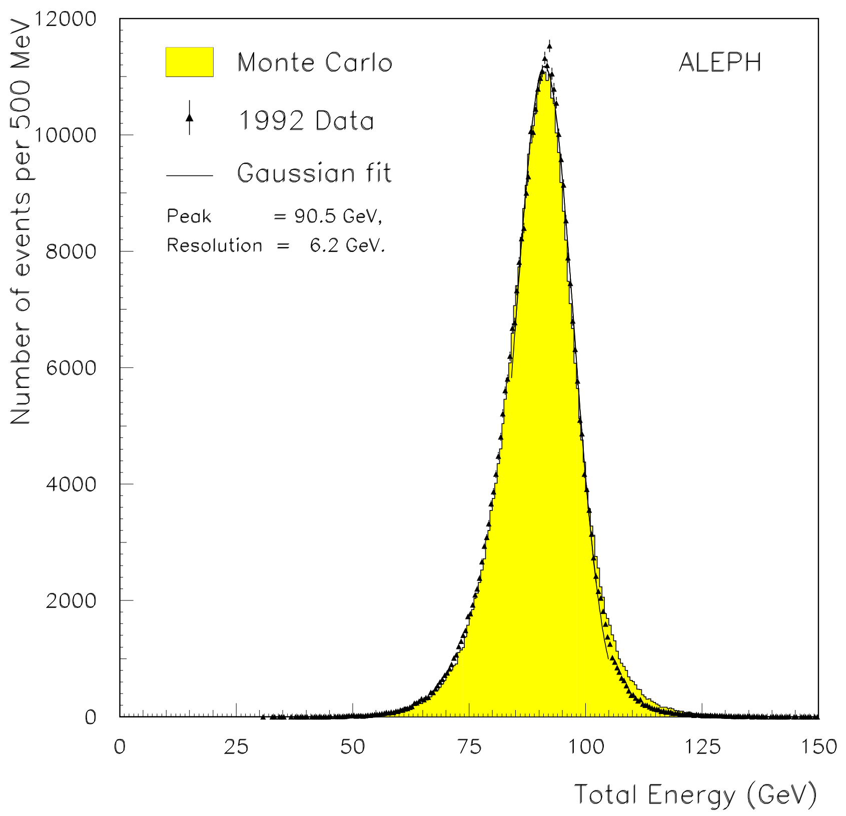

Figure 4.2: Distribution of the total energy for well-contained hadronic events for the 1992 data (points) and Monte Carlo (shaded histogram)

all the clusters found in the luminosity monitors, where no particle identification is available. This list is expected to be a close representation of the reality, i.e. of the stable particles actually produced by the collision. Since the neutrinos escape undetected, they cannot be in the list but they should be detected indirectly by the presence of missing energy in the event.

The energy-flow resolution can be determined from the data using a sample of selected hadronic events. Figure 4.2 shows the distribution of the total energy for well-contained hadronic events A Gaussian fit to the total energy distribution gives a peak value of 90.5 GeV (62 % from charged particles, 25 % from photons and 13 % from neutral hadrons), with a resolution of 6.2 GeV. It is well reproduced by a sample of 700,000 fully simulated hadronic events in which a peak value of

90.7 GeV and a resolution of 6.5 GeV are obtained. The jet angular resolution is 18 mrad for the polar angle and 19 mrad for the azimuthal angle.

4.4 Flavour tagging algorithms

Two flavour tagging algorithms developed in ALEPH have been used in this analysis. The impact parameter tag makes use of the relatively long lifetime of hadrons containing a b quark to distinguish between heavy quark events and light quark ones. The event shape tag makes use of two global properties of the event to make the same classification.

4.4.1 Impact parameter tag

The long lifetime and large mass of b hadrons give their decay products large impact parameters, allowing a separation of these hadrons from hadrons coming from fragmentation or decay of a light quark. This tagging algorithm computes the probability that a track comes from the primary vertex using the measurement of its impact parameter. The probabilities of coming from the primary vertex of all the tracks from a given jet, hemisphere or event can be combined to finally have the probability that the given object (jet, hemisphere or event) comes from a b quark.

The main tool in the analysis is, then, the impact parameter of a track. The measurement of this quantity needs, however, a precise estimation of the e^+e^- interaction vertex for each event which needs also the estimation of the overlap region of the electron and positron beams (beam spot) where it lies on. The description of each of these measurements follows.

Beam spot measurement. The position of the beam spot is determined by studying the distance of closest approach of tracks to the coordinate origin in the $r\phi$ plane, d_0. This quantity is signed according to the sign of the angular momentum component of the track along the beam axis, and in the absence of track distortions, should have a distribution centered on zero. If the beam spot is not centered on the coordinate origin, the mean value of d_0 has a sinusoidal dependence on the

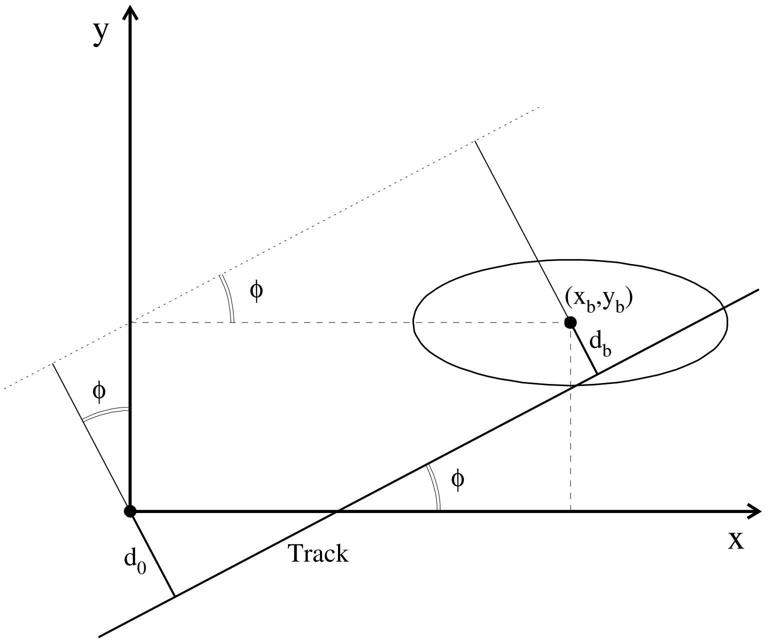

Figure 4.3: Impact parameter with respect to the coordinate origin and with respect to the beam spot centroid. The track is approximated to a straight line in this region.

azimuthal angle ϕ. This dependence can be seen looking at the relation

$$d_b = d_0 - x_b \sin\phi + y_b \cos\phi - d_{\text{off}}, \tag{4.2}$$

which can be deduced from figure 4.3, where, since the distances d_b, d_0, x_b and y_b are small, the track has been approximated to a straight line. d_b is the distance of closest approach of tracks to the beam spot, x_b and y_b are the coordinates of the beam position and d_{off} is an additional offset that takes into account residual tracking effects (alignment errors, field parametrization, etc.).

The mean of d_b for each ϕ is zero. Thus, the fit to the dependence of $< d_0 >$ as function of the angle ϕ gives the coordinates of the luminous region as well as the value of d_{off}.

Since there are variations in the crossing beam coordinates even inside the same fill, this measurement is done every $\sim$ 100 events. For the optics of the LEP machine, the beam spot is expected to be elliptical in shape in the plane perpendicular to the beam direction, with the horizontal width much greater than the vertical one due to synchrotron radiation effects. The predicted dimensions are $\sigma_H = 200\,\mu$m and $\sigma_V = 12\,\mu$m, respectively (table 3.1).

Event crossing point measurement. For each event, the measurement of the three coordinates of the collision point is needed. To perform this, the event is clustered in jets using the E clustering scheme with the energy flow objects. In this scheme, the variable

$$y_{ij} = \frac{(p_i + p_j)^2}{E_{vis}^2} \tag{4.3}$$

is computed for each pair of objects. The four-momenta of the pairs of objects with lower y_{ij} are added and the computation of the y_{ij} is performed again over the new set of objects. This procedure is repeated until all the y_{ij} are higher than a given value, y_{cut}. The remaining objects are the clustered jets. Here, the y_{cut} was chosen to be 0.02.

After the clustering is performed, all tracks satisfying minimal quality cuts are assigned to the nearest jet and then projected onto the plane perpendicular to the axis of its corresponding jet. The primary vertex in the plane perpendicular to each jet is then found. Knowing the direction of each jet, the projected primary vertices are expanded back in three dimensions. A χ^2 fit is performed to combine all the vertices and the beam spot information in the $x-y$ plane in order to get the event crossing point. This procedure ensures that hadron lifetimes do not bias the position of the primary vertex.

Track impact parameter measurement. The impact parameter of a track is defined as the closest approach of the track to the production point of the mother particle of the track. The method to measure this parameter is described in figure 4.4. The point $\vec{V}$ is the primary vertex. $\vec{J}$ is the direction of the mother particle momentum, as approximated by the jet direction. The circular arc represents a track, assumed here to be a decay product. Point $\vec{S_t}$ is the point on the track where it comes closest to the line going through $\vec{V}$ with direction $\vec{J}$. The point $\vec{S_t}$ is used as an approximation to the decay point of the track. The track is linearized at $\vec{S_t}$, and the signed impact parameter is defined as

$$\tilde{D} \equiv D \cdot \text{sign}\left((\vec{S_j} - \vec{V}) \cdot \vec{J}\right), \tag{4.4}$$

being a positive number with value D if the vector $\vec{S_j} - \vec{V}$ lies in the same direction as the jet direction $\vec{J}$, negative otherwise.

The experimental resolution generates a random sign for tracks which originate

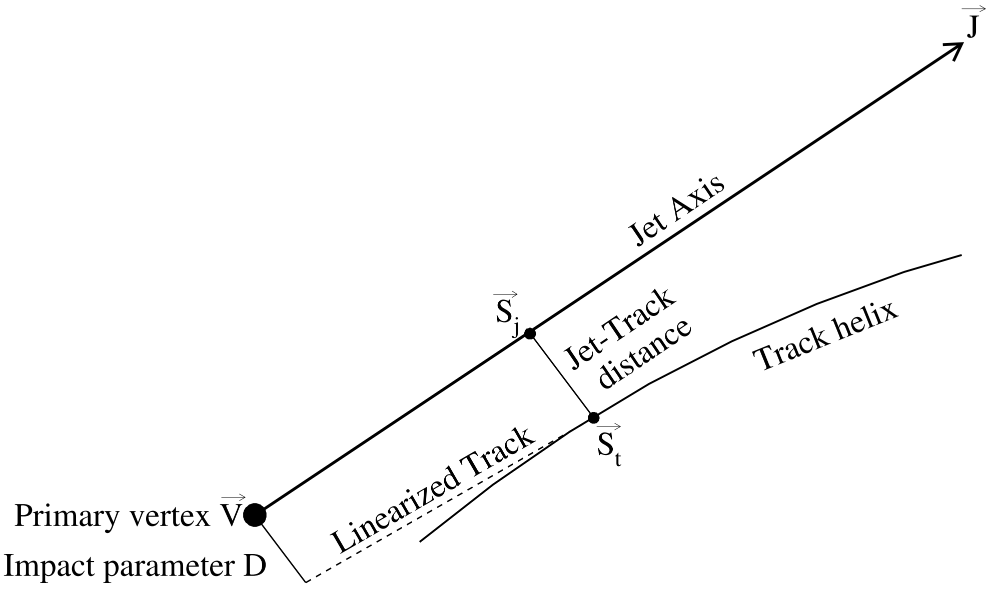

Figure 4.4: Definition of the signed impact parameter. See text for details.

from the primary vertex. The tracks with negative $\tilde{D}$ form a control sample that can be used to measure the resolution.

In the tagging algorithm, the statistical significance of the impact parameter of the tracks, defined as $\tilde{D}/\sigma_D$, is used. The uncertainty in D, σ_D, is computed from the error matrices of the track and primary vertex, plus their correlations. Since the error of the track is highly dependent on its angle, the number of VDET hits and the planes of the VDET that it traverses, using the normalized $\tilde{D}/\sigma_D$ allows to treat all the tracks nearly uniformly for all the angles and number of VDET hits.

The probability that a track comes from the primary vertex is then defined as

$$P_T(\tilde{D}/\sigma_D) = \int_{-\infty}^{-|\tilde{D}/\sigma_D|} dx\, \Re(x), \tag{4.5}$$

being $\Re(\tilde{D}/\sigma_D)$ the resolution function, the parametrization of the distribution of the impact parameter significance for tracks with negative value of $\tilde{D}$.

The same argument can be extended to a group of tracks forming a jet, a hemisphere or an event. The variable to compute, P_N, is the probability that any set of N tracks without lifetime produce the same set of observed probabilities or any other set of values equally or more unlikely. Being P_{T_i} the individual track probabilities, the differential probability for the observed set of variables to happen is given by

$$\mathcal{P} \equiv \prod_{i=1}^{N} P_{T_i}. \tag{4.6}$$

Considering that all the individual track probabilities belong to a N-dimensional space, P_N can be computed as

$$\begin{aligned} P_N &= \int_{(0,0,\ldots,0)}^{\prod_{i=1}^{N} x_i=\mathcal{P}} dx_1 dx_2 \ldots dx_N \\ &= 1 - \int_{\prod_{i=1}^{N} x_i=\mathcal{P}}^{(1,1,\ldots,1)} dx_1 dx_2 \ldots dx_N \\ &= 1 - \int_{\mathcal{P}}^{1} \int_{\mathcal{P}/x_N}^{1} \int_{\mathcal{P}/(x_N \cdot x_{N-1})}^{1} \cdots \int_{\mathcal{P}/(\prod_{i=2}^{N} x_i)}^{1} dx_1 dx_2 \ldots dx_N, \end{aligned} \tag{4.7}$$

where the x_i represent the probability of each track. Finally, P_N is given by [45]

$$P_N = \mathcal{P} \cdot \sum_{j=0}^{N-1} \frac{(-\ln \mathcal{P})^j}{j} \tag{4.8}$$

and represents the likelihood for the group of tracks of coming from the primary vertex.

4.4.2 Event shape tag

Events produced by the fragmentation of a b quark are expected to have different shape that the ones coming from light quarks or c quarks. In general, jets produced by a b fragmentation and decay are expected to have a larger opening angle due to the higher mass of the b hadron and the fact that they can decay to a charmed hadron that would decay afterwards to lighter hadrons, thereby randomizing the directions of the final particles. This can be used to classify different quark flavours.

Considering all the energy flow objects computed according to the algorithm explained in section 4.3, the thrust axis of the whole event, defined as the vector $\vec{T}$ which maximizes the thrust value

$$T = \frac{\sum_{i=1}^{n} |\vec{T} \cdot \vec{p_i}|}{\sum_{i=1}^{n} |\vec{p_i}|}, \tag{4.9}$$

where $\vec{p_i}$ is the momentum of the ith particle, is computed. The event is divided in two hemispheres according to the plane perpendicular to thrust axis and another thrust axis is computed for each hemisphere. In order to avoid correlations among hemispheres, only particles forming an angle below 45° with the thrust axis corresponding to the hemisphere they belong to are considered. The selected particles are boosted into the rest frame of each hemisphere before computing the two variables used: the moment of inertia and the lateral mass [46].

The moment of inertia is defined as the minimum eigenvalue normalized to the sum of the three eigenvalues of the inertial matrix which is computed according to

$$\lambda_{ij} = \sum_{m=1}^{n} \frac{-p_m^i p_m^j}{|\mathbf{p}_m|}, \quad i \neq j \tag{4.10}$$

and

$$\lambda_{kk} = \sum_{m=1}^{n} \frac{(p_m^i)^2 + (p_m^j)^2}{|\mathbf{p}_m|}, \quad k \neq i, j \tag{4.11}$$

where p_m^i is the ith component of the boosted momentum vector of the mth particle. The total momentum in the centre-of-mass frame of the b jets tends to be more uniformly distributed than the ones for lighter quark jets. Thus, b jets look more spherical and the three eigenvalues of the inertial matrix tend to be equal. In this case the moment of inertia tends to its maximum value of 1/3.

The lateral mass is intended to distinguish between products of gluon bremstrahlung and decay products in the final state based on the direction relative to the boost of the jet. It is defined as the sum of the boosted momenta of those particles in the hemisphere that make an angle with the hemisphere axis larger than $\cos^{-1}(0.75)$. The distribution of lateral mass for hemispheres produced from a b quark is peaked at higher values than for the other flavours.

Figure 4.5 shows the distribution for the moment of inertia and the lateral mass for different quark flavours. Using Monte Carlo, the likelihood that an hemisphere with a given moment of inertia and lateral mass comes from a $\mathrm{Z} \to \mathrm{b\bar{b}}$ event, l_h, is computed and this is the estimator used in the tag.

4.5 The event simulation

The different physics analyses use Monte Carlo simulated events to evaluate background contaminations, compute acceptances and efficiencies and, in general, com-

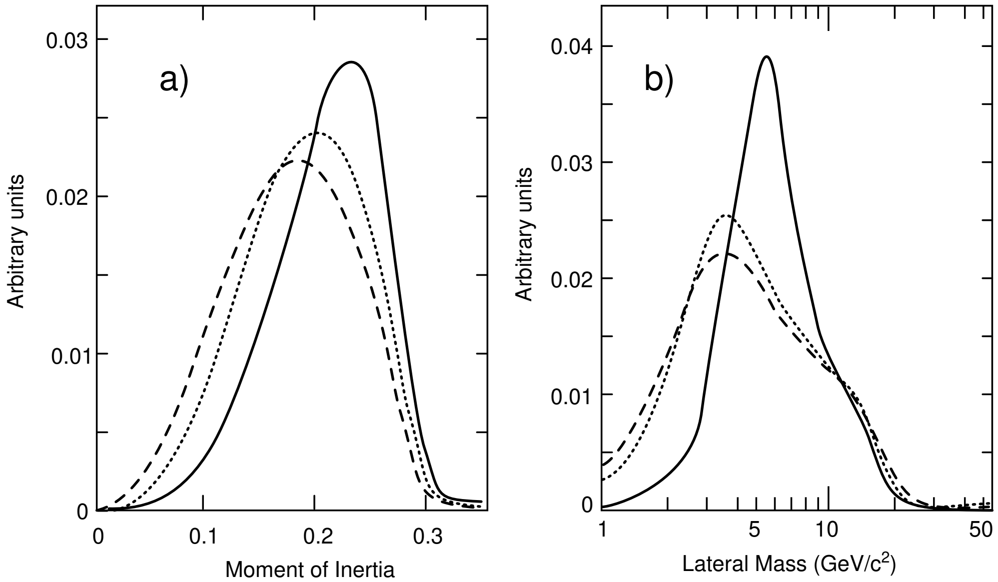

Figure 4.5: Distributions of quantities used in the event shape tag. (a) moment of inertia, (b) lateral mass, for different Monte Carlo events. the solid lines correspond to b events, the dotted lines to c, and the dashed ones to uds. (All curves are normalized to have the same area).

pare theoretical models to the experimental results. The chain to produce simulated events is as follows:

- Generation of the event kinematics. The particle four-momenta are generated according to the different physics processes (in parentheses the names of the computer programs used):

  - $e^+e^- \to \mu^+\mu^-$ (KORALZ [47]).
  - $e^+e^- \to \tau^+\tau^-$ (KORALZ).
  - $e^+e^- \to e^+e^-$ (BABAMC [48]).
  - $e^+e^- \to q\,\overline{q}$ (JETSET [49] + DYMU [50]).
  - $e^+e^- \to \ell^+\ell^-(\ell^+\ell^-)$ (PHOPHO [51], [52]).

  In ALEPH, all these programs have been unified through the common interface KINGAL [53].

- Simulation of the detector. This is done using a GEANT [54] based program (GALEPH [55]) where all the information about the geometry and materials involved in the experimental setup are described. For the tracking simulation, the primary long-lived particles are followed through the detector. Secondary particles are also produced by interaction with the detector material. Bremsstrahlung, Compton scattering and ionization are some of the processes simulated. GEANT and GHEISHA [56] are used to simulate the electromagnetic and nuclear interactions respectively. The energy depositions are converted to measurable electrical signals. The complexity of the TPC required the development of a special package (TPCSIM) for its tracking and digitization.

– Reconstruction. The same reconstruction program (JULIA [32]) used for the real data is used in the simulated events. Thus, the output of all the simulation processes has the same format as the real data.

4.5.1 Hadronic Monte Carlo models

The measurement of the different scaled energy distributions that will be presented in chapter 5 needs the use of all the event generators presented above. The ones that produce the dilepton events are only used for background studies and have a small impact in the measurement. The main detector efficiency correction and the correction for initial state radiation is made using the simulation of hadronic events.

The hadronic Monte Carlo simulation is done in four steps (figure 4.6). In the first one, the initial particles (electron and positron) produce an intermediate boson (γ or Z) that will decay into a $q\overline{q}$ pair. Initial and final state radiation is included in some models at this stage. Once the quark-antiquark pair is produced, the probabilities of quark and gluon emission obey perturbative QCD. The description of this stage constitutes the second step. This procedure continues until the momentum transfer to the following emission becomes small enough, typically 1 GeV, to be confronted with the limitations of perturbative QCD. Then the third step, hadronization, takes place: partons fragment and hadrons are formed. Being this process a non-perturbative phenomenon, some models have to be assumed. Finally, the produced hadrons are forced to decay according to the measured branching ratios to form the detected particles.

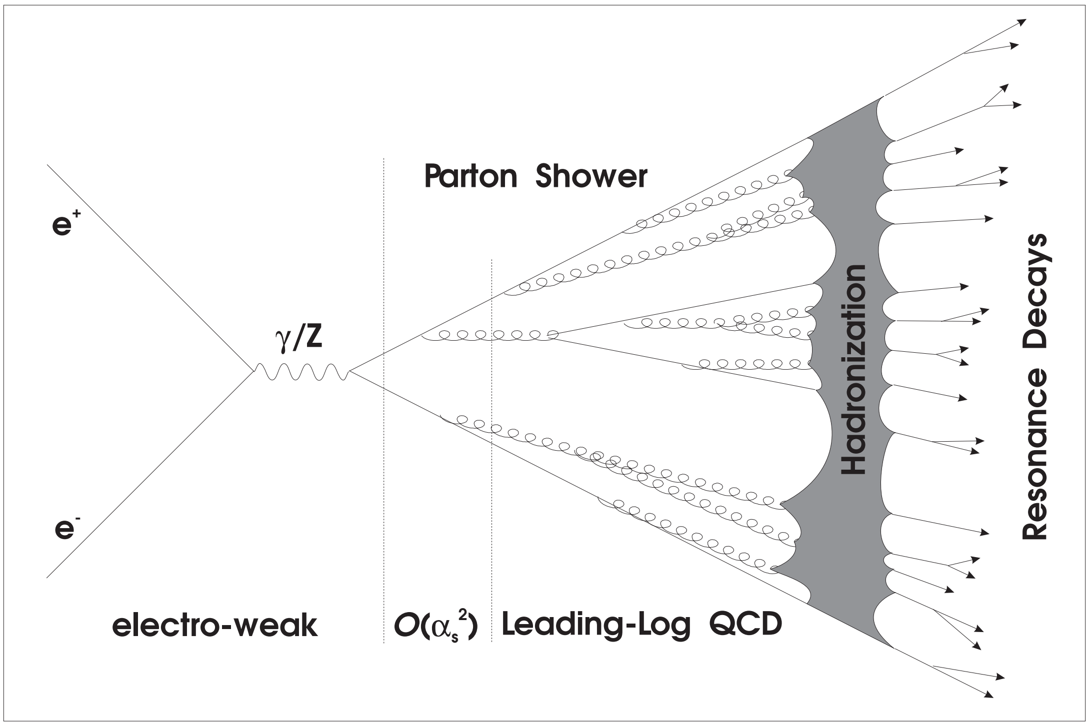

Figure 4.6: Schematic representation of a parton shower and hadronization. The four steps that lead to the formation of the final detected particles from the production of a quark-antiquark pair are presented.

Parton shower The perturbative phase can be computed with different approaches. In some models, as in the JETSET ME [57], calculations are made using the exact fixed second order QCD matrix element. However, these models can only generate 2, 3 or 4 partons in the final step. The non-perturbative phase has to fill the gap between this number of final partons and a higher multiplicity of hadrons, typically around 40 charged and neutral particles at LEP energies. Thus, these are not well suited for the description of the data at LEP energies. Instead, the parton shower picture is used.

The parton shower picture is based on an iterative use of the basic branchings, ie. $\mathrm{q} \to \mathrm{q}g$, $g \to gg$, $g \to \mathrm{q}\overline{\mathrm{q}}$. The momentum sharing between the daughter partons is determined by the Altarelli-Parisi splitting kernels (eqs. (B.19) to (B.22) in appendix B). These splitting kernels obey Altarelli-Parisi type equations. Thus the probability for a branching to take place at a given value of the evolution parameter, $t = \ln(Q^2_{evol}/\Lambda^2)$, is computed.

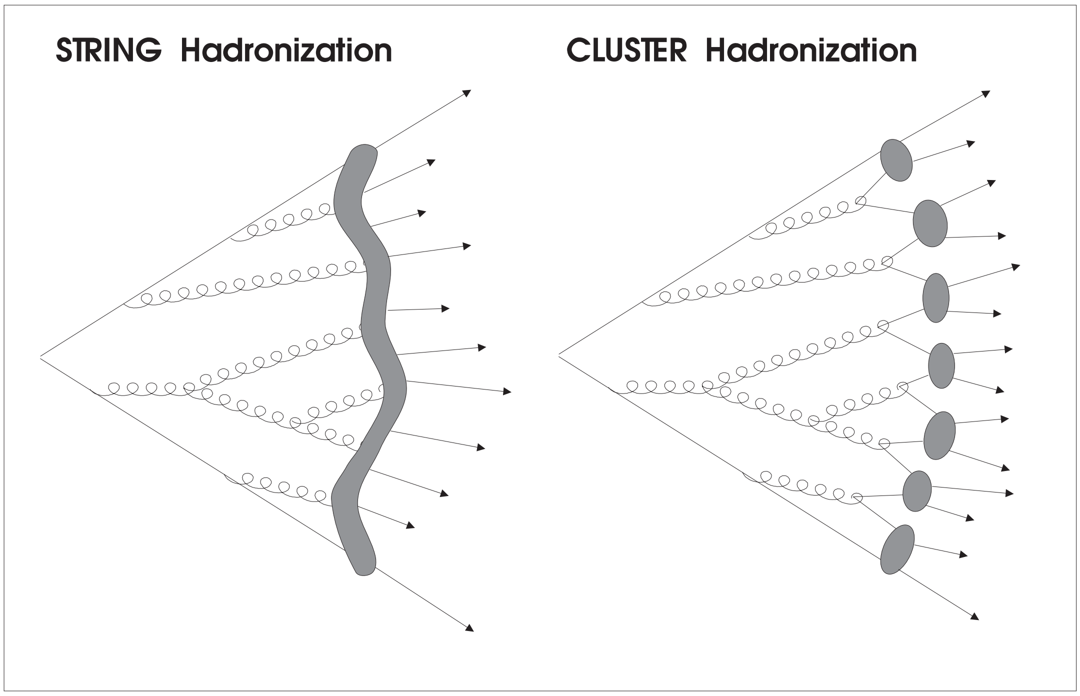

Figure 4.7: Representation of the string and cluster fragmentation.

The transverse momentum of the partons can be introduced assigning it independently in each subsequent branching, according to a gaussian distribution. This is called the incoherent parton shower approach. However, most of the models incorporate interference effects between subsequent splitting processes in the parton cascade. The usual way of doing this is by decreasing the emission angles of the subsequent partons in the shower. This is called the angular ordering effect and models that incorporate this feature are called coherent.

String fragmentation Different phenomenological models are used to describe the non-perturbative conversion of partons into hadrons. This process is called hadronization or fragmentation. The string model of fragmentation (figure 4.7) works in the following way. A string is stretched between a quark and an antiquark and a gluon is modeled as a kink on the string. As the quark and antiquark move apart, the potential energy stored in the string increases, and the string may break up by producing a new $q'\overline{q}'$ pair, so that the system splits into two colour singlet systems $q\overline{q}'$ and $q'\overline{q}$. If the invariant mass of either of these string pieces is large enough, they may further break.

In the Lund string model [58], the string breakup process is assumed to proceed until only on-mass-shell hadrons remain, each hadron corresponding to a small piece of string. The fraction of energy of the string taken by the hadron is modeled according to parametrized fragmentation functions. Usually, the symmetric fragmentation function

$$f(z) = \frac{(1-z)^a}{z}\exp(-bm_\perp^2/z) \tag{4.12}$$

where $m_\perp^2$ is the transverse mass of the hadron and with two free parameters, a and b, is used for the fragmentation of light quarks, while the Peterson fragmentation function [59]

$$f(z) = \frac{1}{z}\left[1-\frac{1}{z}-\frac{\epsilon}{1-z}\right]^{-2} \tag{4.13}$$

with a free parameter, ϵ, is used for the fragmentation of heavy quarks.

Cluster fragmentation Another hadronization model takes the final partons to form clusters. Before forming them, the gluons are forced to split into quark-antiquark pairs. Then, colour-neutral pairs of quarks that are close in phase space form massive clusters that decay isotropically into the observable hadrons (figure 4.7). The cluster fragmentation scheme is attractive as no explicit assumptions about fragmentation functions and the generation of transverse momenta are needed.

Monte Carlo models used in the analysis The ideas described so far for the perturbative phase of the parton shower formation and the fragmentation are combined in different ways in the models used in the analysis. A brief description of each follows:

JETSET PS [60] It is based in the parton shower picture and the string hadronization model. It includes angular ordering and matching of the first gluons emission to the exact $\mathcal{O}(\alpha_s)$ matrix element. This ensures that a hard radiation process in the initial phase of the parton shower is properly described.

NLLJET [61] In this model, the leading order splitting kernels are replaced by the next-to-leading ones. Thus, it contains $\mathcal{O}(\alpha_s^2)$ corrections to the $2 \to 2$ splitting functions and includes also $2 \to 3$ splitting processes. The hadronization is controlled by the string fragmentation scheme.

HERWIG [62] The parton shower includes interjet interference and gluon polarization effects. The hadronization phase is done following the cluster model.

ARIADNE [63] This model implements an alternative way to formulate the parton showering process as colour-dipole radiation which includes matching to the $\mathcal{O}(\alpha_s)$ matrix element, angular ordering and some azimuthal correlations between jets automatically. The initial quark-antiquark is considered as a colour-dipole that radiates a gluon according to the leading-order QCD matrix element. This gluon splits the initial dipole into two secondary ones. Iterating this process gives rise to the parton shower. The partons are then fragmented into hadrons according to the string fragmentation model.

HVFL This is no more than the JETSET PS model interfaced with DYMU to produce the initial quark-antiquark pair. This includes a better description of initial and final state radiation and, partially, the interference terms between them. Being the standard ALEPH Monte Carlo model, it also contains a fine tuning of the heavy flavour decay branching ratios to better describe the data.

Chapter 5

Data analysis

This chapter describes the data used in the analysis. It is important to have as much information as possible for different quark-flavour samples. Thus, light uds-, c- and b-flavour enriched scaled energy distributions are measured besides the scaled energy distribution for all flavours that gives the information for the evolution of the fragmentation functions. The procedures for the selection of events, correction for detector effects and estimation of the systematic errors are explained in sections 5.1, 5.2 and 5.3. The estimation of the correlation errors among all the distributions is explained in section 5.6. Useful information on the gluon fragmentation function is obtained in the analysis of three jet events and the measurement of the longitudinal and transverse scaled energy distributions. These measurements are described in sections 5.4 and 5.5, respectively. Finally, the scaled energy distributions measured at lower energies by other experiments than ALEPH, and the assumptions made in their normalization errors are described in section 5.7.

5.1 Selection of hadronic events

Before any flavour identification is attempted, a good selection of hadronic events has to be made. Since the interest is in the scaled energy distribution and the available statistics of around 20 tracks per event is rather high, the interest of the global selection is in avoid possible biases that would result in high correction factors rather than in optimizing the selection efficiency.

For each event, only charged tracks with more than 4 TPC hits, originated in a cylinder of radius $d_0 = 2\,\mathrm{cm}$ and length of $z_0 = 10\,\mathrm{cm}$ around the interaction point, forming an angle with the z axis, θ, between 20° and 160°, and with a transverse momentum, p_t, with respect to the z axis exceeding 0.2 GeV/c are considered in the analysis. Tracks passing these requirements are called good tracks. An hadronic event should have more than four of these good tracks and the sum of their energy, assuming they have the pion mass, must be above 15 GeV.

The sphericity axis, defined as the eigenvector corresponding to the minimum eigenvalue of the tensor

$$S^{ab} = \frac{\sum_i p_i^a p_i^b}{\sum_i p_i^2} \tag{5.1}$$

is computed in the events passing the above selection cuts. Only those events in which the polar angle of the sphericity axis, θ_{sph} lies between 35° and 145° are accepted. Since the opening angle of a jet is roughly 15°, this cut avoids larger correction factors removing those events that would not be fully contained in the detector acceptance.

A total of 911539 events from 1992 and 1993 LEP run periods with a centre-of-mass energy around 91.2 GeV fulfil the requirements to be considered hadronic events, the selection efficiency being 77%. The background was estimated from Monte Carlo, being the main contribution the one coming from tau pairs (0.3%), the ones from Bhabha and dimuon events being negligible. No Monte Carlo two photon event passed the selection cuts.

5.2 Scaled energy inclusive distribution

For each event, the variable $x_E = E_{tr}/E_{beam}$ (called x in the following), is computed for each charged good track, with E_{tr} being the energy of the track assuming the pion mass.

The raw data distribution is normalized to the total number of events such that, for each bin

$$\sigma_{i,raw} = \frac{1}{N_{events}} \frac{N_i^{tr}}{\Delta x_i} \tag{5.2}$$

where N_i^{tr} is the number of tracks such that its variable x lies within the bin interval, and Δx_i is the width for bin i.

At each value of x, the bin width was chosen to be four times the momentum resolution of the tracks in order to avoid a large migration of tracks to the neighbouring bins. Since the momentum resolution increases with energy, the bin width is different for different values of the variable x. In the low momentum region, the general rule of four times the momentum resolution for the bin width would result in too main bins. For this reason, below $x \sim 0.4$ wider bins were used in the histograms.

The raw distribution is corrected, using Monte Carlo methods, for effects of geometrical acceptance, detector efficiency and resolution, decays of long-lived particles (with $\tau > 1\,\text{ns}$), secondary interactions and initial state photon radiation. Thus, the scaled energy distribution is defined as the distribution for charged tracks obtained if all particles with a mean lifetime $\tau \leq 1\,\text{ns}$ decay while the others are stable.

To perform the correction, hadronic events were generated using the generator HVFL (section 4.5.1). Initial state radiation is included in the simulation. The generated events were passed through the detector simulation and reconstruction program as explained in section 4.5. The same procedure was performed for τ, Bhabhas, dimuon and two photon events using KORALZ, BHABHA and PHOPHO as generators. The same selection and analysis procedure was performed for the simulated data, and distributions $\sigma_{i,sim}$ containing the hadronic events and all the background sources, were constructed.

Hadronic events were also generated using the HVFL generator with neither initial state radiation nor detector simulation and with the requirement that all particles with mean lifetimes $> 10^{-9}\,\text{s}$ are stable. All charged particles were used to construct the $\sigma_{i,gen}$ distribution were, in the computation of x, the true mass of the particle is used.

Corrected data distributions were obtained using the bin-by-bin ratio of the generated and simulated distributions according to

$$\sigma_{i,corr} = C_i \cdot \sigma_{i,raw} = \frac{\sigma_{i,gen}}{\sigma_{i,sim}}\, \sigma_{i,raw} \,. \tag{5.3}$$

The distributions were corrected separately for the 1992 and 1993 data taking periods to take into account the proper detector configuration for each year. Afterwards, both corrected distributions were combined.

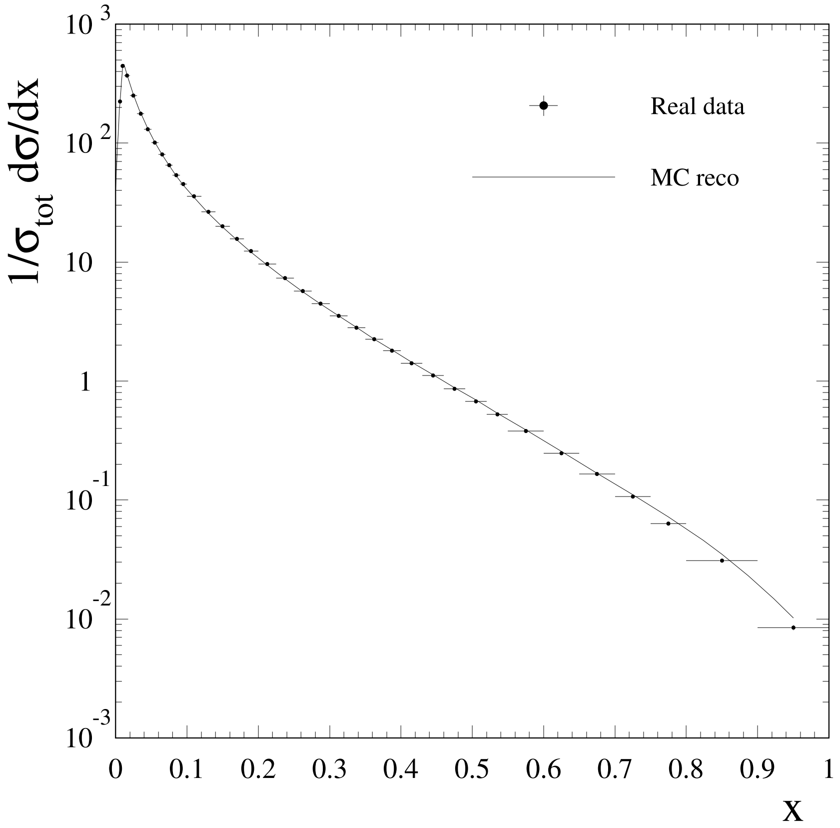

Figure 5.1: All-flavour uncorrected distribution and comparison with reconstructed Monte Carlo. The background from τ's, dimuon and Bhabha events is included in the Monte Carlo. Only statistical errors are considered which turn out to be too small to be seen in the plot.

Although this correction procedure can induce a small bias towards the model, the fact that the simulated and raw data agree, as seen in figure 5.1, and that the correction factors are relatively small indicate that this bias is not large. Figure 5.2(a) shows the correction factors, C_i, applied to the distribution of all flavours. They are around 1.07 or below in almost the whole interval, except the bins at larger momentum. This is due to the TPC momentum smearing. The resolution in the TPC is nearly gaussian in the inverse of the momentum. The resolution function can be written as

$$\mathcal{R}(p_{\text{meas}}, p_{\text{true}}) = \frac{1}{p_{\text{meas}}^2} \exp\left[-\left(\frac{1/p_{\text{meas}} - 1/p_{\text{true}}}{\sqrt{2}\sigma_{1/p_{\text{true}}}}\right)^2\right], \tag{5.4}$$

where p_{meas} is the measured momentum and p_{true} is the true momentum of the charged track. The resolution distribution has a long tail at large momentum. Thus, large momentum bins tend to be more populated from low momentum tracks.

Standard cut	Variation 1	Variation 2
$N_{\rm TPC} \geq 4$	$N_{\rm TPC} \geq 3$	$N_{\rm TPC} \geq 5$
$d_0 \leq 2.0\,{\rm cm}$	$d_0 \leq 1.5\,{\rm cm}$	$d_0 \leq 3.0\,{\rm cm}$
$z_0 \leq 5.0\,{\rm cm}$	$z_0 \leq 3.0\,{\rm cm}$	$z_0 \leq 10.0\,{\rm cm}$
$20^\circ \leq \theta_{\rm track} \leq 160^\circ$	$30^\circ \leq \theta_{\rm track} \leq 150^\circ$	$15^\circ \leq \theta_{\rm track} \leq 165^\circ$
$p_t \geq 200\,{\rm MeV}$	$p_t \geq 150\,{\rm MeV}$	$p_t \geq 400\,{\rm MeV}$
$N_{\rm good} \geq 5$	$N_{\rm good} \geq 4$	$N_{\rm good} \geq 7$
$E_{Ch} \geq 15\,{\rm GeV}$	$E_{Ch} \geq 10\,{\rm GeV}$	$E_{Ch} \geq 25\,{\rm GeV}$
$35^\circ \leq \theta_{\rm spher} \leq 145^\circ$	$45^\circ \leq \theta_{\rm spher} \leq 135^\circ$	$65^\circ \leq \theta_{\rm spher} \leq 155^\circ$

Table 5.1: Definition of the cuts for the standard analysis and the variation made for the systematic errors estimation. Each cut was varied at once taking, alternatively, the values in the two columns labelled as *Variation 1* and *Variation 2*, and the analysis was repeated for each combination. The rest of the cuts remain at their standard values.

This effect is amplified by the fact that the scaled energy distribution falls off rather steeply with x, and therefore, for a given x, contamination from lower energy bins is much more likely than from higher energy bins. This effect makes the correction factor in the last bins to be even below 0.8.

Two types of systematic uncertainties were taken into account. The first one is due to possible discrepancies between the real and the simulated detector performance. The second one comes from the fact that the QCD generator chosen to calculate the correction factors might not fully reproduce the data, and then the corrected data could result biased to the model used in the QCD generator.

To estimate the uncertainties of the first kind, all the selection cuts were varied, once at a time, taking alternatively the values listed in table 5.1, and the same correction and combination procedure was used to produce analogous corrected distributions for each set of cuts. In each bin, the maximum change with respect to the corrected distribution with the standard set of cuts was taken as the systematic error. Figure 5.3 shows these differences in number of statistical standard deviations of the reference distribution. The maximum variation comes from the change in the cuts in the angle of the sphericity axis and from accepting events with four good tracks. The large difference at large x seen when accepting events with four good tracks could be due to the background of two-photon events that was not subtracted in this procedure, since it was found to be negligible when requiring five good tracks in the nominal analysis. Most of the differences are below one

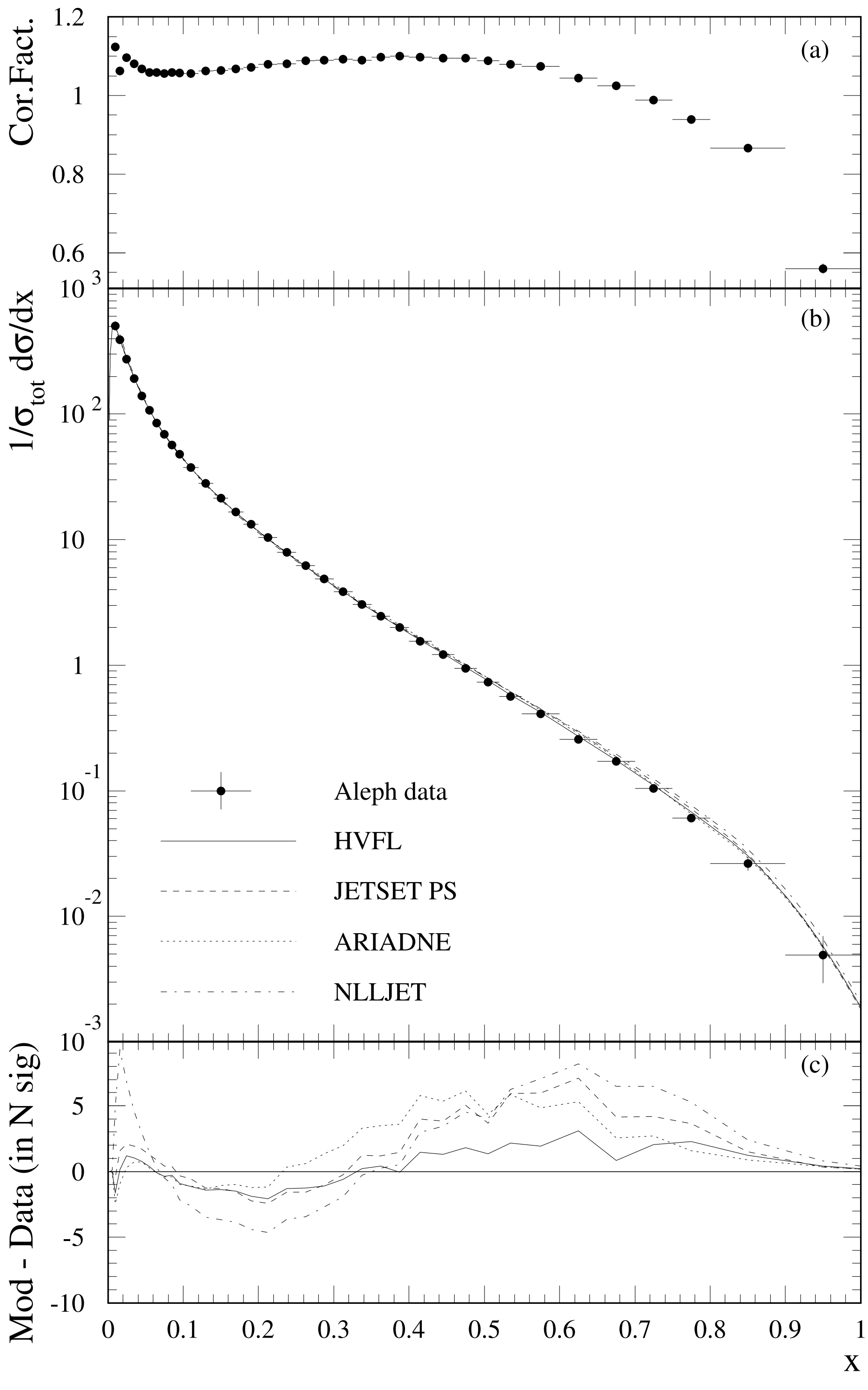

Figure 5.2: Correction factors applied to the all-flavour inclusive energy distribution(a), corrected distribution compared with predictions from Monte Carlo models (b), and deviation of the models from the corrected data measured in number of standard deviations, where the error includes statistical and systematical sources (c).

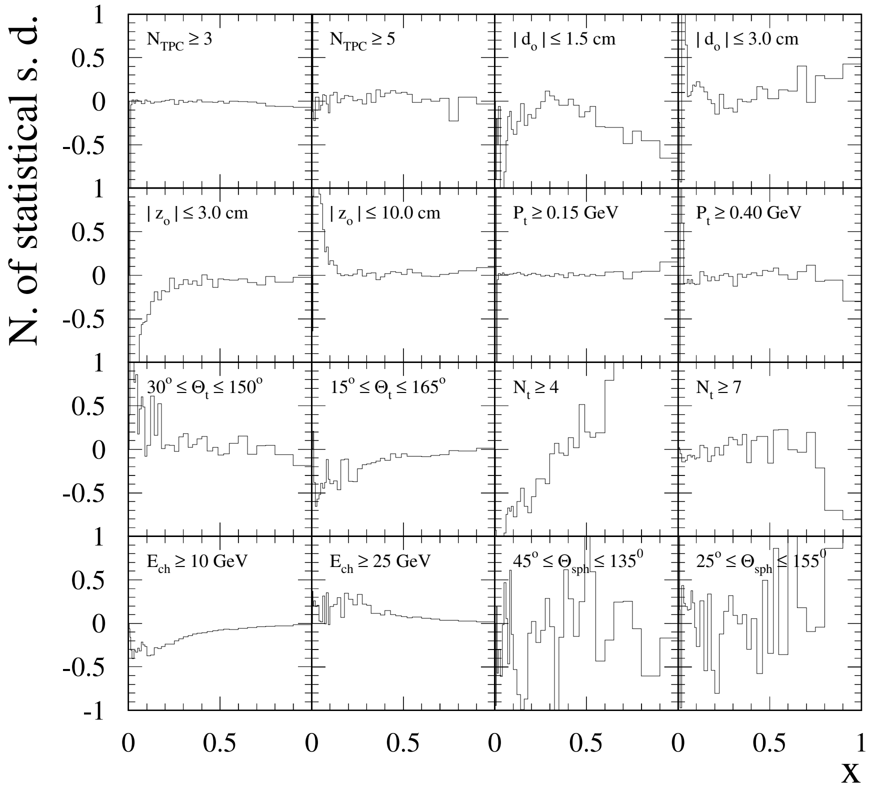

Figure 5.3: Differences between the distribution constructed with the standard selection cuts and the ones varying one of the cuts at a time. This difference is shown in number of statistical standard deviations of the reference distribution.

statistical standard deviation showing the robustness of the selection criteria. The analysis of these variations shows no significant correlation among different bins in the x distribution.

To estimate the systematic uncertainties coming from the QCD generator chosen, a simplified method which does not use the full detector simulation was applied. Five million events were generated using the ARIADNE, NLLJET and JETSET PS generators (section 4.5.1). HERWIG was not used in this procedure because the available version, 5.6, simulates a much softer scaled energy distribution than the data. Thus, including it would give rise to an artificial increase in the systematic uncertainties.

Simplified correction factors were computed for each model using the ratio of the generated distribution and the distribution containing tracks and events that fulfil the same selection criteria that for the standard data. Figure 5.4 shows these

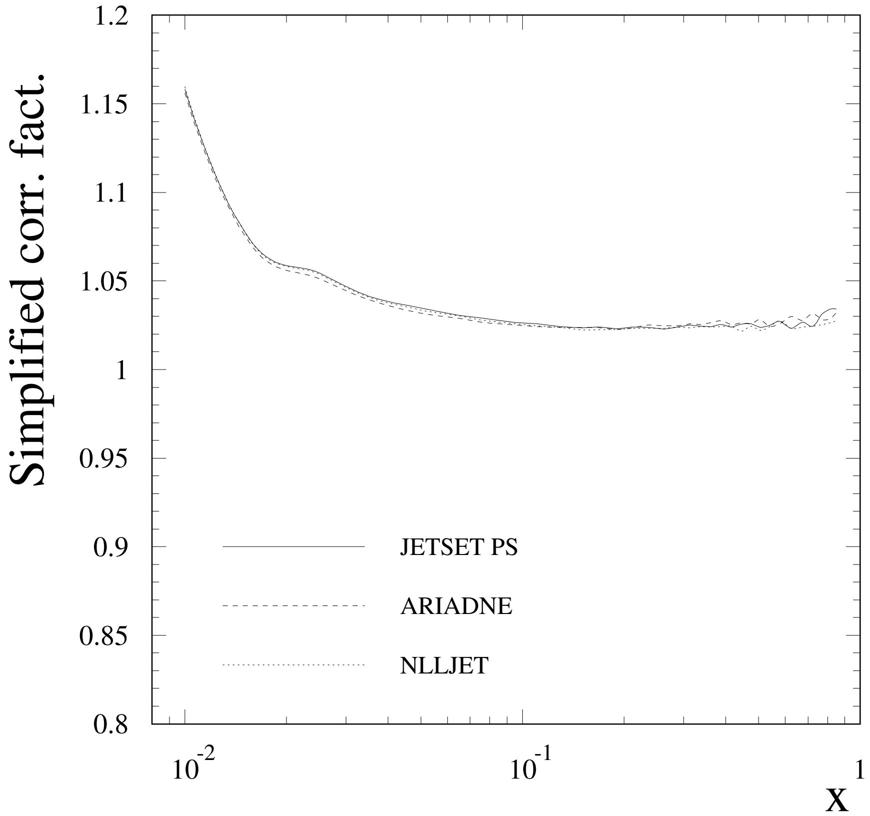

Figure 5.4: Simplified correction factors for the all-flavour energy distributions constructed with three different Monte Carlo models: JETSET PS, ARIADNE and NLLJET.

simplified correction factors for the three Monte Carlo models used to compute this systematic error source. The fact that no TPC smearing resolution and efficiency is taken into account in this simulation makes these simplified correction factors to be closer to one than the ones coming from the full simulated distributions. Nevertheless, it is expected that if all the detector effects would be included, the differences between the models would remain the same and that the maximum relative difference between the simplified correction factors is a good estimation of the systematic error coming from this QCD generator dependence.

The statistical error and the systematics coming from the limited statistics of the Monte Carlo used to perform the correction procedure, the selection cut variation and the QCD model dependence were added in quadrature to compute the total bin-by-bin error of the distribution. A common normalization error of 1%, which is correlated, not only in all the bins, but also in all the distributions is also added in quadrature to the total error. The estimation of this source of error is explained in section 5.6.1. Table C.1 in appendix C lists the cross-section and all the error contributions for all the bins. The systematic error dominates everywhere. The normalization error dominates over the bin-to-bin error below $x = 0.5$. From the three contributions to the bin-to-bin systematic error, the one coming from the differences in the Monte Carlo models dominates below $x = 0.1$ but above this point, this source of systematic error tends to be equal or smaller than the one coming from the selection cut variation. The systematic error coming from the finite Monte Carlo statistic is comparable to the cut variation systematic in the whole particle energy interval.

Figure 5.2(b) shows the corrected scaled energy distribution for the normal flavour composition. The continuous lines show the prediction of several Monte Carlo models. The differences between the corrected data and the different models can be seen in more detail in figure 5.2(c) where the quantity $(\mathrm{Model} - \mathrm{Data})/\mathrm{Error}_{\mathrm{data}}$, being $\mathrm{Error}_{\mathrm{data}}$ the total statistical and systematic error of the distribution (included the normalization error), is plotted for the different models. While the HVFL Monte Carlo, which is the one used in the correction procedure, differs by less than three standard deviations in the whole energy range, the rest of models disagree up to eight standard deviations, especially in the high x region. The reason for this should be assigned to better parameter tuning of the HVFL Monte Carlo, especially in the heavy flavour hadron decay branching fractions.

5.3 Flavour enriched distributions

Since the distributions for the light quarks (u,d,s) are expected to be almost indistinguishable, three different enriched flavour distributions were prepared: for light, c and b quarks. This section describes the measurement of these enriched flavour distributions using the two tagging algorithms described in section 4.4.

To prepare the enriched flavour distributions, the same selection cuts as described in section 5.1 were first applied. The selected events were then divided in two hemispheres separated by the plane perpendicular to the thrust axis. The two flavour tags described in sections 4.4.1 and 4.4.2 were applied to the two hemispheres of the event giving the estimators P_H and l_H, respectively, for each hemisphere.

The impact parameter tag algorithm is more efficient for events with large charged multiplicity. Thus, in order to reduce the bias introduced by this tagging algorithm, the algorithm is applied only to the tracks of one hemisphere. If that hemisphere passes the selection cut, the other one is used to measure the charged particle spectrum, weighting each track with a factor of two. The cross sections are normalized to the number of accepted hemispheres. Finally, since the two hemispheres are almost independent, the procedure is repeated with the tag applied to the second hemisphere. The same procedure is used when applying the event shape tag.

The procedure described above makes the assumption that the correlation of the tag between hemispheres is small. It can be shown that, for the lifetime tag [45], this correlation is smaller than one per cent for the cut in P_H used in this analysis. In the case of the event shape tags, these correlations are already small by construction, since only particles forming and angle below 45° with the jet axis are used in the variables. Residual correlations between the hemispheres are taken into account in the correction procedure.

A sample enriched with bottom-quark events is obtained requiring $P_H < 0.001$, which results in a b-identification efficiency of about 32.5%. The flavour composition of the tagged sample is 90.5% of bottom quarks, 7.3% of charm quarks and 2.2% of light quarks, according to the Monte Carlo. It has been checked [64] that the Monte Carlo efficiencies and purities agree well with those in the data.

Using the same technique, a light-quark enriched sample has been prepared. In this case, the hemisphere probability to come from the interaction point is required to be $P_H > 0.1$. The light-quark efficiency is about 74%, and the tagged sample consists of 78.9% light-quark events, 14.5% charm events and 6.6% bottom events.

A sample enriched in c-quark events is obtained requiring $0.001 < P_H < 0.07$. In order to increase the purity, the global hemisphere-shape variables described in section 4.4.2 were also used. The value of the likelihood, l_H, was required to be below 0.2. The final sample consists of 35.1% charm events, 26.7% bottom events and 38.2% light-quark events. The efficiency for c-quark tagging is about 9%.

The correction procedure described in section 5.2 was applied. The systematic errors were estimated with the method described there. Systematic effects coming from the possible defects in the simulation of the flavour tag will be taken into account in the α_s measurement (section 6.7.1).

The corrections were made using distributions generated with the same flavour composition as the ones resulting applying the different tag algorithms to the Monte Carlo sample after detector simulation. Figures 5.5, 5.6, 5.7(a) show the correction factors applied in the enriched flavour distributions for b, c and light quarks, respectively. While below $x \sim 0.6$, they are comparable to the ones shown in figure 5.2(a) corresponding to the all-flavours distribution, differences arise above this limit, especially for the b-enriched distribution (figure 5.5(a)), where the correction factors for some bins have values around 0.5. This effect can be explained again by the TPC momentum smearing described in section 5.2. The more steeply falling distribution for the b-enriched sample accentuates the effect, while the harder momentum distribution of the light quarks gives correction factors very similar to the ones for the all flavour distribution.

Figures 5.5, 5.6, 5.7(b) and (c) show the corrected distributions and their comparison with the different Monte Carlo models. The larger discrepancies that arise in the b-enriched flavour distribution should be attributed to a lack of branching ratio tuning in the ARIADNE, JETSET and NLLJET Monte Carlos, as it was pointed out in section 5.2. The good agreement seen for the c-enriched flavour distribution (fig. 5.6(c)) should be attributed to its larger errors rather than to a better agreement with the Monte Carlo models.

Figure 5.8 plots the measured ALEPH distributions. One clearly sees the difference between light and heavy flavour enriched samples. The errors include all bin-to-bin errors (statistical and systematic) added in quadrature as well as an overall 1% normalization error. Systematic errors dominate everywhere. The agreement with the HVFL Monte Carlo prediction is reasonable for all distributions and x regions.

Tables C.2,C.3,C.4, in appendix C list the cross section and all the error contributions for all the bins for the flavour enriched distributions. For the uds-enriched distribution, the dominant bin-to-bin error is of systematic origin. This is not the case for the c- and b-enriched distributions where statistical and systematic bin-to-bin errors become comparable. As in the case of the non flavour scaled energy distribution, the normalization error dominates over the bin-to-bin systematic error for the low x region ($x \leq 0.3$) for all the flavour tagged distributions. Among

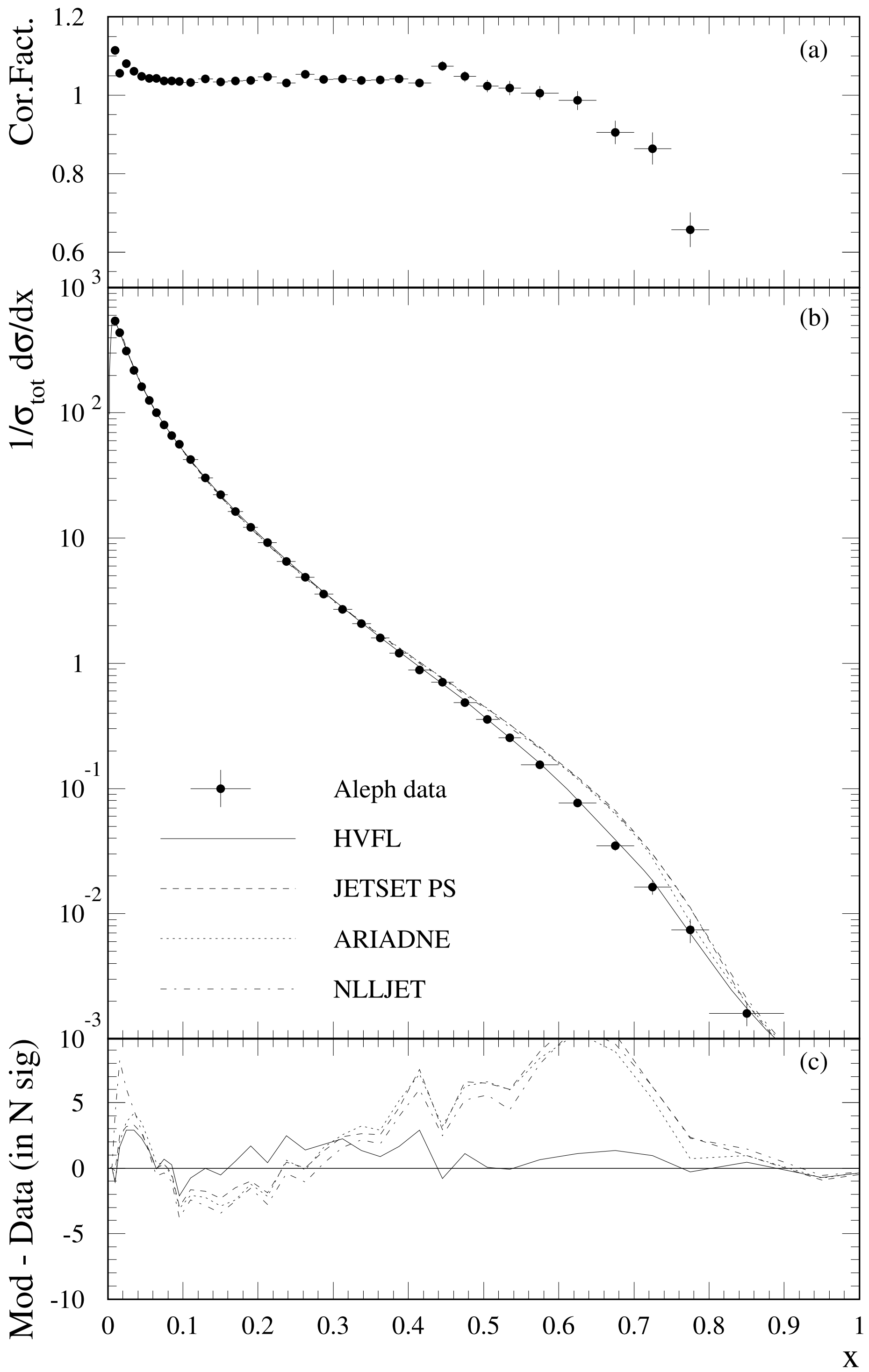

Figure 5.5: Correction factors applied to the b-enriched scaled energy distribution(a), corrected distribution compared with predictions from Monte Carlo models (b), and deviation of the models from the corrected data measured in number of standard deviations (including statistical and systematic error) (c).

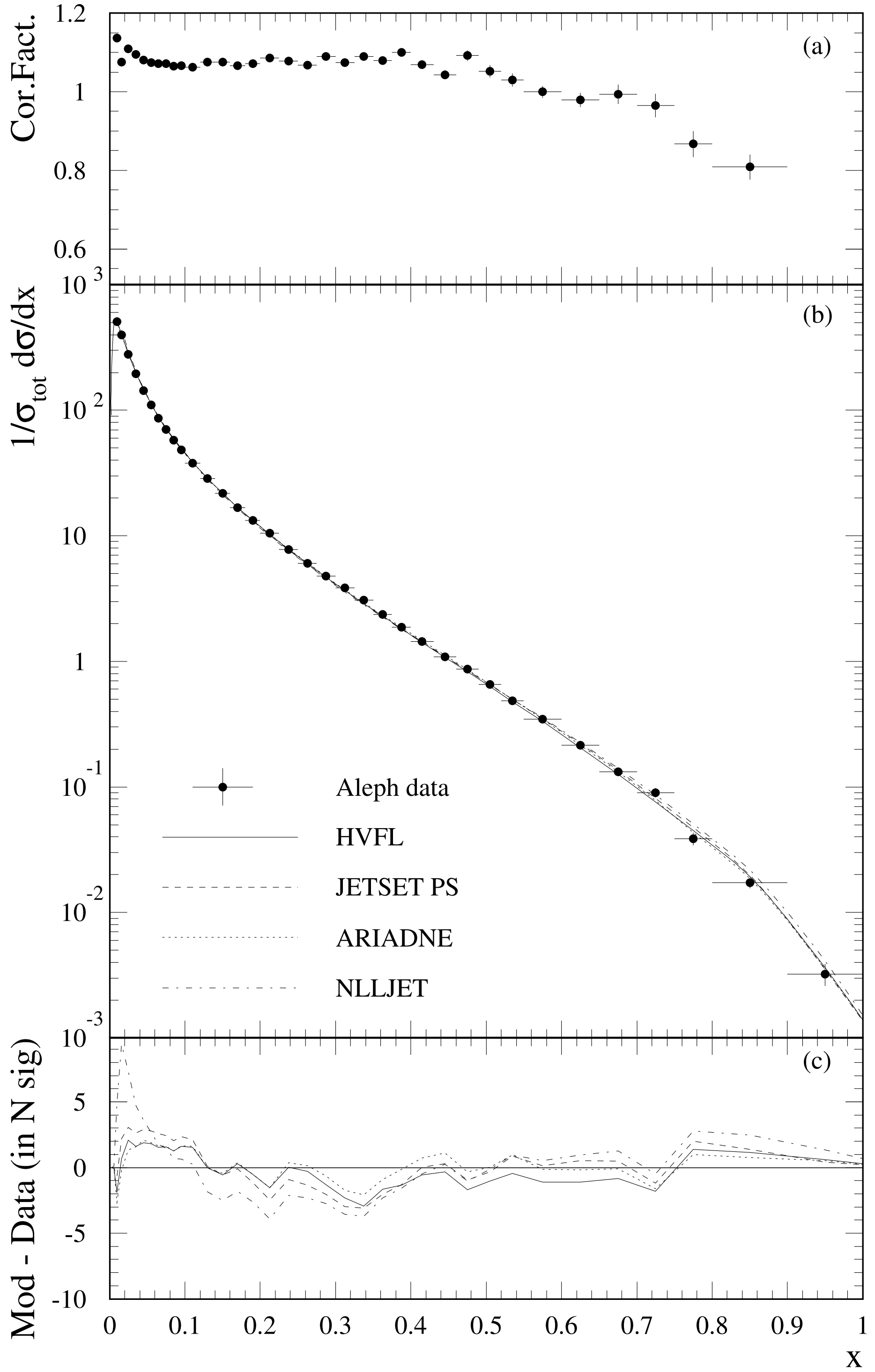

Figure 5.6: Correction factors applied to the c-enriched scaled energy distribution(a), corrected distribution compared with predictions from Monte Carlo models (b), and deviation of the models from the corrected data measured in number of standard deviations (including statistical and systematic error) (c).

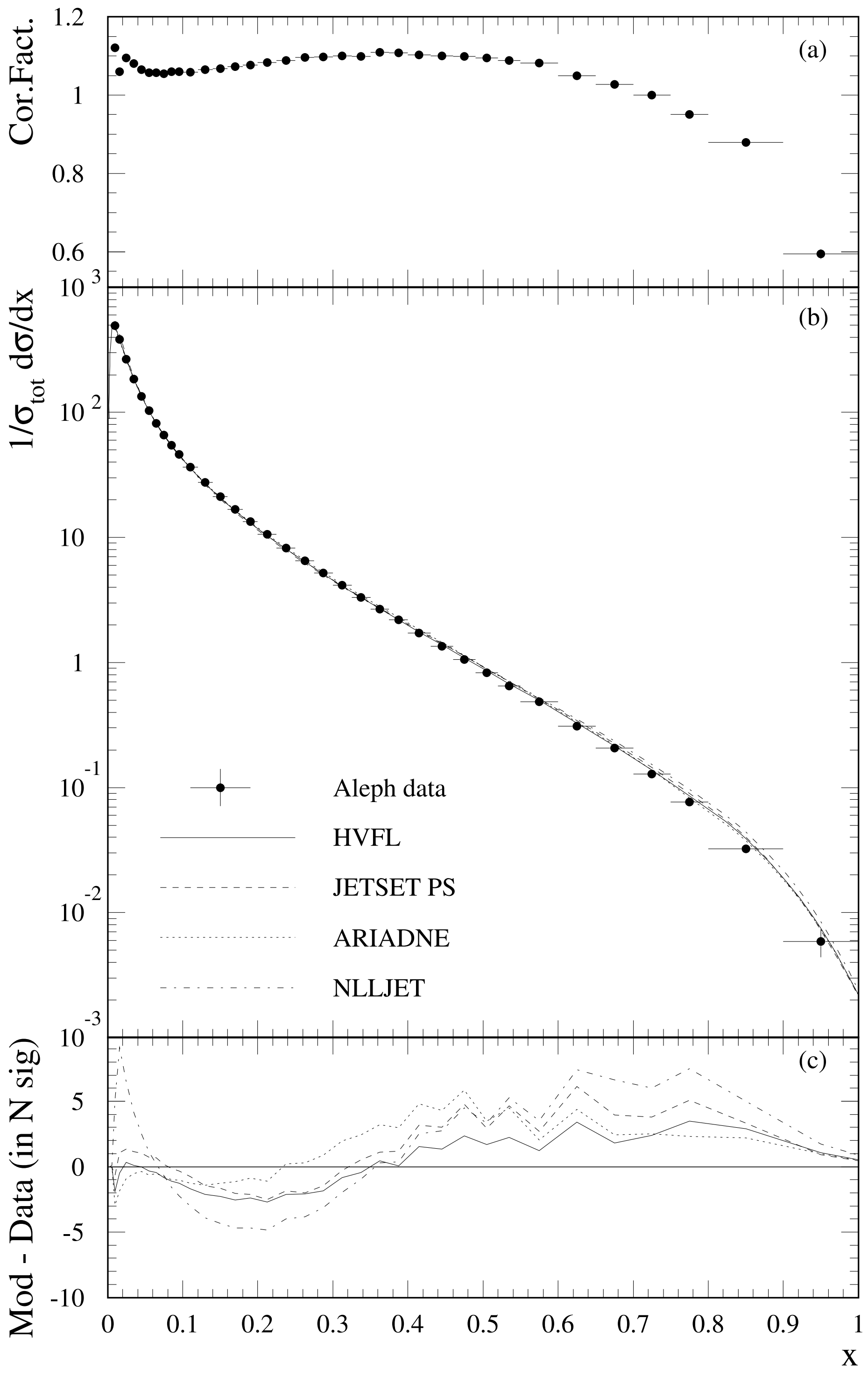

Figure 5.7: Correction factors applied to the uds-enriched scaled energy distribution(a), corrected distribution compared with predictions from Monte Carlo models (b), and deviation of the models from the corrected data measured in number of standard deviations (including statistical and systematic error) (c).

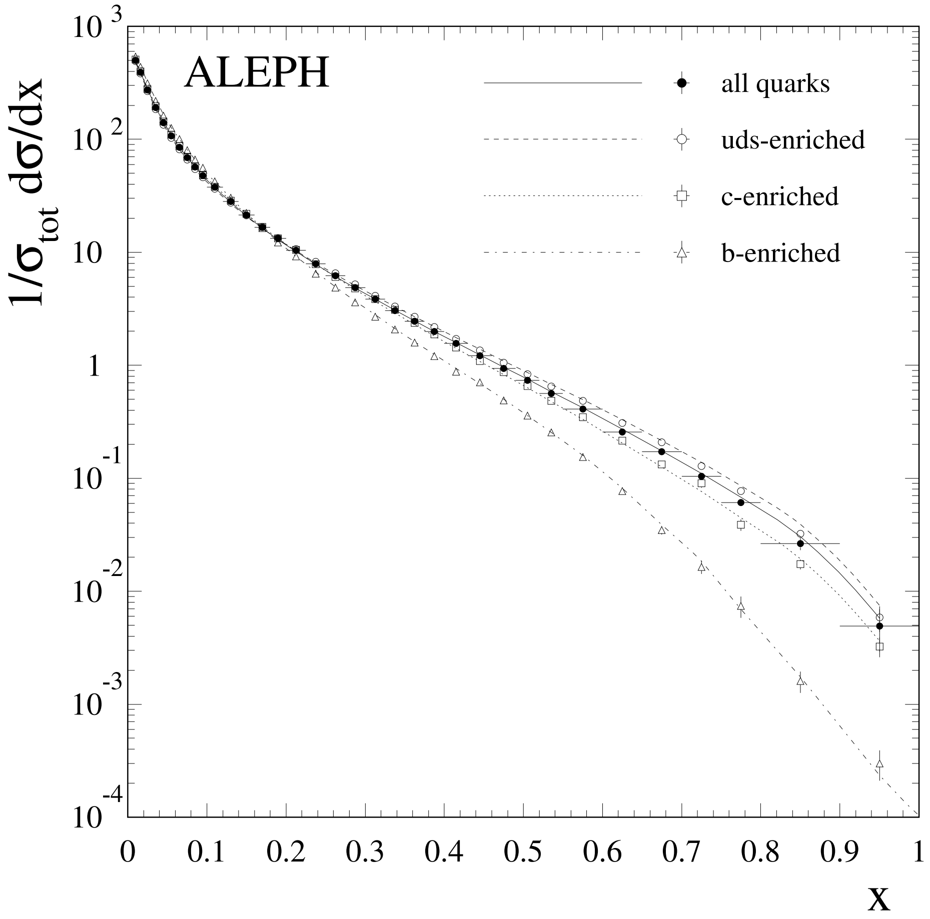

Figure 5.8: Measured scaled energy distributions corrected for detector effects (symbols) and comparison with the predictions from HVFL. The distributions are normalized to the total number of events. Error bars include statistical and systematics uncertainties. The same binning is used for all distributions.

the sources of bin-to-bin systematic errors, the dominant one is the cut variation, although for the c- and b-enriched distributions, the one coming from the limited statistics of the Monte Carlo used to perform the correction is of similar magnitude.

5.4 Gluon distribution from three-jet events

The analysis of scaling violations needs not only information of the fragmentation function for different flavours but also the shape of the gluon fragmentation function that enters in the evolution equations described in section 2.3.

The gluon fragmentation function can be extracted directly from the data using three jet symmetric events [65]. These events are characterized by two of the jets having essentially the same energy and the angular separation between any of the two lower energetic jet and the highest energetic jet being in the range $150^0 \pm 7.5^0$.

The most energetic jet has a high probability of originating from a quark or an antiquark. To identify the gluon jet from the two lower energy jets a b anti-tagging method is used. If one of the two jets contains long-lived particles, it is associated with a heavy quark jet. The remaining jet is then tagged as the gluon jet.

Two samples of jets are prepared. In the symmetric (S) sample no gluon jet tagging is applied and contains the two lower energetic jets from all the events. This untagged mixture contains $P_g^S = 48.5\%$ of gluons and 51.5% of quarks as computed by Monte Carlo. In the tagged (T) sample, only those jets not tagged as coming from a b quark are considered. The gluon purity in this sample is $P_g^T = 90.0\%$.

Any observable, A, can be measured in both samples. The measurement for gluons and quarks, A_g and $A_{\rm q}$, can be extracted from the following relations for the S and T samples

$$A^S = P_g^S \cdot A_g + (1 - P_g^S) \cdot A_{\rm q} \tag{5.5}$$

$$A^T = P_g^T \cdot A_g \cdot \delta A_g + (1 - P_g^T) \cdot A_{\rm q} \cdot \delta A_{\rm q} \tag{5.6}$$

where $\delta A_{g({\rm q})}$ is a measurement of the bias coming from the fact that the tagged sample is largely enriched in jets coming from b quarks. This bias has to be estimated from Monte Carlo and is given by

$$\delta A_{g({\rm q})} = \frac{A_{g({\rm q})}^{MC,T}}{A_{g({\rm q})}^{MC,S}}, \tag{5.7}$$

where $A_{g({\rm q})}^{MC,T}$ and $A_{g({\rm q})}^{MC,S}$ are the Monte Carlo measurements for correctly identified gluons (quarks) jets in the tagged and symmetric configurations. Further details of the procedure to estimate the purities and the corrections can be found in ref. [65].

The inclusive charged particle momentum distribution of the gluon jet, scaled to its energy, is extracted using the technique described above. It is presented in figure 5.9 and in table C.5 in appendix C. The mean energy of the gluon jets is 24 GeV.

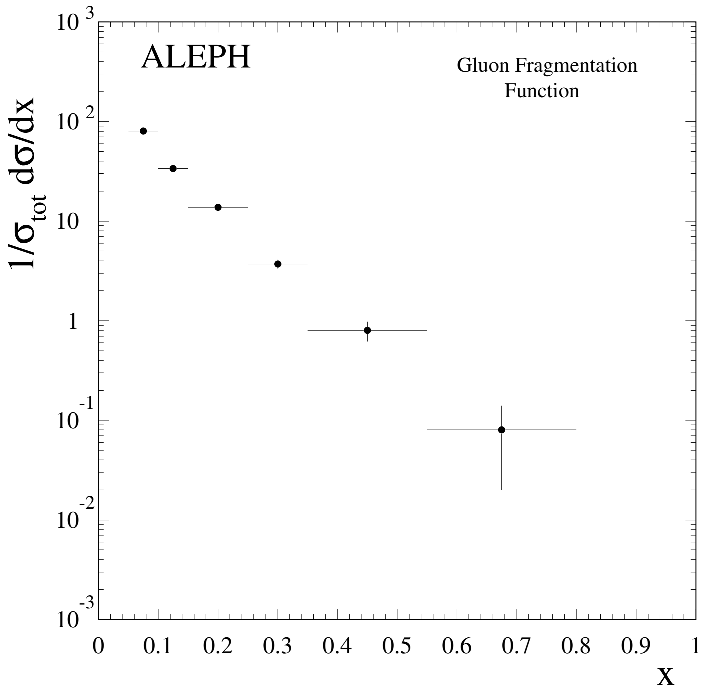

Figure 5.9: Gluon scaled energy distribution measured in three jet symmetric events [65]. The average energy of the gluon jet is 24 GeV.

5.5 Transverse and longitudinal distributions

The longitudinal and transverse cross sections defined in eq. (2.27) are known to be useful for the extraction of the gluon fragmentation function through eq. (2.69). They can be extracted from the data, either by fitting the angular dependence for each x interval [66], or by weighting the double-differential cross section with respect to x and $\cos\theta$ with the appropriate weight to project onto the $(1+\cos^2\theta)$ component (transverse) or the $\sin^2\theta$ component (longitudinal):

$$\frac{d\sigma^{L,T}}{dx} = \int_{-v}^{+v} d\cos\theta\, W_{L,T}(\cos\theta, v)\, \frac{d^2\sigma}{dx\, d\cos\theta} \tag{5.8}$$

with [20]

$$W_L(\cos\theta, v) = \left[v^2\left(5+3v^2\right) - 5\cos^2\theta\left(3+v^2\right)\right]/4v^5 \tag{5.9}$$

and

$$W_T(\cos\theta, v) = \left[5\cos^2\theta\left(3-v^2\right) - v^2\left(5-3v^2\right)\right]/2v^5 \tag{5.10}$$

being the longitudinal and transverse projectors, respectively, and v defining the detector acceptance, which is considered to be constant in the range $|\cos\theta| < v = 0.94$.

The event and track selection are the same as described in section 5.1 except that the requirement on the sphericity axis is removed for the measurement of the longitudinal and transverse distributions, because it would introduce an effective strong $\cos\theta$ dependence in the track selection efficiency. Due to larger statistical errors in the measurement of the longitudinal distribution, the binning was changed with respect to the other measured distributions.

The selected tracks are then used to construct the inclusive transverse and longitudinal distributions according to

$$\frac{1}{\sigma_{\text{tot}}}\frac{d\sigma^{L,T}}{dx} = \left(\frac{1}{N_{\text{events}}}\sum_{\text{tracks}} W_{L,T}(\cos\theta, v)\right) \cdot \frac{1}{\sigma_{\text{tot}}}\int_{-v}^{v} d\cos\theta \frac{d^2\sigma}{dx\, d\cos\theta} \tag{5.11}$$

where the integral represents the cross section in a certain x bin integrated over the angular acceptance. The weights from eqs. (5.9) and (5.10) give the fraction of this total integral that is in the longitudinal and transverse part, respectively. Equation (5.11) can be simplified taking into account eq. (2.27), which allows to write the integral as

$$\frac{1}{\sigma_{\text{tot}}}\int_{-v}^{v} d\cos\theta \frac{d^2\sigma}{dx\, d\cos\theta} = \frac{1}{\sigma_{\text{tot}}}\frac{d\sigma}{dx}\frac{3}{4}\left[v + \frac{v^3}{3} + \frac{d\sigma^L/dx}{d\sigma/dx}(v - v^3)\right], \tag{5.12}$$

which only depends on the acceptance cut and the ratio of the longitudinal and total scaled energy distributions for the corresponding bin.

Equation (5.12) depends on the histogram bin since the ratio of the longitudinal and total cross section depends on it. However the ratio of the distributions changes by only 1.5% across the range in x measured. Therefore, it was assumed that this dependence would be taken into account in the correction factors and eq. (5.11) was approximated by

$$\frac{1}{\sigma_{\text{tot}}}\frac{d\sigma^{L,T}}{dx} = \left(\frac{1}{N_{\text{events}}}\sum_{\text{tracks}} W_{L,T}(\cos\theta, v)\right) \cdot \frac{1}{\sigma_{\text{tot}}}\frac{d\sigma}{dx} \cdot \mathcal{N}(v) \tag{5.13}$$

with

$$\mathcal{N}(v) \equiv \frac{3}{4}\left[v + \frac{v^3}{3} + \left\langle\frac{d\sigma^L/dx}{d\sigma/dx}\right\rangle(v - v^3)\right]. \tag{5.14}$$

which, for $v = 0.94$ is $\mathcal{N}(v) \sim 0.915$ with small variations with the value of $\left\langle\frac{d\sigma^L/dx}{d\sigma/dx}\right\rangle$. This value is not known before the measurement is made. So, it is taken as an approximation from the Monte Carlo and, after a first measurement is performed, it is recomputed and the measurement is made again with the new value.

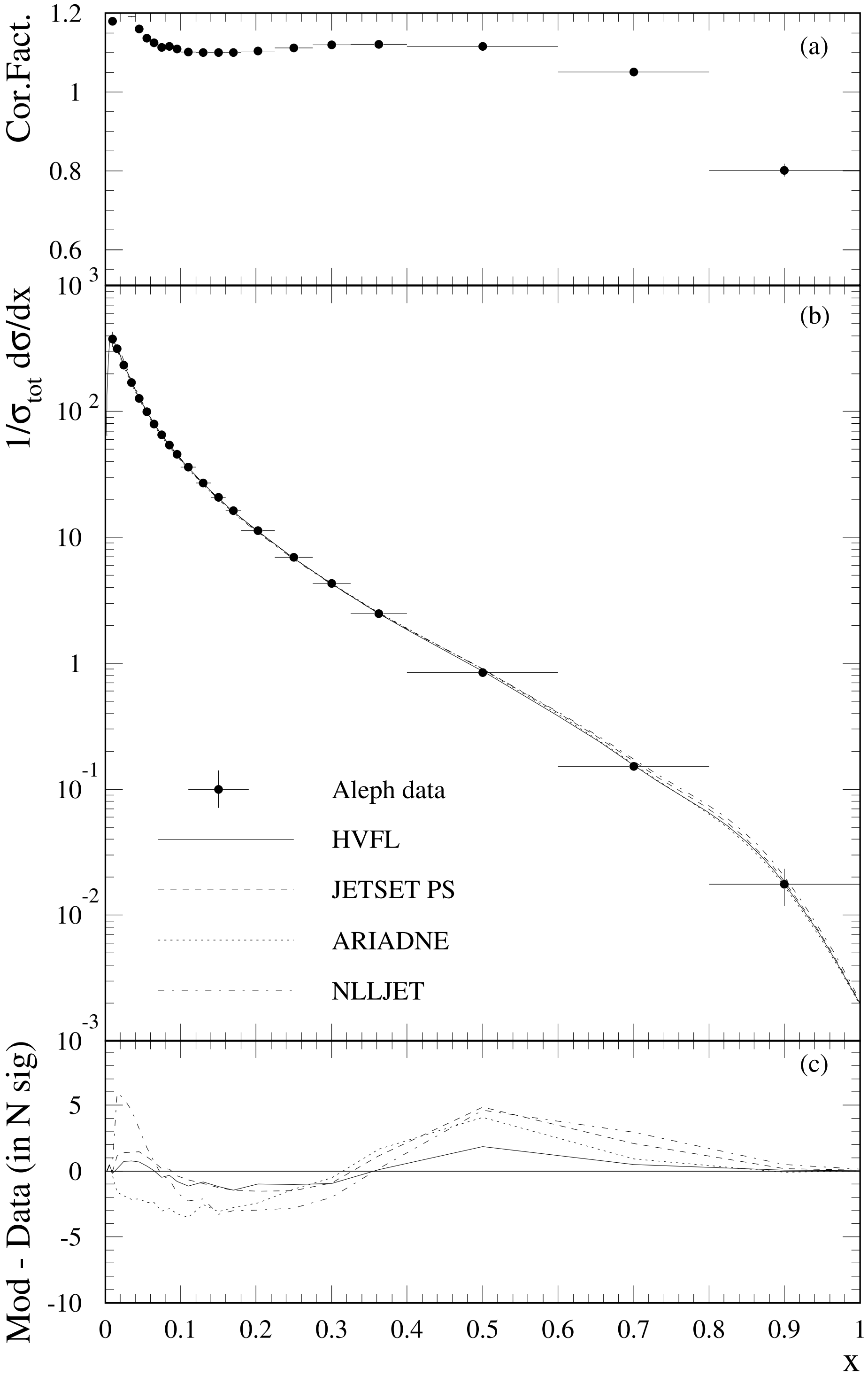

Figure 5.10: Correction factors applied to the transverse scaled energy distribution(a), corrected distribution and comparison with different Monte Carlo models (b), and deviation of the models from the corrected data measured in number of standard deviations, where the error includes statistical and systematical sources (c).

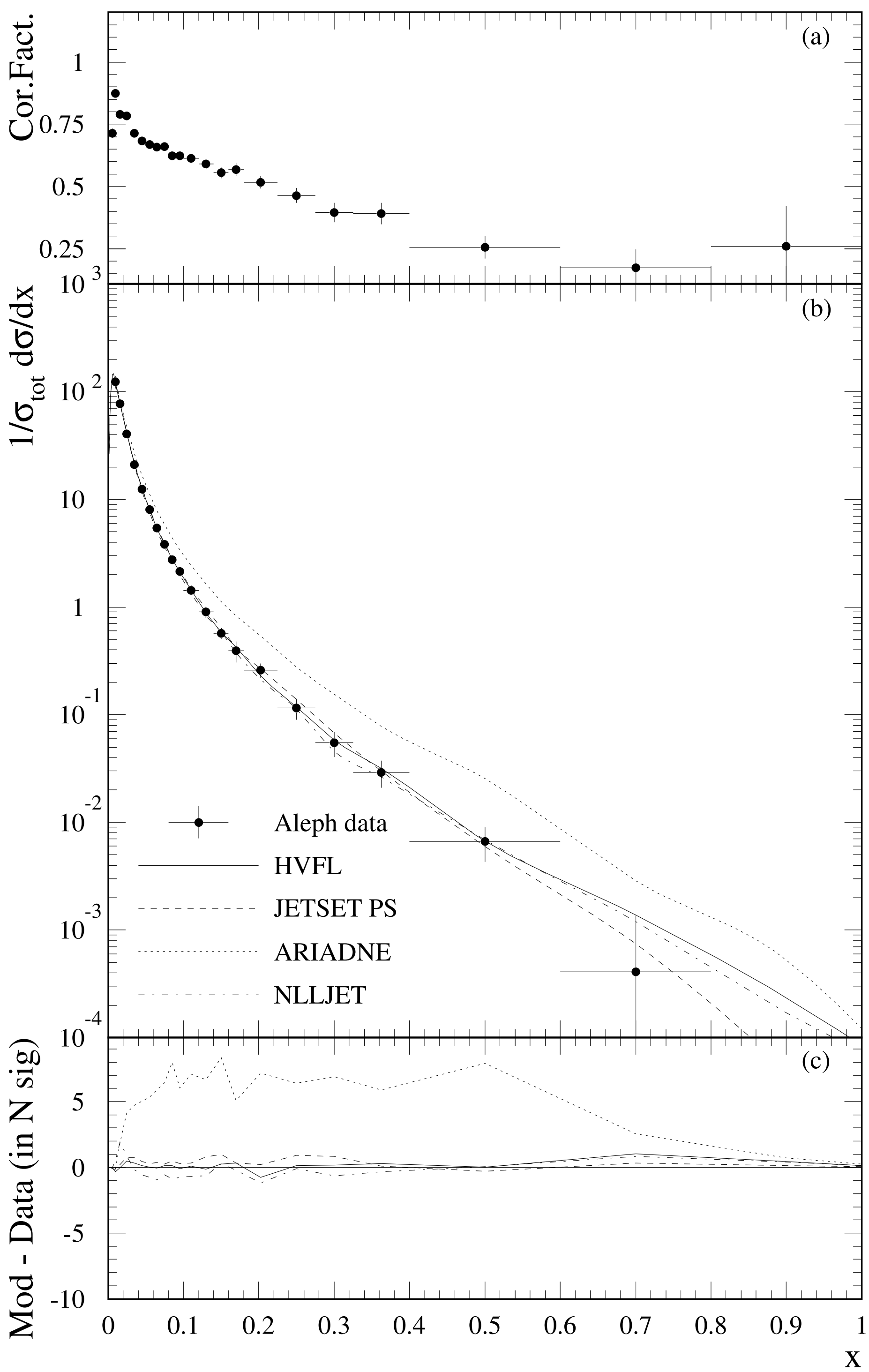

Figure 5.11: Correction factors applied to the longitudinal scaled energy distribution(a), corrected distribution and comparison with different Monte Carlo models (b), and deviation of the models from the corrected data measured in number of standard deviations, where the error includes statistical and systematical sources (c).

The correction procedure is performed bin by bin in the way described in section 5.2. Figures 5.10 and 5.11 show the correction factors and the comparison with different Monte Carlo models for the transverse and longitudinal scaled energy distribution, respectively. The only significant discrepancy is between ARIADNE and the corrected longitudinal distribution. While the correction factors for the transverse scaled energy distribution (fig. 5.10(a)) are rather similar to the corresponding ones for the total distributions (fig. 5.2(a)), the ones for the longitudinal distribution (fig. 5.11(a)) deserve more explanation.

Figure 5.12(a) shows the track selection efficiency for tracks inside the acceptance of $v = 0.94$. The hypothesis that this efficiency is constant over all the angles is not true and this causes these correction factors, especially for the longitudinal distribution, to be large. To confirm this hypothesis, studies with a toy Monte Carlo, parametrizing the angular track selection efficiency to the sum of a cubic polynomial and a hyperbolic tangent as a function of θ were done. This parametrization is displayed by a continuous line in figure 5.12(a). The correction factors obtained with this toy Monte Carlo follow the qualitative behaviour of the ones shown in figure 5.11(a). Thus, correcting the angular distribution before projecting the double differential cross section of x and $\cos\theta$ into the longitudinal and

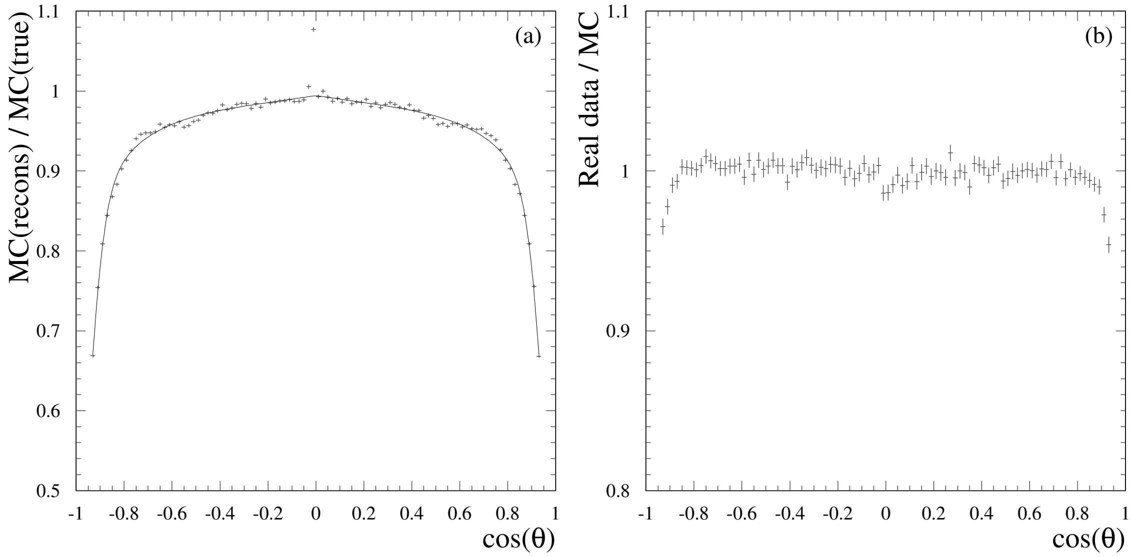

Figure 5.12: Reconstruction efficiency of charged tracks as a function of $\cos\theta$ according to the Monte Carlo simulation (a), and ratio of the angular distributions between Monte Carlo simulated data and real data (b).

transverse distributions would avoid the large correction factors of the longitudinal cross section. However, the result would be the same that including this effect in the bin to bin corrections.

Figure 5.12(b) shows the ratio of the angular distributions from real and simulated data. The differences are below 1% in almost the whole angular range, except for $|\cos\theta| > 0.9$. Since HVFL is expected to simulate the underlying angular distribution correctly, the differences are assigned to deficiencies of the simulation of the track efficiency at low angles. To take this into account, the analysis was repeated with $v = 0.9$ as acceptance cut. The differences between the longitudinal and transverse distributions obtained and the nominal distributions were taken into account in the systematic error which, otherwise, was computed following the same procedure explained in section 5.2. The extra systematic error is found to be essentially equivalent to assuming a 10% relative uncertainty in the track inefficiency at low angles.

The cross sections and the detailed error contributions for the transverse and longitudinal scaled energy distributions are given in tables C.6 and C.7 in appendix C. The bin-to-bin systematic errors dominate over the statistical error, especially in the longitudinal distribution, where the main contribution comes from the differences in the Monte Carlo models due to the disagreement between ARIADNE and the real data. The 1% normalization error is the dominant uncertainty for the transverse distribution.

5.6 Correlations between distributions

Apart from the statistical and systematic errors coming from the selection cuts or from the Monte Carlo model used in the detector correction, there exist correlated errors between the bins of all the measured distributions. One affects all the bins of all the measured distributions and it comes from systematic uncertainties in the normalization of the distributions. The other comes from the fact that some tracks enter in more than one distribution.

5.6.1 Normalization errors

The scaled energy distributions are normalized such that the integral of them is the mean number of charged tracks per event. Thus, any uncertainty in the charged multiplicity would affect all the bins of all the distributions. A study of the charged multiplicity of hadronic events has already been performed by ALEPH in ref. [67]. The error in the total charged multiplicity is about 1% and is mainly coming from the uncertainty in the multiplicity of tracks with transverse momentum below 0.2 GeV/c and from the uncertainty in the number of tracks from photon conversions accepted.

The uncertainty of the second kind is taken as correlated for all the bins of all the distributions. Conservatively, when the fit is performed, a 1% error has been added in quadrature to all the elements of the covariance matrix formed from all the distributions.

5.6.2 Correlations due to common tracks

Since all the tracks that enter in one bin of one of the tagged distributions enter also in the analogous bin of the distribution corresponding to all flavours, there is a statistical correlation between these bins. The cuts used for the flavour enriched distributions have been chosen to be exclusive and the binning is the same in all the distributions. This makes these correlations not to be present between analogous bins of different tagged distributions.

Supposing the number of tracks entering bin i in the inclusive distribution is $n_i^{\rm tot}$ and that the number of tracks in a given flavour tagged distribution for the same bin is $n_i^{\rm tag}$, being $n_i^{\rm tag} < n_i^{\rm tot}$, the correlation between the two bins of the distributions is given by

$$\rho_i^{\rm tot,tag} = \frac{n_i^{\rm tag}}{\sqrt{n_i^{\rm tag}}\sqrt{n_i^{\rm tot}}} = \sqrt{\frac{n_i^{\rm tag}}{n_i^{\rm tot}}}. \tag{5.15}$$

Therefore,

$$\sigma_i^{\rm tot,tag} = \sqrt{\frac{n_i^{\rm tag}}{n_i^{\rm tot}}}\sigma_i^{\rm tot,stat}\sigma_i^{\rm tag,stat} \tag{5.16}$$

Experiment	Normalization error
Tasso (22 GeV)	2.3%
TPC/2γ (29 GeV)	3.2%
Mark II (29 GeV)	1.5%
Tasso (35 GeV)	1.0%
Cello (35 GeV)	2.9%
Tasso (44 GeV)	1.5%
Amy (55 GeV)	0.4%
Delphi (91.2 GeV)	3.0%
Aleph (91.2 GeV)	1.0%

Table 5.2: Normalization errors used in the inclusive distributions for all the experiments used in the analysis. The errors on TPC/2γ, DELPHI and ALEPH are from the published papers. The rest are estimated as explained in the text.

was added in quadrature to the corresponding element of the covariance matrix formed with all the distributions when the data is used in the scaling violation fit that will be described in section 6.6.

5.7 Low energy data

The analysis of scaling violations needs the inclusive distributions for more than one energy to perform the evolution and have sensitivity to the strong coupling constant. Thus, in addition to the ALEPH data, inclusive charged particle spectra from TASSO [68] at $\sqrt{s}$ = 22, 35 and 45 GeV, MARK II [69] and TPC/2γ [70] at $\sqrt{s}$ = 29 GeV, CELLO [71] at $\sqrt{s}$ = 35 GeV, AMY [72] at $\sqrt{s}$ = 55 GeV and DELPHI [73] at $\sqrt{s}$ = 91.2 GeV have been used. Lower-energy data have been discarded because of the larger size of power-law corrections. In all those measurements, x was defined as $x = 2p/\sqrt{s}$. The difference with the ALEPH definition, $x = 2E/\sqrt{s}$, leads to negligible power-law corrections in the range $0.1 < x < 0.8$, used for the fit in section 6.6.

Special treatment of the errors was done in the cases where normalization errors were not specified. In some cases, statistical and systematic errors were not separated. The principle to estimate the normalization error was to take the minimum percentual systematic error as normalization error. To perform this, first the statistical errors were computed from the published number of events used in the measurement. This error was subtracted in quadrature from all the bins to compute the systematic error. The minimum percentage of computed systematic error was taken as percentual normalization error for all the bins. Table 5.2 shows the normalization errors for all the experiments used in the analysis.

Chapter 6

Scaling violations analysis and results

In section 2.5 a description on how to extract the information on α_s from the study of scaling violations in e^+e^- was presented.

However, some practical problems still arise before the measurement can be performed. Perturbative QCD does not predict the form of the fragmentation functions or the functional form of the power-law corrections. The assumptions made in these two aspects of the analysis are described in sections 6.3 and 6.4, respectively. The arguments to choose the parametrization scale are presented in 6.5.

But, before a fit to the data can give a reliable result for the strong coupling constant, still some more practical problems have to be solved. The coupled system of integro-differential evolution equations and the relations between the fragmentation functions and the cross sections are not at all trivially solvable equations. The methods to handle these numerical problems are described in sections 6.1 and 6.2.

Finally, the measurement, the systematic uncertainties and the checks done of the result are presented in sections 6.6, 6.7 and 6.8.

6.1 Evaluation of the convolution integrals

The equations relating the fragmentation functions to the measured cross-sections (section 2.2.1) and the evolution equations themselves (section 2.3) contain multiple convolution integrals of the type

$$\int_x^1 dz\, P(z)Q(x/z). \tag{6.1}$$

As the functions P and Q are rather complicated expressions of their argument, a fast algorithm to perform those integrals, which avoids a lot of slow numerical integrations, has to operate on tabulated function values. Thus, a uniform coverage in x and z, based on n subdivisions of the interval [0,1] would require to tabulate $P(z)$ on n, and $Q(x/z)$ on n^2 grid points, which already for a moderately small coordinate spacing results in huge memory requirements.

This can be avoided going to another set of variables [74]. Since the evolution of the fragmentation functions at a fractional momentum x_0 only depends on the values of the fragmentation and splitting functions at $x > x_0$, the analysis can be restricted also to a finite region in $\ln x$. It is therefore possible to substitute x and z by $t = \ln(z)$ and $u = \ln(x)$. In these variables eq. (6.1) becomes

$$\int_x^1 dz\, P(z)Q(x/z) = \int_u^0 dt\, \widetilde{P}(t)\widetilde{Q}(u-t) \tag{6.2}$$

with

$$\widetilde{P}(t) = e^t P\left(e^t\right) \quad \text{and} \quad \widetilde{Q}(u-t) = Q\left(e^{u-t}\right). \tag{6.3}$$

Choosing an equidistant grid in the new variables allows to evaluate the convolution integrals based on the same number of tabulated points for both $\widetilde{P}$ and $\widetilde{Q}$. Indexing the grid points from 1 to n, the convolution integral (6.2) can be approximated by the sum

$$\int_x^1 dz\, P(z)Q(x/z) \approx \Delta \cdot \sum_{i=k}^{n} \widetilde{P}_i \cdot \widetilde{Q}_{n-i} \tag{6.4}$$

where k is the index of the first $\widetilde{P}_i$ such that $t > u$ and Δ is the grid spacing in the transformed variables. The original convolution integral has been turned into a scalar product between two partial arrays of tabulated function values.

An algorithmically simple way to do the convolution integrals is only one aspect. In addition high numerical accuracy is required. The simple unweighted sum (6.4) evaluates the convolution integral with a residual error $\mathcal{O}(\Delta)$. This can be improved to $\mathcal{O}(\Delta^4)$ with only minimal additional computing costs by using the alternative extended Simpson's rule [75], where it is improved by adding a correction term which only depends on the function values at the first and last four evaluation points. The alternative extended Simpson's rule requires at least $N = 8$ knots where the integrand is evaluated. The cases $N < 8$ have to be dealt with individually.

A collection of integration rules for arbitrary $N > 1$ is given below. Information about how they are derived can be found in [75]. Let

$$\int_a^b dx\, f(x) = I \tag{6.5}$$

be the integral to be evaluated. Estimates for I shall be based on N evaluations $y_k = f(x_k)$, $k = 1, \ldots, N$, of the integrand on an equidistant grid with grid spacing Δ. If both endpoints are included, $x_1 = a$, $\Delta = (b - a)/(N - 1)$ and $x_N = b$. A complete set of closed quadrature formulas I_N is given by:

$$\begin{aligned}
I_2 &= \frac{\Delta}{2}(y_1 + y_2) && (6.6)\\
I_3 &= \frac{\Delta}{3}(y_1 + 4y_2 + y_3) && (6.7)\\
I_4 &= \frac{3}{8}\Delta(y_1 + 3y_2 + 3y_3 + y_4) && (6.8)\\
I_5 &= \frac{\Delta}{3}(y_1 + 4y_2 + 2y_3 + 4y_5 + y_5) && (6.9)\\
I_6 &= \frac{\Delta}{48}(17y_1 + 59y_2 + 44y_3 + 44y_4 + 59y_5 + 17y_6) && (6.10)\\
I_7 &= \frac{\Delta}{3}(y_1 + 4y_2 + 2y_3 + 4y_4 + 2y_5 + 4y_6 + y_7) && (6.11)\\
I_N &= \Delta\sum_{k=1}^{N} y_k - \frac{\Delta}{48}(31y_1 - 11y_2 + 5y_3 \\
&\quad - y_4 - y_{N-3} + 5y_{N-2} - 11y_{N-1} + 31y_N) \quad N \geq 8. && (6.12)
\end{aligned}$$

For functions which are difficult to evaluate at $x = b$, a modified set of open quadrature formulas I_N^+ can be derived. Here the information from the given grid points is extrapolated into the region between x_N and b. With $x_1 = a$, $\Delta = (b - a)/N$ and $x_N = b - \Delta$, the following expressions, which are of the same accuracy as the closed formulas given above are obtained:

$$I_1^+ = I_1 + \Delta\, y_1 \tag{6.13}$$

$$I_2^+ = I_2 + \frac{\Delta}{2}(3y_2 - y_1) \tag{6.14}$$

$$I_3^+ = I_3 + \frac{\Delta}{12}(23y_3 - 16y_2 + 5y_1) \tag{6.15}$$

$$I_N^+ = I_N + \frac{\Delta}{24}(55y_N - 59y_{N-1} + 37y_{N-2} - 9y_{N-3}) \quad N \geq 4 \tag{6.16}$$

where $\Delta = (b-a)/N$ is to be used everywhere.

6.2 Methods to solve the evolution equations

Looking at the non trivial structure of the evolution eqs. (2.46), it can be deduced that is almost unavoidable to use some numerical method to solve them. The standard method used in the analysis is the Runge-Kutta method. However, in some cases, a different approach can be useful. The moment analysis, apart from being an elegant method, allows to solve the equations analytically, at least, restricted to first order in α_s. This is no longer true when $\mathcal{O}(\alpha_s^2)$ corrections are introduced. Therefore, this method is only used in the study of Monte Carlo models to try to have an insight in the parametrization of the non-perturbative terms.

6.2.1 Runge-Kutta method

The general problem of solving a system of ordinary differential equations of any order can be reduced to solve a coupled system of N first-order ordinary differential equations like

$$\frac{dy_i(x)}{dx} = f_i(x, y_1, \ldots, y_N), \quad i = 1, \ldots, N \quad \longrightarrow \quad \frac{d\vec{y}(x)}{dx} = \vec{f}(x; \vec{y}). \tag{6.17}$$

Knowing the solution at a point x_n, a solution can be found at the point $x_{n+1} \equiv x_n + h$ with

$$\vec{y}_{n+1} = \vec{y}_n + h \cdot \vec{f}(x_n, \vec{y}(x_n)) + \mathcal{O}(h^2) \tag{6.18}$$

However, the method above is unstable and not accurate enough. Instead, the fourth-order Runge-Kutta method [75], which is more robust and precise, can be used. For each step in the solution, the following sequence of evaluations must be made for each of the f_i:

$$k_1 = h\, f(x_n, y_n)$$

$$
\begin{aligned}
k_2 &= h\, f(x_n + \frac{h}{2}, y_n + \frac{k_1}{2}) \\
k_3 &= h\, f(x_n + \frac{h}{2}, y_n + \frac{k_2}{2}) \\
k_4 &= h\, f(x_n + h, y_n + k_3) \\
y_{n+1} &= y_n + \frac{k_1}{6} + \frac{k_2}{3} + \frac{k_3}{3} + \frac{k_4}{6} + \mathcal{O}(h^5)
\end{aligned} \tag{6.19}
$$

where f stands for any of the f_i. It is easy to transport the method described in eqs. (6.19) to the evolution eqs. (2.46), where the right-hand f_i of (6.19) are the convolution integrals, h is the evolution variable, $\ln s$, and the y_i are each of the values of the pretabulated fragmentation functions. The value of h was chosen to be the difference between logarithms of the centre-of-mass energy of two consecutive distributions.

6.2.2 Moments method

An alternative method to solve the evolution equations is to convert them in simple differential equations. The evolution equations for the singlet (2.50) and non-singlet (2.49) parts, contain convolution integrals that, forgetting the energy dependence, are of the form

$$\int_x^1 dz\, P(z)\, A\left(\frac{x}{z}\right). \tag{6.20}$$

Taking into account that x and z take values between 0 and 1, this can be written in the form

$$\int_0^1 dy \int_0^1 dz\, \delta(y - \frac{x}{z})\, P(z)\, A(y) \tag{6.21}$$

where the lower limit in the integral over the z variable can be moved from x to 0 because the δ function ensures that the integrand is zero over the added interval between 0 and x. Multiplying eq. (6.21) by a power of x and integrating over the whole interval, gives

$$\int_0^1 dx\, x^n \int_0^1 dy \int_0^1 dz\, z\, \delta(x - yz)\, P(z)\, A(y) = \int_0^1 dy\, y^n A(y) \cdot \int_0^1 dz\, z^{n+1} P(z). \tag{6.22}$$

This property can be used to simplify the integro-differential evolution equations in such a way that they become simple differential equations when they are expressed in form of the moments of the fragmentation functions. The formalism is described in detail in [76]. Here it is described at leading order, since this formalism is only used in the leading order study of the scaling violations with the different Monte Carlos with the purpose to have an insight of the parametrization of the non-perturbative power-law corrections (section 6.4).

The moments of the cross-sections are defined in the following way:

$$M_n = \int_0^1 dx\, x^{n+1} \frac{d\sigma}{dx}. \tag{6.23}$$

Then, taking into account that the singlet and non-singlet parts of the fragmentation functions have been defined weighted with x according to eq. (2.48), the n-order moment for the singlet, non-singlet and energy-weighted gluon fragmentation function has to be defined as

$$A_n = \int_0^1 dx\, x^n A(x,s) \qquad A = N, S, G. \tag{6.24}$$

Up to leading order, the running coupling constant is given by

$$\alpha_s(s) = \frac{1}{b_0\, t} \tag{6.25}$$

where b_0 is given in (2.26) and t is defined as

$$t = \ln\left(\frac{s}{\Lambda^2}\right) \tag{6.26}$$

being Λ the leading order effective QCD scale. Equation (6.25) is just the approximation up to first order of the running coupling constant described in section 2.1.3. With these definitions, and the property of eq. (6.22), it is easy to show that the evolution equations simplify to

$$\begin{aligned} t\frac{d}{dt}\begin{pmatrix} S_n \\ G_n \end{pmatrix} &= \begin{pmatrix} a^n_{\mathrm{QQ}} a^n_{\mathrm{GQ}} \\ a^n_{\mathrm{QG}} a^n_{\mathrm{GG}} \end{pmatrix} \begin{pmatrix} S_n \\ G_n \end{pmatrix} \\ t\frac{d}{dt} N_n &= a^n_{\mathrm{QQ}} N_n. \end{aligned} \tag{6.27}$$

with the coefficients a^n_{xx} given by

$$\begin{aligned} b_0 a^n_{\mathrm{QQ}} &= -\frac{1}{2} + \frac{1}{(n+2)(n+3)} - 2\sum_{j=2}^{n+2}\frac{1}{j} \\ b_0 a^n_{\mathrm{GG}} &= 2X\left[-\frac{1}{12} + \frac{1}{(n+1)(n+2)}\right. \end{aligned} \tag{6.28}$$

$$+\frac{1}{(n+3)(n+4)} - \sum_{j=2}^{n+2} \frac{1}{j}\Bigg] - \frac{2}{3}Z \tag{6.29}$$

$$b_0 a^n_{\mathrm{GQ}} = \frac{n^2+5n+8}{(n+1)(n+2)(n+3)} \tag{6.30}$$

$$b_0 a^n_{\mathrm{QG}} = 2Z\,\frac{n^2+5n+8}{(n+2)(n+3)(n+4)}, \tag{6.31}$$

where X, Z, and b_0 are defined in eqs. (2.12) and (2.26). The solution of the non-singlet part is rather trivial and gives

$$N_n(s) = N_n(s_0)\left(\frac{\ln(s/\Lambda^2)}{\ln(s_0/\Lambda^2)}\right)^{a^n_{\mathrm{QQ}}}. \tag{6.32}$$

The solution for the coupled system needs a little bit more algebra and can be expressed as

$$\begin{pmatrix} S(t) \\ G(t) \end{pmatrix} = \alpha_1 \vec{e}_1 \left(\frac{t}{t_0}\right)^{\lambda_1} + \alpha_2 \vec{e}_2 \left(\frac{t}{t_0}\right)^{\lambda_2} \tag{6.33}$$

where $\lambda_{1,2}$ are the eigenvalues of the coefficient matrix in eq. (6.27) and $\vec{e}_{1,2}$ the corresponding eigenvectors. The parameters $\alpha_{1,2}$ are determined through the initial conditions for $t = t_0$ at the initial centre-of-mass energy $\sqrt{s_0}$.

6.3 Parametrization of the fragmentation functions

The scheme presented in figure 2.2 assumes that the fragmentation functions are specified at one particular energy scale. With enough amount of data, it would be possible to perform a moment analysis, in a similar way as the one described in section 6.2.2, where this parametrization would not be necessary. But, the coarse binning of the data due to statistical limitations does not allow to fix the initial conditions truly unambiguously. Some assumptions about the shape of the fragmentation functions must be done, the least restrictive ones being the requirements of positiveness and smoothness. The most convenient approach is to use a phenomenological parametrization, where the shape is described by a small number of free parameters.

Perturbative QCD, in the framework of the Modified Leading-Log Approximation (MLLA) [77], supplemented by the Local Parton-Hadron Duality (LPHD) hypothesis [78], predicts that the momentum spectrum of final state particles should exhibit an approximately gaussian peak in $\ln x$ [79]. From this, it can be inferred a functional form for the scaled energy distributions like

$$\frac{d\sigma}{d\ln x} \sim \exp\left(-c(d-\ln x)^2\right) \quad \Leftrightarrow \quad \frac{d\sigma}{dx} \sim \frac{1}{x}\exp\left(-c\ln^2 x\right) x^{2cd}. \tag{6.34}$$

Combined with the expectation that the momentum spectrum falls off with some power of $1-x$ for $x \to 1$ [11, 17], finally yields the ansatz

$$D(x) = N(1-x)^a x^{b-1} \exp\left(-c\ln^2 x\right), \tag{6.35}$$

where N, a normalization constant, and a, b and c are free parameters which have to be determined from the data. With the possible exception of c, the parameters are expected to be different for light quarks, c quarks, b quarks and gluons. The parameter c is in principle predicted by the MLLA and, in leading order, should also be flavour independent. In total, thirteen parameters are used to describe the fragmentation functions at one energy: the c parameter, which is taken equal for all flavours and the gluon, and the N_i, a_i and b_i for the light, c, and b quarks and the gluon.

In order to avoid correlations between the normalization and the rest of parameters, the final parametrization function chosen for the analysis is given by

$$xD_i(x,s_0) = N_i \, \frac{(1-x)^{a_i} x^{b_i} \exp\left(-c\ln^2 x\right)}{\int_{0.1}^{0.8} dx\,(1-x)^{a_i} x^{b_i} \exp\left(-c\ln^2 x\right)}, \tag{6.36}$$

where i stands for uds, c, b, and g (gluons), and the dependence on s_0 comes from the implicit dependence of the parameters (N_i, a_i, b_i and c) on this variable.

6.4 Parametrization of the non-perturbative terms

Another still undefined part of the analysis is the introduction of the non-perturbative contributions to the evolution. In sections 2.4 some sources of power-law corrections were presented. There are corrections that go as $1/\sqrt{s}$ and others that go as $1/s$. Although it is expected that the dominant one is coming from hadronization corrections (section 2.4.4), which go as $1/\sqrt{s}$, the actual form of the non-perturbative contributions to the evolution is not known.

Given sufficient data, it would also be possible to determine them from the data without strong external assumptions. Such an approach was followed in the analysis of the SLAC/BCDMS deep-inelastic scattering data [80]. There, the power-law corrections were known to behave like $1/Q^2$, with the available data covering the range $0.5\,\mathrm{GeV}^2 < Q^2 < 260\,\mathrm{GeV}^2$. In the study of scaling violations in fragmentation functions, the power-law corrections are expected to behave like $1/\sqrt{s}$, while a typical analysis covers data in the range from $22\,\mathrm{GeV} < \sqrt{s} < 91\,\mathrm{GeV}$. Thus the dynamical range to separate power-law corrections from the logarithmic scaling violations due to perturbative QCD is 125 times larger in deep-inelastic scattering experiments than it is in e^+e^--annihilation. This severely restricts the number of parameters describing non-perturbative effects that can be determined from the data to essentially only a single number.

A simple effective way of parametrizing the non-perturbative effects is by doing a change of variables and relate the perturbative variable x to the measured quantity x_e through $x = g(x_e)$. Imposing the condition of energy conservation before and after the transformation fixes the relation between the perturbative prediction $\sigma(x)$ and the observable cross section $\sigma_{NP}(x_e)$:

$$\int dx x \frac{d\sigma}{dx} = \int dg(x_e) g(x_e) \frac{d\sigma}{dx} = \int dx_e g(x_e) g'(x_e) \frac{d\sigma}{dx} = \int dx_e x_e \frac{d\sigma_{NP}}{dx_e} \tag{6.37}$$

From this, it can be deduced that

$$\frac{d\sigma_{NP}}{dx_e} = \frac{g(x_e)g'(x_e)}{x_e}\frac{d\sigma}{dx}. \tag{6.38}$$

The simplest ansatz for g is given by a rescaling of the type $x = x_e(1 + h_1/\sqrt{s})$ [20]. However, it was found that some other parametrizations could work better. A general ansatz for the non-perturbative effects is given by

$$x = g(x_e) = x_e + (h_0 + h_1\, x_e + h_2\, x_e^2 + \ldots)\left[\left(\sqrt{s}\right)^{-k} - \left(\sqrt{s_0}\right)^{-k}\right]. \tag{6.39}$$

Using only the parameter h_0 means that the perturbative prediction and the observable cross-sections are related by a shift of the spectra, using only h_1 corresponds to a rescaling of x. The energy-dependence of this transformation is given by the term in square brackets. This term is built such that the non-perturbative corrections are zero at the scale $\sqrt{s_0}$ where the fragmentation functions are parametrized, which takes into account the fact that the fragmentation functions themselves already parametrize all non-perturbative effects at a given scale. Perturbative QCD then predicts logarithmic scaling violations in the evolution of those fragmentation functions, and the above ansatz takes care of the power law corrections that come on top.

There are sources of power-law corrections in which $k = 1$ and another ones in which $k = 2$. Since the number of parameters allowed by the currently available experimental data is only one, some guidance about the appropriate choice has to be taken from Monte Carlo simulations of e^+e^- annihilation processes into hadrons. In addition to a discrimination between using h_0 and h_1 (shift versus rescaling) those models also allow to infer the power k to be used in eq. (6.39).

For this purpose a leading-order moment analysis as described in section 6.2.2 was performed on data generated with the JETSET, ARIADNE and HERWIG Monte Carlo models. Here even the higher moments of the fragmentation functions can be reliably determined, something which unfortunately is in practice impossible for the comparatively coarse-binned published experimental x-distributions. Moments can be viewed as a convenient means to describe the shape of the fragmentation functions without having to resort to an explicit parametrization. Low order moments probe mainly the low x part of the distribution, higher order moments progressively test large x region. The next sections describe this analysis and the parametrization of the non-perturbative terms used in the analysis of the real data.

6.4.1 Non-perturbative terms in the moments analysis

The missing ingredient to perform the moments analysis is the inclusion of the non-perturbative effects. This is easy for the two simple parametrizations discussed above. Defining

$$f(x) = \frac{d\sigma}{dx}(x) \tag{6.40}$$

$$a_1 = 1 + h_1 \left[\left(\sqrt{s}\right)^{-k} - \left(\sqrt{s_0}\right)^{-k} \right] \tag{6.41}$$

$$a_0 = h_0 \left[\left(\sqrt{s}\right)^{-k} - \left(\sqrt{s_0}\right)^{-k} \right], \tag{6.42}$$

the introduction of the rescaling in the moments becomes

$$M_n(\mathrm{NP}) = \int_0^1 dx_e\, x_e^{n+1}\, f_{\mathrm{NP}}(x_e) = \int_0^1 dx_e\, a_1^2\, x_e^{n+1}\, f(a_1 x_e)$$

$$= \int_0^{a_1} dy\, a_1^{-n} y^{n+1} f(y) = a_1^{-n} M_n \tag{6.43}$$

where the last step is done because the integral in the interval $(0, a_1)$ in y is the whole phase space as $(0, 1)$ is for the variable x_e.

In the case of the shift,

$$\begin{aligned} M_n(\mathrm{NP}) &= \int_0^1 dx_e\, x_e^{n+1} f_{\mathrm{NP}}(x_e) = \int_0^1 dx_e\, \frac{x_e + a_0}{x_e}\, x_e^{n+1} f(x_e + a_0) \\ &= \int_{a_0}^{a_0+1} dy\, y\, (y - a_0)^n f(y) = \sum_{k=0}^{n} \binom{n}{k} (-a_0)^{n-k} M_k \end{aligned} \tag{6.44}$$

where the last step is done again because the integral in the interval $(a_0, a_0 + 1)$ in y is the whole phase space as $(0, 1)$ is for the variable x_e.

Here M_n are the moments without power-law corrections and $M_n(\mathrm{NP})$ the moments including the non-perturbative effects.

6.4.2 Monte Carlo study

The energy evolution of the moments seen in the Monte Carlo and its comparison to the leading-order QCD prediction allow to infer the behaviour of the non-perturbative corrections [74]. A leading-order analysis is justified since the Monte Carlo models are based on a leading-log cascade and only partially incorporate next-to-leading logarithmic effects.

Monte Carlo data containing 1 million events were generated with the natural flavour mix for centre-of-mass energies of 22, 35, 44, 55 and 91 GeV for the JETSET PS, ARIADNE and HERWIG models. At 91 GeV, additional samples of 1 million events with primary c and b quarks were generated. From this, the moments for light, c and b quark fragmentation functions at an initial scale of 91 GeV were determined. The gluon fragmentation function, which in leading order does not contribute to the observable cross section but is needed in the evolution equations, was assumed to be equal to the c quark fragmentation function. The associated uncertainty was estimated by alternatively setting it equal to the b quark fragmentation function and taking the corresponding change in the evolution of the moments as a theoretical error.

For the determination of the parameters governing the power-law corrections, the QCD scale parameter Λ describing the logarithmic part of the scaling violations

JETSET 7.3 $\Lambda_{QCD} = 0.319\,\mathrm{GeV}$								
Ansatz		$\overline{\chi^2/n_{df}}$	Parameter Value h (GeV)					
h_0	$1/\sqrt{s}$	154	-0.78	$\pm$	0.15	$\pm$	0.15
h_1	$1/\sqrt{s}$	183	-2.3	$\pm$	1.40	$\pm$	0.41
h_0	$1/s$	356	$-15.$	$\pm$	1.7	$\pm$	2.8
h_1	$1/s$	411	$-45.$	$\pm$	28.	$\pm$	7.8
ARIADNE 4.02 $\Lambda_{QCD} = 0.225\,\mathrm{GeV}$							
Ansatz		$\overline{\chi^2/n_{df}}$	Parameter Value h (GeV)				
h_0	$1/\sqrt{s}$	46	-0.59	$\pm$	0.13	$\pm$	0.13
h_1	$1/\sqrt{s}$	56	-1.8	$\pm$	0.95	$\pm$	0.38
h_0	$1/s$	132	$-11.$	$\pm$	1.7	$\pm$	2.5
h_1	$1/s$	152	$-35.$	$\pm$	20.	$\pm$	7.4
HERWIG 5.6 $\Lambda_{QCD} = 0.152\,\mathrm{GeV}$							
Ansatz		$\overline{\chi^2/n_{df}}$	Parameter Value h (GeV)				
h_0	$1/\sqrt{s}$	13	-0.41	$\pm$	0.12	$\pm$	0.11
h_1	$1/\sqrt{s}$	15	-1.3	$\pm$	0.59	$\pm$	0.36
h_0	$1/s$	43	-8.5	$\pm$	2.3	$\pm$	2.3
h_1	$1/s$	48	$-25.$	$\pm$	13.	$\pm$	7.1

Table 6.1: Monte Carlo studies of non-perturbative corrections. See text for definition of errors.

was fixed to the input value used for the respective model. Different functional forms for the non-perturbative corrections were tried separately for the leading ten moments in single-parameter fits of h_0 and h_1 assuming the energy dependence to be $1/\sqrt{s}$ or $1/s$. The power law corrections were included in such a way that they vanish at $\sqrt{s} = 22\,\mathrm{GeV}$.

The results are summarized in table 6.1 and one example is displayed in figure 6.1. For each ansatz of the non-perturbative terms, the average chisquare per degree of freedom $\overline{\chi^2/n_{df}}$ is given together with the value obtained for the non-perturbative parameter h_i. The quoted number is the central value obtained over the first 10 moments, the first error is half-range of the values obtained, and the second one the half range found when varying the QCD scale, Λ, from one half to twice its nominal value. The statistical errors are completely negligible.

Although $\overline{\chi^2/n_{df}}$ is rather large, one has to keep in mind that the Monte Carlo

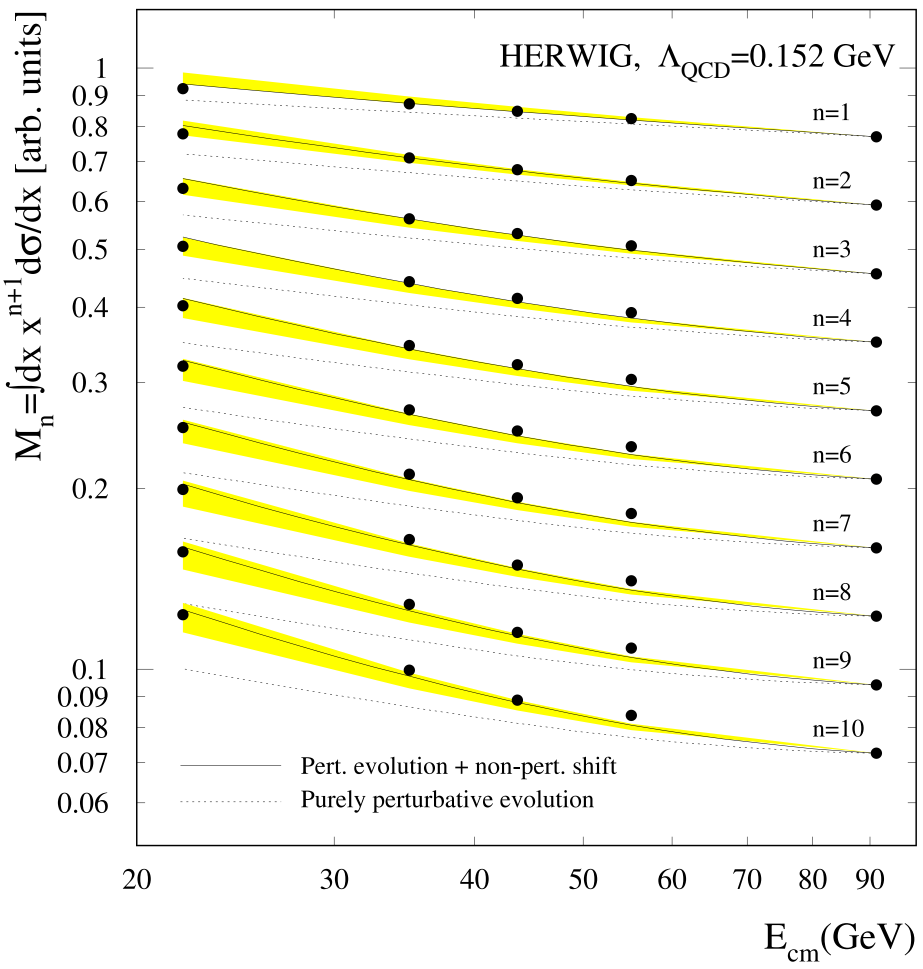

Figure 6.1: Energy evolution for the leading moments of the inclusive x distributions as predicted by the HERWIG model. The points are the actual moments, the curves are the results of the leading order QCD analysis. The dotted lines show the result of a purely perturbative evolution from 91 GeV to 22 GeV. The full lines are evolutions over the same range. The parameter h_0 is optimized separately for each moment. The shaded bands are obtained by varying a global parameter h_0 between the extreme values found in the individual fits.

statistics used in this study is roughly a hundred times of what is available in the data. Consequently even values $\chi^2/n_{df} \approx \mathcal{O}(100)$ correspond to a satisfactory description of the data. As it can be seen from figure 6.1, even despite the bad χ^2 the qualitative behaviour is well reproduced by the fits. Studying the χ^2 values given in table 6.1 shows that a power-law behaviour with $1/\sqrt{s}$ is clearly preferred over a $1/s$ dependence. Concerning the choice of h_0 versus h_1, the χ^2 values are less conclusive. However, from the spread of the results (first error in the table) it can be seen that h_0 is much more stable than h_1. This can be traced to the fact that the fitted value for h_1 becomes more and more negative for lower order moments, i.e. when putting more emphasis on the low-x region, suggesting a behaviour $h_1 \sim 1/x$ which is equivalent to parametrizing the non-perturbative terms by a shift h_0.

In conclusion, the Monte Carlo studies suggest a simple effective parametrization of the non-perturbative terms of the functional form

$$x = x_e + h_0 \left(\frac{1}{\sqrt{s}} - \frac{1}{\sqrt{s_0}} \right) \tag{6.45}$$

with a negative parameter h_0, and this is what is going to be used in the fit to the real data.

6.5 Choice of parametrization scale

With the values of h_0 obtained from the Monte Carlo study (table 6.1), typical shifts in x are of the order $\Delta x = \mathcal{O}(0.01)$. At high values of x, where the cross section goes to zero, such a shift is much smaller than the experimental resolution and thus has only very little impact. At small x it amounts to a non-negligible change of the cross-section for two reasons: the momentum measurement is much more precise and the cross section rises rapidly. The fact that a negative h_0 seems to be preferred and the functional form (6.45) suggests to use a parametrization scale $\sqrt{s_0}$ smaller or equal to the smallest scale used in a scaling violations analysis, such that the value x at which the perturbative cross section is evaluated in order to obtain the cross-section at the experimental value x_e is always larger than x_e. This assures that x never is needed at unphysical negative values. Unphysical values $x > 1$ may occur but, as explained above, this is much less severe and can easily be tolerated, thus permitting to have a really simple way of parametrizing non-perturbative effects. For the fit to be explained in the following section, $\sqrt{s_0} = 22\,\mathrm{GeV}$ is chosen.

6.6 Results of the fit

An overall fit of the QCD predictions to all ALEPH and low energy data between 22 GeV and 91.2 GeV presented in chapter 5 is done. Following the arguments given in section 6.5, the fragmentation functions for the different flavours are parametrized at 22 GeV according to eq. (6.36). The non-perturbative effects are parametrized by (6.45). In total, thirteen parameters are used to describe the fragmentation functions at one energy, the c parameter introduced in section 6.3, and the normalizations (N_i) and values of a_i and b_i for the light, c and b quarks and also for the gluon fragmentation function. The evolution to another energy requires two more parameters: α_s, which determines the perturbative evolution, and h_0, which parametrizes the non-perturbative effects in the evolution. Finally, the first order strong coupling constant, β_s, introduced in eq. (2.69) is also required. Altogether there are sixteen parameters, which are all fit simultaneously to the available data.

The flavour-tagged distributions serve mainly the purpose of fixing the parameters of the corresponding fragmentation functions. The gluon-tagged sample and the longitudinal and transverse distributions determine the leading-order coupling constant, β_s, and the parameters of the gluon distribution function. Then, from the low energy data and the inclusive data at 91 GeV the values of α_s and h_0 are obtained.

The fit range is chosen as $0.1 < x < 0.8$ for all data at all energies. Outside this range, systematic effects, especially at low $\sqrt{s}$, start to become important. However, for the longitudinal cross section (measured only at 91 GeV), the fit range is taken as $0.04 < x < 0.8$ to increase the statistical sensitivity.

The procedure follows the scheme of figure 2.2. First, the parametrization of the fragmentation functions for the three quark species and the gluon is used to tabulate the values of the function $xD_i(x, s_0)$ in a grid of equally spaced points in $\ln x$. The number of points was chosen to be 100 in the interval $[\ln 0.04, \ln 1]$. Tests were done to probe the sensitivity of the fit result to larger number of grid points, resulting in no change. The coefficient functions and the kernels are also tabulated in $\ln x$ using the same grid definitions that for the fragmentation functions.

Then, the coefficient functions are used at the parametrization energy to compute the measurable cross sections (horizontal arrows in figure 2.2). The convolution integrals involved in this procedure are computed as explained in section 6.1. A covariance matrix is constructed with the errors of the data and the correlation between the different bins, and the χ^2 is computed from the comparison of the data and the cross-sections computed from the convolution of the fragmentation

$\alpha_s(M_Z) = 0.1258 \pm 0.0053$ $h_0 = -0.14 \pm 0.10$ GeV				
	light (uds) quarks	c quarks	b quarks	gluons
N	0.372 ± 0.005	0.359 ± 0.006	0.295 ± 0.008	0.395 ± 0.020
a	1.69 ± 0.04	3.09 ± 0.16	3.29 ± 0.09	2.6 ± 0.8
b	-1.40 ± 0.06	-1.10 ± 0.09	-1.69 ± 0.07	-1.59 ± 0.29
c	0.252 ± 0.014			
β_s	0.199 ± 0.008			

Table 6.2: Results of the fit to all data. The errors include statistical and experimental systematic uncertainties, except for those related to flavour tagging. See text for definition of parameters.

functions and the coefficient functions.

The tabulated kernels and the fragmentation functions are used to compute the fragmentation functions at other energies (vertical arrows in figure 2.2). The solution of the evolution equations (2.46) is obtained using the Runge-Kutta technique described in section 6.2.1. Again convolution integrals are involved in this procedure that are solved in the way described in section 6.1. The fragmentation functions at the new energy are used, together with the coefficient functions, to compute the cross-sections at the new energy. The inclusion of the parametrized non-perturbative effects is done following the parametrization (6.45). The comparison with the measured data follows the same procedure that the one done for the initial parametrization scale.

The evolution of the fragmentation functions, the subsequent calculation of the predicted cross-section and the comparison of the prediction to the data is done for all the available distributions at different centre-of-mass energies. A total χ^2 results from all the procedure which is then minimized changing the sixteen parameters of the fit.

The results of the fit are shown in table 6.2. There are sizable correlations amongst most of the parameters, which may be as large as 90% between the parameters of the fragmentation functions. The parameter most strongly correlated with $\alpha_s(M_Z)$ is the one describing the energy evolution of the non-perturbative terms, h_0. Here the correlation is 36%. The value found for h_0 is compatible with zero, which

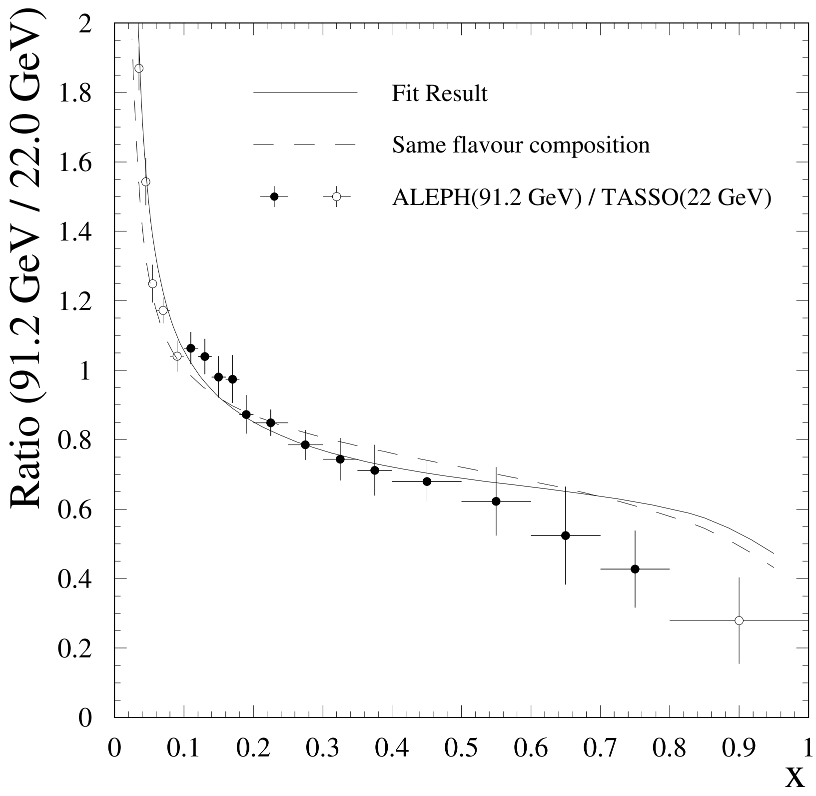

Figure 6.2: Ratio of inclusive cross sections at $\sqrt{s} = 91.2\,\mathrm{GeV}$ and $\sqrt{s} = 22\,\mathrm{GeV}$ compared to the QCD prediction. The full dots contributed in the global fit.

indicates that non-perturbative effects are small, within the parametrization given by eq. (6.45). The influence of h_0 in the uncertainty of α_s can be seen by fixing it at its central value. The error on α_s decreases to ± 0.0049. Thus, its contribution to the total error can be estimated to be ± 0.0020. Fixing all the parameters describing the shape of the fragmentation function and the non-perturbative corrections, the purely experimental error of $\alpha_s(M_{\mathrm{Z}})$ would be $\Delta\alpha_s = 0.0017$.

The value found for α_s agrees with previous ALEPH determinations [81] and c with the MLLA expectation [79]. Also β_s is consistent with typical values for a leading-order α_s measurement. Since β_s is allowed to vary, the information about the gluon fragmentation function obtained from the longitudinal cross section improves only marginally the direct measurement.

The size of the scaling violations can be seen in Figure 6.2, where the ratio of the inclusive cross sections measured by ALEPH at $\sqrt{s} = 91.2\,\mathrm{GeV}$ and TASSO at $\sqrt{s} = 22\,\mathrm{GeV}$ is plotted as a function of x. For comparison, also the expectation

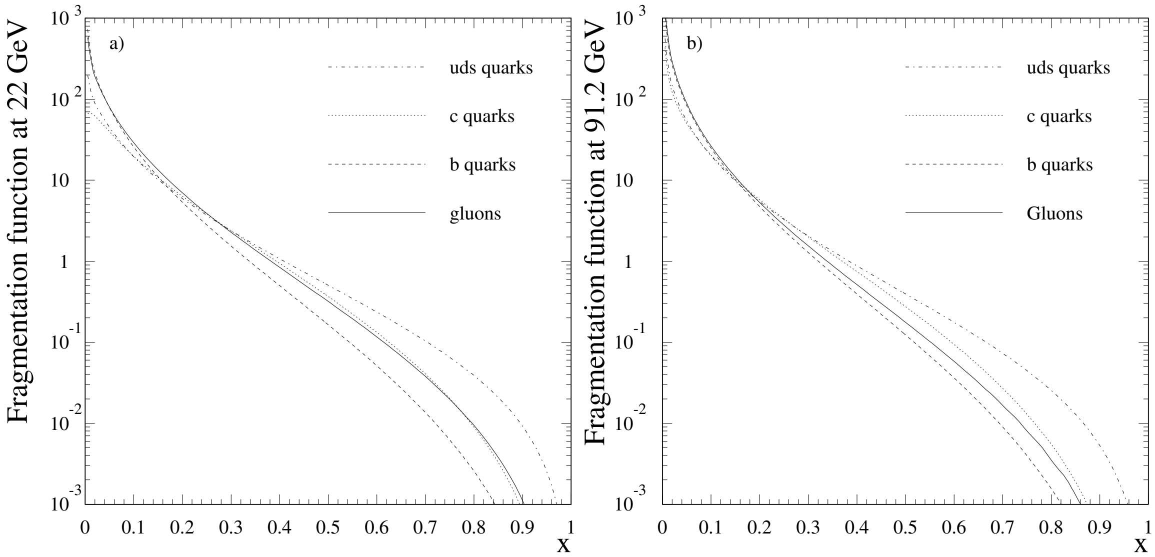

Figure 6.3: Fragmentation functions at (a) 22 GeV and (b) 91.2 GeV obtained from the fit. It can be observed the generally harder spectra of the functions at lower energy. The gluon fragmentation function becomes closer to the b fragmentation function as the energy increases.

for the case all the distributions would have the same flavour composition as at 91.2 GeV is given. The size of the scaling violations can also be seen by comparing directly the fragmentation functions obtained at the two energies (figure 6.3).

Figure 6.4 shows that the overall agreement between data and prediction is good and that the QCD evolution reproduces the observed scaling violations. All error bars include both statistical and experimental systematic uncertainties. This can be seen in better detail in figure 6.5 where the differences between the fitted and the measured values are plotted in number of standard deviations (statistical and systematic error of the measured distribution are included). Most of the distributions start to disagree with the fitted curves below $x = 0.1$, where the fit is not performed. This is due to inadequacies in the parametrization of the fragmentation function in this zone. The ALEPH data gives the impression of having a large contribution to the total χ^2 mainly coming from the low momentum region (below $x = 0.4$). This is not the case because all the data is correlated through the normalization error (section 5.6.1). When the correlated error is the dominant one (as it is the case in this momentum region for the ALEPH data), the overall contribution to the χ^2 is the same as the one coming from only one bin. Thus, although the differences are almost two standard deviations for all the bins in this

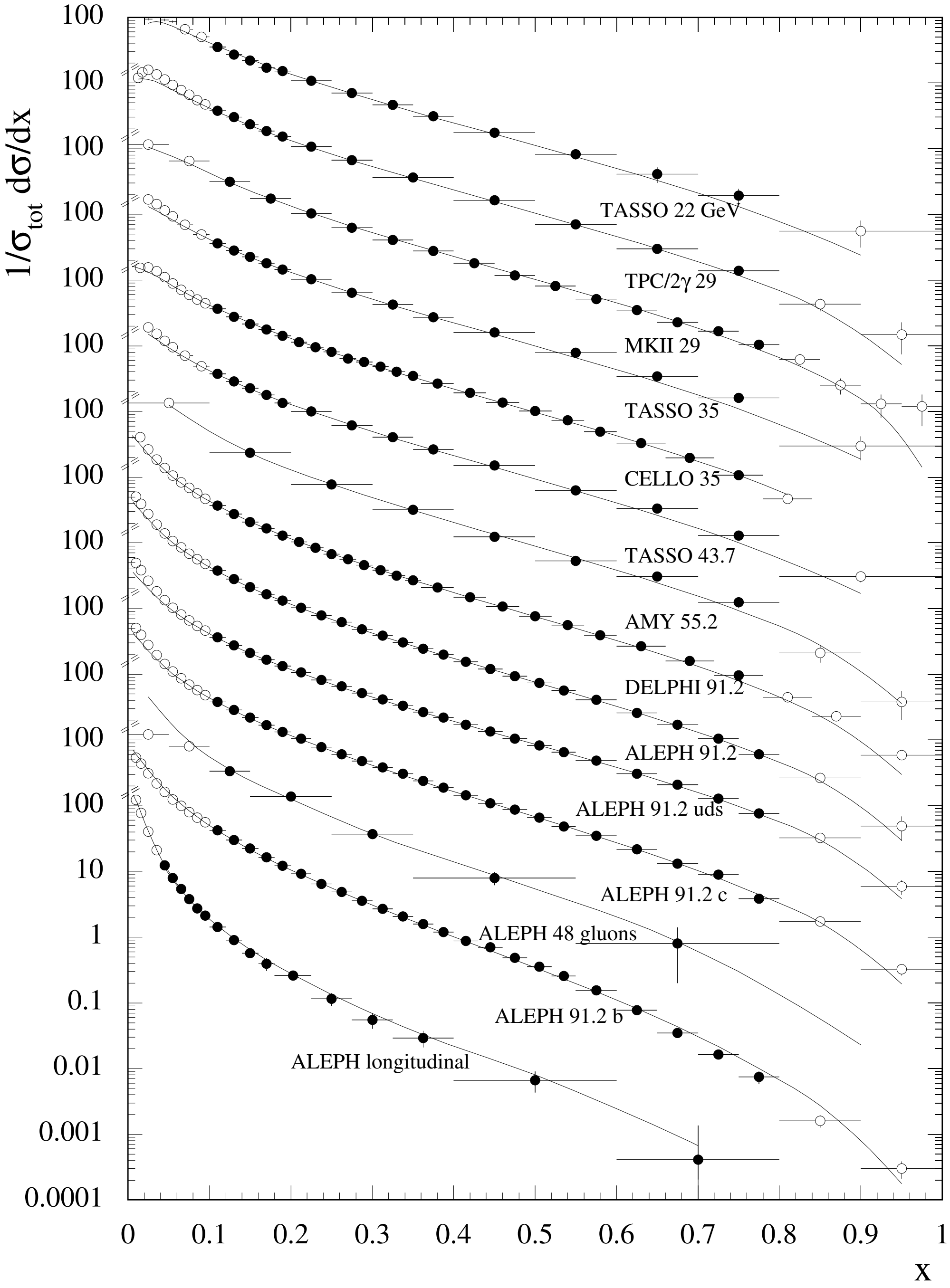

Figure 6.4: Scaled-energy distributions used in the QCD fit. Only the dark points enter the fit. Errors shown include statistical and systematic uncertainties. The lines represent the result of the fit.

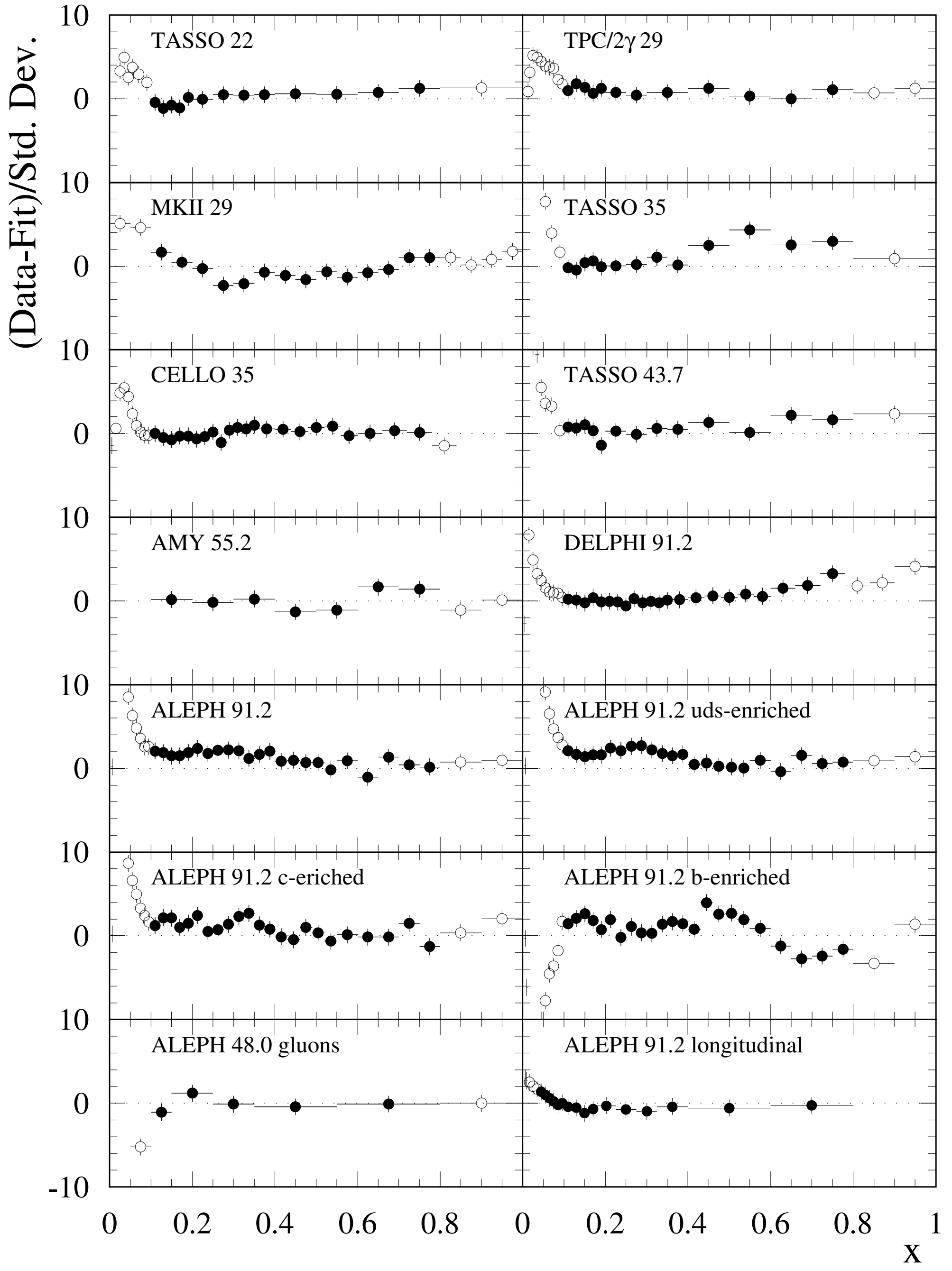

Figure 6.5: Differences between the fit result and the data in number of standard deviations (including statistical and systematic errors) for all the distributions used in the fit. Only the dark points enter the fit.

Distribution	χ^2/n_{df}
Tasso (22 GeV)	7.3/13
TPC/2γ (29 GeV)	9.5/12
Mark II (29 GeV)	36.8/14
Tasso (35 GeV)	44.6/13
Cello (35 GeV)	10.6/22
Tasso (44 GeV)	13.6/13
Amy (55 GeV)	7.8/7
Delphi (91.2 GeV)	32.1/22
Aleph all flavours (91.2 GeV)	28.9/23
Aleph uds-enriched (91.2 GeV)	29.7/23
Aleph c-enriched (91.2 GeV)	26.9/23
Aleph b-enriched (91.2 GeV)	66.5/23
Aleph gluons (48 GeV)	2.8/5
Aleph longitudinal (91.2 GeV)	7.8/16

Table 6.3: Detail of the χ^2/n_{df} per experiment in the standard analysis.

region, the contribution to the total χ^2 is only of roughly four units. A change in the normalization of $\approx 2\%$ would make the distribution agree almost perfectly.

The χ^2 per degree of freedom of the fit is 307.3/213. The contributions from each distribution are detailed in table 6.3. The contributions from the ALEPH distributions have to be considered only as approximate since the correlation among them were not considered when extracting their individual value.

As it can be seen in table 6.3, three distributions contribute substantially to the overall χ^2: MARKII (37/14), TASSO at 35 GeV (45/13) and the ALEPH b-enriched sample (66/23). The large χ^2 for the b quark enriched sample is due to inadequacies of the simple parametrization of the fragmentation function. While the simple ansatz is good enough to describe the fragmentation of the gluon and the light quarks including the c quark, it fails to reproduce the detailed structure of b quark fragmentation and decay over the full x range. Removing the high-x points above $x = 0.6$ changes the χ^2/n_{df} to 31/19 while the result of the fit remains unchanged. The relatively high values of the χ^2 for MARKII and TASSO (35 GeV) point to an inconsistency in the experimental data, since there are data from other experiments at the same energies which are perfectly consistent with the QCD fits. In order to understand the importance of those problems for the fit, the errors of these two distributions are scaled up by the corresponding values of $\sqrt{\chi^2/n_{df}}$, effectively deweighting the results from those experiments. The result of the fit with the enlarged errors and the ALEPH b-enriched sample restricted to the range $0.1 < x < 0.6$ is $\alpha_s(M_Z) = 0.127 \pm 0.006$, fully consistent with the previous one, with an overall $\chi^2/n_{df} = 219/209$.

6.7 Systematic errors

The error in $\alpha_s(M_Z)$ presented in the previous section contains the statistical errors and most of the systematic errors from the measurement of the scaled energy distributions. Also the error from the correlations in all the parameters is included in the fit. The only missing uncertainties come from the assumption made in the normalization errors for those experiments in which this is not specified, the dependence of $\alpha_s(M_Z)$ on the assumed flavour composition for the flavour-tagged distributions, and the theoretical errors, which will be estimated by looking at the factorization and renormalization scale dependence of the result.

6.7.1 Experimental systematic errors

Normalization errors. In the low energy experiments where only the combined statistical and systematic errors have been published, the nominal result was obtained with the assumption explained in section 5.7 for the normalization errors. Alternatively, all unspecified errors were taken as bin-to-bin errors giving the result $\alpha_s(M_Z) = 0.1278 \pm 0.0058$. The corresponding shift of $\Delta\alpha_s = 0.002(norm)$ was taken as an additional systematic error.

Flavour composition. By varying the confidence-level cuts in the lifetime tags, the flavour compositions were changed such that the flavour enrichment for uds and b quarks changed by $\pm 4\%$ and for c quarks by -4% and $+2\%$ (it was found to be very difficult to get higher purities). The flavour composition of the different distributions obtained with these changes are specified in table 6.4 where also the purities and flavour composition of the distributions used to make the nominal analysis are shown for comparison. The cuts applied in the two algorithms to construct each distribution are also shown in the table together with the efficiencies. These

Dist. Name	% uds	% c	% b	Efficiency	Cut definition
uds-enr. (stand)	78.9	14.5	6.6	$\epsilon_{uds} = 74.0$	$P_h \geq 0.3$
uds-enr. $(-)$	75.0	16.1	8.9	$\epsilon_{uds} = 91.0$	$P_h \geq 0.1$
uds-enr. $(+)$	82.8	12.5	4.7	$\epsilon_{uds} = 37.8$	$P_h \geq 0.7$
c-enr. (stand)	38.2	35.1	26.7	$\epsilon_c = 9.0$	$0.001 \leq P_h \leq 0.07, l_h \leq 0.2$
c-enr. $(-)$	41.1	31.5	27.4	$\epsilon_c = 15.9$	$0.0005 \leq P_h \leq 0.12, l_h \leq 0.25$
c-enr. $(+)$	35.6	36.9	27.5	$\epsilon_c = 6.2$	$0.001 \leq P_h \leq 0.05, l_h \leq 0.18$
b-enr. (stand)	2.2	7.3	90.5	$\epsilon_b = 32.5$	$P_h \leq 0.001$
b-enr. $(-)$	3.5	9.7	86.8	$\epsilon_b = 39.7$	$P_h \leq 0.003$
b-enr. $(+)$	0.9	3.9	95.2	$\epsilon_b = 21.3$	$P_h \leq 0.0001$

Table 6.4: Flavour composition of the different distributions considered in the analysis. For each distribution, the flavour composition and the efficiency for the flavour to be enriched are shown. Also the cuts applied to the hemispheres for the lifetime tag (P_h) and the event shape tag (l_h) are shown.

Changed distribution	χ^2/n_{df}	$\alpha_s(M_Z)$
uds-enr. $(-)$	303.8/213	0.1253 ± 0.0056
uds-enr. $(+)$	309.1/213	0.1263 ± 0.0054
c-enr. $(-)$	307.1/213	0.1218 ± 0.0055
c-enr. $(+)$	308.9/213	0.1246 ± 0.0055
b-enr. $(-)$	289.2/213	0.1259 ± 0.0054
b-enr. $(+)$	294.8/213	0.1252 ± 0.0053

Table 6.5: Results of $\alpha_s(M_Z)$ for different flavour tagged distributions. For each fit, the tagging cuts of a given distribution are changed, giving the flavour compositions specified in table 6.4. A fit is performed with this new distribution but leaving the rest untouched.

efficiencies do not include the global $\sim 77\%$ of the hadronic selection (section 5.1). Those labeled with 'stand' are the ones that are used in the nominal analysis and the ones with '+' and '$-$' are more enriched and less enriched distributions used in the study of the systematic errors.

The results of the fit changing one of the corresponding enriched flavour distributions at a time are given in table 6.5.

The maximum change was $\Delta\alpha_s = 0.004$, which was taken as an additional systematic error due to flavour composition of the tagged data samples. This result can be confirmed from the extrapolation of the results presented in table 6.6 where

Changed purity	χ^2/n_{df}	$\alpha_s(M_Z)$
uds-enriched $-$	308.9/213	0.1262 ± 0.0054
uds-enriched $+$	308.3/213	0.1251 ± 0.0055
c-enriched $-$	308.2/213	0.1250 ± 0.0055
c-enriched $+$	306.6/213	0.1266 ± 0.0052
b-enriched $-$	308.5/213	0.1247 ± 0.0054
b-enriched $+$	306.4/213	0.1269 ± 0.0053

Table 6.6: Results of $\alpha_s(M_Z)$ for different purities in the tagged distributions. For each fit, the nominal purity taken from the Monte Carlo was changed by $\pm 1\%$. The fits were done with the same nominal distributions but with this 'artificially' changed purity.

the nominal values of the purities were varied artificially by $\pm 1\%$ without changing the distributions themselves. The shifts in $\alpha_s(M_Z)$ were ~ 0.001. Assuming a linear variation of the fitted value of $\alpha_s(M_Z)$ with the variation of the Monte Carlo estimates for the purities, the estimated systematic error would be equivalent to an uncertainty of $\pm 4\%$ in the purity estimates from the Monte Carlo which seems conservative [45, 82].

Considering also the fit error, the total experimental error of $\alpha_s(M_Z)$ is $\Delta\alpha_s(exp) = \pm 0.005(fit) \pm 0.002(norm) \pm 0.004(purity) = \pm 0.007(exp)$.

6.7.2 Theoretical errors

A priori, the scales μ_i, μ_f and μ_R in figure 2.2 are unconstrained. When calculating to all orders in perturbative QCD, any dependence on the choice of the scales vanishes. In finite order perturbation theory, a residual scale dependence is related to the sensitivity to uncalculated higher order terms. In order to avoid large logarithms in the theoretical predictions, the natural choice of scales is $\mu_i^2/s_i = \mu_f^2/s_f = \mu_R^2/\mu^2 = 1$ and these are the values used for the standard analysis. Varying the scales allows to estimate the theoretical uncertainties of the prediction.

The renormalization and factorization scales were parametrized according to $\mu_R = f_R\mu$ and $\mu_{i,f} = f_F\sqrt{s_{i,f}}$, being the nominal value determined by $\ln f_{R,F} = 0$. The scale values were varied, one at a time, in the range $-1 \leq \ln f_{R,F} \leq 1$, giving the values of $\alpha_s(M_Z)$ presented in table 6.7.

Value of the scale	χ^2/n_{df}	$\alpha_s(M_Z)$
$\ln f_R = -1$	307.3/213	0.1242 ± 0.0052
$\ln f_R = +1$	307.3/213	0.1281 ± 0.0056
$\ln f_F = -1$	310.8/213	0.1196 ± 0.0049
$\ln f_F = +1$	304.7/213	0.1310 ± 0.0061

Table 6.7: Results of $\alpha_s(M_Z)$ for different factorization and renormalization scale assumptions. The theoretical errors are taken from the maximum variation in α_s when changing the scale.

The quality of the fit is insensitive to the renormalization scale and does not change substantially with the changes made in the factorization scale. Taking the two scale variations as independent sources of theoretical uncertainties, the theoretical systematic error on $\alpha_s(M_Z)$ will be given by

$$\Delta\alpha_s(theory) = \pm 0.002(\mu_R) \pm 0.006(\mu_F), \tag{6.46}$$

which, combined in quadrature with the experimental error, gives the final result

$$\alpha_s(M_Z) = 0.126 \pm 0.007(exp) \pm 0.006(theory) = 0.126 \pm 0.009. \tag{6.47}$$

6.8 Checks

Several additional checks were carried out in the analysis varying some of the assumed parameters.

6.8.1 Parametrization scale variation

Although there are reasons to choose the parametrization scale at 22 GeV, as explained in section 6.5, repeating the fit with different parametrization points will prove, not only that the value of α_s does not strongly depend on this assumption, but also that the result is not widely sensitive to the choice of the parametrization of the fragmentation functions. This last point comes from the fact that, given the fragmentation functions in the exact form (6.36) at an initial scale $\mu_i = \sqrt{s_0}$, the evolution to a final scale μ_f will transform them to a similar shape which, however, will be outside the original parameter space. Thus varying the parametrization scale is a way to probe slightly different families of functions $D(x)$.

Two different values were tried for the parametrization scale giving the results:

$$\alpha_s(M_Z) = 0.1246 \pm 0.0059 \qquad \text{for} \qquad s_0 = 45.0\,\text{GeV}, \tag{6.48}$$

$$\alpha_s(M_Z) = 0.1240 \pm 0.0063 \qquad \text{for} \qquad s_0 = 91.2\,\text{GeV}, \tag{6.49}$$

which deviate less than 0.002 from the nominal result. The chisquared values differ in less than one unit from the one of the standard fit.

6.8.2 Parametrization of the non-perturbative effects

Although the parametrization of the non-perturbative terms is justified in the Monte Carlo (section 6.4), it is worth to probe the dependence of the result on it.

The energy dependence of the non-perturbative evolution terms was changed from $1/\sqrt{s}$ to $1/s$, as it is known to be in deep-inelastic scattering. The result was $\alpha_s(M_Z) = 0.1265 \pm 0.0052$ in perfect agreement with the nominal result. The value of the χ^2 increased by less than one unit and the value of the non-perturbative parameter changed to $h_0 = -2.7 \pm 2.0$. Thus, the data themselves cannot confirm that the energy dependence of the non-perturbative evolution terms is of the form $1/\sqrt{s}$, but the change in $\alpha_s(M_Z)$ is negligible with the $1/s$ assumption. Anyway, the $1/\sqrt{s}$ assumption is well supported by Monte Carlo studies (section 6.4) and phenomenological theoretical assumptions (section 2.4).

The rescaling ansatz used in reference [20]

$$x = x' \left[1 + h_1 \cdot \left(\frac{1}{\sqrt{s}} - \frac{1}{\sqrt{s_0}} \right) \right] \tag{6.50}$$

was also tried. The fit to all the parameters gave a $\chi^2 = 314.1/213$, and a result of $\alpha_s(M_Z) = 0.108 \pm 0.010$ with a correlation of 87% between α_s and h_1. A value of $h_1 = -1.03 \pm 0.44$ was obtained. This correlation precludes a simultaneous measurement of both parameters. In reference [20], the value of h_1 was estimated from the HERWIG Monte Carlo, giving a value of $h_1 = -0.5$. Fixing this parameter to this value, gave $\alpha_s(M_Z) = 0.1184 \pm 0.0050$, which is compatible with the nominal result although it depends on the assumptions and approximations made in the HERWIG Monte Carlo.

Interval	χ^2/n_{df}	$\alpha_s(M_Z)$	h_0
0.1-0.5	162.4/148	0.1215 ± 0.0071	-0.077 ± 0.108
0.05-0.8	702.2/259	0.1331 ± 0.0036	-0.253 ± 0.084
0.15-0.8	244.7/180	0.1326 ± 0.0100	-0.094 ± 0.169

Table 6.8: Results of the fit to $\alpha_s(M_Z)$ for different intervals in x. All the parameters are fitted.

Interval	χ^2/n_{df}	$\alpha_s(M_Z)$
0.1-0.2	51.9/73	0.1313 ± 0.0040
0.2-0.3	47.8/57	0.1234 ± 0.0073
0.3-0.4	33.9/54	0.1200 ± 0.0078
0.4-0.5	50.1/43	0.1249 ± 0.0075
0.5-0.6	41.1/39	0.1255 ± 0.0075
0.6-0.7	43.5/37	0.1261 ± 0.0075
0.7-0.8	52.8/37	0.1247 ± 0.0088

Table 6.9: Results of the fit to $\alpha_s(M_Z)$ in different intervals in x. All the parameters except $\alpha_s(M_Z)$ are fixed.

6.8.3 Dependence on the fit range

The dependence on the choice of the fit interval was studied by varying the lower and upper bounds of the fit range around the nominal values of $x_{\min} = 0.1$ and $x_{\max} = 0.8$. The results on α_s (shown in table 6.8) are compatible with the nominal result. The χ^2 of the fit degrades considerably when going to smaller $x_{\min}$, indicating that the parametrizations of the fragmentation functions and non-perturbative terms are not suitable for very small x. Going to larger values of $x_{\min}$ amounts to giving up much of the available data, and the fit of all 16 parameters becomes unstable, with correlations of more than 90% between many of the variables.

Finally, the whole parametrization except $\alpha_s(M_Z)$ was fixed to the nominal result, and the strong coupling constant was fitted, using the same formalism as before in independent x intervals of size $\Delta x = 0.1$ between $x = 0.1$ and $x = 0.8$. The different fitted values are shown in table 6.9. All results were found to be statistically compatible with the nominal one, verifying that scaling violations over the full x range are described by one single coupling constant.

Chapter 7

Summary and conclusions

The inclusive distribution $(1/\sigma_{\mathrm{tot}})(d\sigma/dx)$ for charged particles has been measured by the ALEPH experiment for hadronic events of all flavours and enriched samples in light flavours, c quarks and b quarks. In addition, the transverse and longitudinal distributions were measured and, together with information from identified gluon jets, used to constrain the gluon fragmentation function.

A global analysis of these measurements and results from other experiments at lower centre-of-mass energies has been carried out in the framework of next-to-leading order QCD. Scaling violations in the time-like domain between $\sqrt{s} = 22\,\mathrm{GeV}$ and $\sqrt{s} = 91.2\,\mathrm{GeV}$ are observed in agreement with QCD predictions. The data are found to be consistent with one universal coupling constant describing the evolution of the fragmentation functions between $\sqrt{s} = 22\,\mathrm{GeV}$ and $\sqrt{s} = 91.2\,\mathrm{GeV}$. At the same time, the shape of the fragmentation function for gluons, light flavours, c and b quarks were determined from the data alone.

Although the parameters describing the fragmentation functions obtained are strongly correlated, the functional forms of the different fragmentation functions can be used as input to some phenomenological studies.

The size of the power-law corrections, mainly coming from the hadronization effects, have been also extracted from the data and been found to be rather small. Thus, the perturbative evolution of the fragmentation function is the main source of the observed scaling violations.

The strong coupling constant measured here from scaling violations is consistent with other determinations by ALEPH [81] at one fixed energy based on global event shape variables. Expressed at the scale M_Z, the measured value is $\alpha_s(M_Z) = 0.126 \pm 0.009$.

The result is ~ 1.3 standard deviations higher than the value quoted in [80] from the fit to EMC/BCDMS data in the range $0.5 - 260\,\mathrm{GeV}^2$ using the same formalism to extract the value of the strong coupling constant from scaling violations in the space-like domain.

The main single contribution to the error on α_s comes from the dependence on the factorization scale chosen. Next-to-next-to-leading order calculations of the coefficient functions and splitting kernels would decrease this source of error. The overall error is bigger than for some other determinations of the strong coupling constant [73, 81] mainly because all non-perturbative effects (in the value of the fragmentation functions at one energy and in their evolution) have been taken directly from data, without relying on the quantitative predictions of the Monte Carlo models.

In the future, with the data of new e^+e^- machines at higher energies than LEPI, it will be possible to extend this analysis and have a better constrain of the strong coupling constant. In particular, preliminary Monte Carlo studies show that around 6000 hadronic events can be used to construct the scaled-energy inclusive distribution at LEPII with $500\,\mathrm{pb}^{-1}$. However, the improvement in the fit error could be only of the order of 2%. A substantial improvement in the α_s measurement would need even higher energy machines, as the next linear colliders.

Appendix A

Electroweak cross sections

The computation of the scaled energy inclusive distributions from the fragmentation functions needs the knowledge of the electro-weak relative cross sections in order to weight the contribution of different flavour species at each particular energy. This appendix describes the factors that are introduced in formula (2.43).

The flavour weights are defined through

$$w_i(s) = \frac{\sigma_i(s)}{2\sigma_u(s) + 3\sigma_d(s)} \tag{A.1}$$

where it has been taken into account that there are five active favours in the whole energy range used in the analysis.

The relative cross sections $r_i(s)$ are given by the electroweak theory and can be written as

$$\sigma_i(s) = \sigma_i^{(v)}(s) + \sigma_i^{(a)}(s) = \frac{4\pi\alpha^2}{s}\left(r_i^{(v)}(s) + r_i^{(a)}(s)\right) \tag{A.2}$$

$v_e = -\frac{1}{2} + 2s_w^2$	$a_e = -\frac{1}{2}$
$v_u = \frac{1}{2} - \frac{4}{3}s_w^2$	$a_u = \frac{1}{2}$
$v_d = -\frac{1}{2} + \frac{2}{3}s_w^2$	$a_d = -\frac{1}{2}$

Table A.1: Vector and axial couplings for electrons, u- and d-type quarks used in the computation of the relative electroweak cross sections in eq. (A.2).

with

$$r_i^{(v)}(s) = q_i^2 + \frac{s}{(M_Z^2 - s)^2 + M_Z^2\Gamma_Z^2} \cdot \left[2q_i v_e v_i \frac{M_Z^2 - s}{4s_w^2 c_w^2} + (v_e^2 + a_e^2)v_i^2 \frac{s}{16 s_w^4 c_w^4}\right] \tag{A.3}$$

$$r_i^{(a)}(s) = \frac{s}{(M_Z^2 - s)^2 + M_Z^2\Gamma_Z^2}(v_e^2 + a_e^2)(a_i^2)\frac{s}{16 s_w^4 c_w^4} \tag{A.4}$$

where s_w and c_w denote the sine and cosine of the weak mixing angle, q_i the charge of the respective quarks, and the vector and axial couplings for electrons, u quarks and d quarks are given in table A.1.

Figure A.1 plots the relative electroweak cross sections as a function of the centre-of-mass energy. The large variation in the different proportions between low energies and LEP energies can be seen.

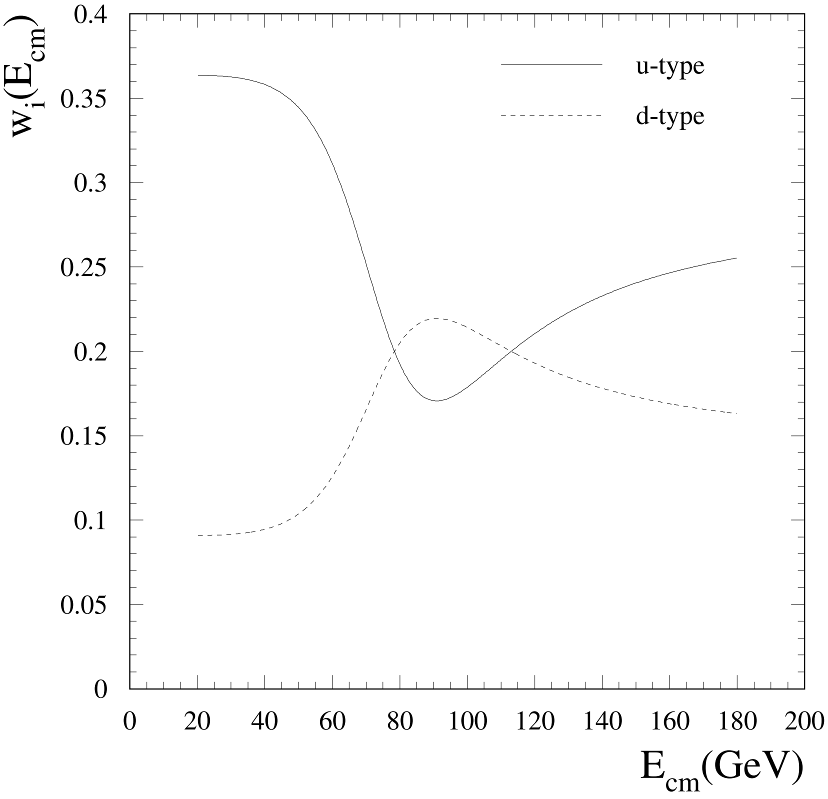

Figure A.1: Relative electroweak cross section as a function of the centre-of-mass energy. The contributions for a u-type quark (continuous line) and a d-type quark (dashed line) are plotted.

Appendix B

Coefficient functions and splitting kernels

This appendix lists a collection of the next-to-leading order formulae necessary for the evaluation of the cross sections from the fragmentation functions, and the calculation of their energy evolution.

B.1 Coefficient functions

This section contains the expressions for the coefficient functions that relate the effective fragmentation functions with the measurable scaled energy cross sections through eq. (2.43). According to reference [76] they are given by

$$
\begin{aligned}
C_g^L(z,\alpha_s(\mu_F),\mu_F^2/s) &= a(\mu_F^2)2\frac{1-z}{z} && \text{(B.1)}\\
C_q^L(z,\alpha_s(\mu_F),\mu_F^2/s) &= a(\mu_F^2) && \text{(B.2)}\\
C_g^T(z,\alpha_s(\mu_F),\mu_F^2/s) &= a(\mu_F^2)\left\{\frac{1+(1-z)^2}{z}\cdot\right. \\
&\quad \left.\cdot\left[\ln(1-z)+2\ln z-\ln\frac{\mu_F^2}{s}\right]-2\frac{1-z}{z}\right\} && \text{(B.3)}\\
C_q^T(z,\alpha_s(\mu_F),\mu_F^2/s) &= \delta(1-z)\left[1+a(\mu_F^2)\left(\frac{2\pi^2}{3}-\frac{9}{2}\right)\right] \\
&\quad -a(\mu_F^2)\ln\frac{\mu_F^2}{s}\left(\frac{1+z^2}{1-z}\right)_{(+)}
\end{aligned}
$$

$$
+a(\mu_F^2)\left[\frac{3}{2}(1-z)-\frac{3}{2}\left(\frac{1}{1-z}\right)_{(+)}\right.
$$
$$
\left.+\,2\frac{1+z^2}{1-z}\ln z+(1+z^2)\left(\frac{\ln(1-z)}{1-z}\right)_{(+)}\right] \quad \text{(B.4)}
$$

where $a(\mu_F^2)$ is the couplant constant defined in eq. (2.12).

The subscript $(+)$ in eq. (B.4) specifies a regularization procedure for the integral over the splitting functions, which are singular at $z=1$, defined as

$$
\int_0^1 dz\,[f(z)]_{(+)}g(z)=\int_0^1 dz\,f(z)\,(g(z)-g(1)) \quad \text{(B.5)}
$$

which, in the usual case that the lower limit of the integral is not 0 but some variable x, translates into

$$
\int_x^1 dz\,[f(z)]_{(+)}g(z)=\int_x^1 dz\;[f(z)(g(z)-g(1))]-g(1)\int_0^x dz\,f(z) \quad \text{(B.6)}
$$

The convolution integrals that are to be performed with the coefficient functions are straightforward, with the exception of the integral over $C_q^T(z)$. After expanding the $(+)$ regularizations one obtains

$$
\begin{aligned}
\int_x^1 dz C_q^T(z,\alpha_s(\mu_F),\mu_F^2/s)D_Q(\frac{x}{z},\mu_F^2) &= D_Q(x,\mu_F^2)(1+a(\mu_F)F_\delta)\\
&\quad +a(\mu_F)\int_x^1 dz\left[D_Q(\frac{x}{z},\mu_F^2)F_R-D_Q(x,\mu_F^2)F_S\right] \quad \text{(B.7)}
\end{aligned}
$$

with

$$
\begin{aligned}
F_\delta &= \frac{2\pi^2}{3}-\frac{9}{2}-\frac{3}{2}\ln(1-x)+\ln^2(1-x)-\ln\frac{\mu_F^2}{s}\left[2\ln(1-x)+\frac{3}{2}\right] && \text{(B.8)}\\
F_R &= \frac{3}{2}(1-z)+\frac{2(1+z^2)}{1-z}\ln z+\frac{1+z^2}{1-z}\left[\ln(1-z)+\ln\frac{\mu_F^2}{s}\right]-\frac{3}{2}\frac{1}{1-z} && \text{(B.9)}\\
F_S &= \frac{2}{1-z}\left[\ln(1-z)+\ln\frac{\mu_F^2}{s}\right]-\frac{3}{2}\frac{1}{1-z} && \text{(B.10)}
\end{aligned}
$$

B.2 Splitting kernels

This sections gives the expressions of the splitting kernels used in the evolution equations (2.46). They are given separately for the non-singlet and singlet parts of the fragmentation functions.

B.2.1 Evolution of flavour non-singlet fragmentation functions

The formulae for the evolution of the non-singlet parts of the fragmentation functions can be found in reference [83]. From there, the NLO splitting function governing the evolution of non-singlet fragmentation functions is obtained as

$$P_N(z, \alpha_s(\mu_R), \mu_R^2/s) = \left[\mathcal{P}^{\mathcal{N}}\right]_{(+)} + a^2(\mu_R) 2\delta(1-z) \int_0^1 dz P^N_{\mathrm{q}\bar{\mathrm{q}}}(z), \tag{B.11}$$

being the expression for $\mathcal{P}^{\mathcal{N}}$

$$\mathcal{P}^{\mathcal{N}} = a(\mu_R) P_{\mathrm{qq}} + a^2(\mu_R^2) \left(P^N_{\mathrm{qq}} + P^N_{\mathrm{q}\bar{\mathrm{q}}} + P_{\mathrm{qq}} b_0 \ln \frac{\mu_R^2}{s} \right) \tag{B.12}$$

where

$$\begin{aligned} P^N_{\mathrm{qq}} &= P_F + X P_G + Z P_n && \text{(B.13)} \\ P^N_{\mathrm{q}\bar{\mathrm{q}}} &= (2 - X) P_A, && \text{(B.14)} \end{aligned}$$

and

$$\begin{aligned} P_F &= 2P_{\mathrm{qq}} \ln z \ln(1-z) + (\frac{3}{1-z} - 3z - 5) \ln z \\ &\quad + (\frac{1+z}{2} - 2P_{\mathrm{qq}}) \ln^2 z - 5(1-z) && \text{(B.15)} \\ P_G &= P_{\mathrm{qq}}(\frac{1}{2}\ln^2 z + \frac{11}{6}\ln z - \frac{\pi^2}{6} + \frac{67}{18}) + (1+z)\ln z + \frac{20}{3}(1-z) && \text{(B.16)} \\ P_n &= -P_{\mathrm{qq}}(\frac{2}{3}\ln z + \frac{10}{9}) - \frac{4}{3}(1-z) && \text{(B.17)} \\ P_A &= S_2 M_{\mathrm{qq}} + (1+z)\ln z + 2(1-z) && \text{(B.18)} \end{aligned}$$

In the above expressions, the values of b_0, X and Z are the ones given in equations (2.26) and (2.12), and a shorthand notation for the first order Altarelli-Parisi splitting kernels

$$\begin{aligned} P_{\mathrm{qq}} \equiv P_{\mathrm{qq}}(z) &= \frac{1+z^2}{1-z} && \text{(B.19)} \\ P_{\mathrm{q}g} \equiv P_{\mathrm{q}g}(z) &= \frac{1+(1-z)^2}{z} && \text{(B.20)} \\ P_{g\mathrm{q}} \equiv P_{g\mathrm{q}}(z) &= z^2 + (1-z)^2 && \text{(B.21)} \\ P_{gg} \equiv P_{gg}(z) &= -z^2 + z - 2 + \frac{1}{z(1-z)} && \text{(B.22)} \end{aligned}$$

was introduced together with the definition

$$M_{ij} \equiv M_{ij}(z) = P_{ij}(-z). \tag{B.23}$$

Also, S_2 was defined as

$$S_2 = -Li_2(\frac{1}{1+z}) + \frac{1}{2}\ln^2 z - \ln^2(1+z) + \frac{\pi^2}{6}, \tag{B.24}$$

where $Li_2(x)$ is the dilogarithm function:

$$Li_2(x) = -\int_0^x \frac{\ln(1-t)}{t}\,dt \;=\; -\int_0^1 \frac{\ln(1-xt)}{t}\,dt \tag{B.25}$$

B.2.2 Evolution of the flavour singlet fragmentation functions

The singlet splitting kernels can be found in reference [84]. The ones coming from the diagonal parts are singular at $z=1$. Thus they are regularized according to

$$\begin{aligned} P_{GG}(z) &= \frac{1}{z}\left[z\hat{P}_{GG}(z)\right]_{(+)} - \delta(1-z)\int_0^1 dy\, y P_{GQ}(y) &\text{(B.26)}\\ P_{QQ}(z) &= \frac{1}{z}\left[z\hat{P}_{QQ}(z)\right]_{(+)} - \delta(1-z)\int_0^1 dy\, y P_{QG}(y) &\text{(B.27)}\end{aligned}$$

which with the definition of the $(+)$ regularization, eq. (B.6), allow to write the evolution equations for the singlet fragmentation functions (eq. (2.50)) as

$$\begin{aligned} s\frac{d}{ds}G(x,s) &= \int_x^1 dz\left\{\hat{P}_{GG}(z)\left[G(\frac{x}{z},s) - zG(x,s)\right]\right.\\ &\quad\left.+P_{GQ}(z)\left[S(\frac{x}{z},s) - zG(x,s)\right]\right\}\\ &\quad-G(x,s)\int_0^x dz\, z\left[\hat{P}_{GG}(z) + P_{GQ}(z)\right] &\text{(B.28)}\\ s\frac{d}{ds}S(x,s) &= \int_x^1 dz\left\{P_{QG}(z)\left[G(\frac{x}{z},s) - zS(x,s)\right]\right.\\ &\quad\left.+\hat{P}_{QQ}(z)\left[S(\frac{x}{z},s) - zS(x,s)\right]\right\}\\ &\quad-S(x,s)\int_0^x dz\, z\left[P_{QG}(z) + \hat{P}_{QQ}(z)\right] &\text{(B.29)}\end{aligned}$$

where only convolution integrals remain. The terms in these evolution equations are given by

$$\hat{P}_{QQ} = a(\mu_R)\,P_{\rm qq} + a^2(\mu_R)\left(R_{\rm qq} + XS_{\rm qq} + ZT_{\rm qq} + P_{\rm qq}b_0\ln\frac{\mu_R^2}{s}\right) \tag{B.30}$$

$$\begin{aligned}
P_{QG} &= a(\mu_R)\,P_{qg} + a^2(\mu_R)\,\left(R_{qg} + XS_{qg} + P_{qg}b_0\ln\frac{\mu_R^2}{s}\right) && \text{(B.31)}\\
P_{GQ} &= a(\mu_R)\,2ZP_{gq}\\
&\quad + a^2(\mu_R)\,\left(ZR_{gq} + ZXS_{gq} + ZZT_{gq} + 2ZP_{gq}b_0\ln\frac{\mu_R^2}{s}\right) && \text{(B.32)}\\
\hat{P}_{GG} &= a(\mu_R)\,2XP_{gg}\\
&\quad + a^2(\mu_R)\,\left(ZR_{gg} + XXS_{gg} + ZXT_{gg} + 2XP_{gg}b_0\ln\frac{\mu_R^2}{s}\right) && \text{(B.33)}
\end{aligned}$$

with the following definitions in the fermion-fermion splitting

$$\begin{aligned}
R_{qq} &= z - 1 - (\frac{3}{2} - \frac{1}{2}z)\ln z + \frac{1+z}{2}\ln^2 z\\
&\quad + P_{qq}\left[\frac{3}{2}\ln z - 2\ln^2 z + 2\ln z\ln(1-z)\right] + 2S_2M_{qq} && \text{(B.34)}\\
S_{qq} &= \frac{14}{3} - \frac{14}{3}z + P_{qq}\left[\frac{11}{6}\ln z + \frac{1}{2}\ln^2 z - \frac{\pi^2}{6} + \frac{67}{18}\right] - S_2M_{qq} && \text{(B.35)}\\
T_{qq} &= -\frac{52}{3} + \frac{28}{3}z + \frac{112}{9}z^2 - \frac{40}{9z} + (2+2z)\ln^2 z\\
&\quad -(10 + 18z + \frac{16}{3}z^2)\ln z - P_{qq}\left[\frac{2}{3}\ln z + \frac{10}{9}\right]. && \text{(B.36)}
\end{aligned}$$

For the fermion-gluon splitting they are

$$\begin{aligned}
R_{qg} &= -\frac{1-z}{2} + 4z - \frac{16-x}{2}\ln z + 2z\ln(1-z) + \frac{2-z}{2}\ln^2 z\\
&\quad + P_{qg}\left[\ln^2(1-z) + 4\ln z\ln(1-z) - 8S_1 - \frac{4\pi^2}{3}\right] && \text{(B.37)}\\
S_{qg} &= S_2M_{qg} + \frac{62}{9} - \frac{35}{18}z + \frac{44}{9}z^2 + (2 + 12z + \frac{8}{3}z^2)\ln z - 2z\ln(1-z)\\
&\quad -(4+x)\ln^2 z + P_{qg}\left[\frac{17}{18} - 2\ln z\ln(1-z) - 3\ln z - \frac{3}{2}\ln^2 z\right.\\
&\quad \left. -\ln^2(1-z) + 8S_1 + \frac{7\pi^2}{6}\right]. && \text{(B.38)}
\end{aligned}$$

The gluon-fermion splitting is described by

$$\begin{aligned}
R_{gq} &= -2 + 3z - (7-8z)\ln z - 4\ln(1-z) + (1-2z)\ln^2 z\\
&\quad -2P_{gq}\left[2\ln z\ln(1-z) + \ln^2 z + \right.\\
&\quad \left.\ln^2(1-z) + \ln(1-z) - \ln z - 8S_1 - \pi^2 + 5\right] && \text{(B.39)}\\
S_{gq} &= 2S_2M_{gq} - \frac{152}{9} + \frac{166}{9}z - \frac{40}{9z} - (\frac{4}{3} + \frac{76}{3}z)\ln z + 4\ln(1-z) + (2+8z)\ln^2 z
\end{aligned}$$

$$
\begin{aligned}
& +P_{gq}\left[\frac{178}{9}+8\ln z\ln(1-z)-\ln^2 z-\frac{4}{3}\ln z\right. \\
& \left.+\frac{10}{3}\ln(1-z)+2\ln^2(1-z)-16S_1-\frac{7\pi^2}{3}\right] \qquad \text{(B.40)} \\
T_{gq} &= -\frac{8}{3}-P_{gq}\left[\frac{16}{9}+\frac{8}{3}\ln z+\frac{8}{3}\ln(1-z)\right], \qquad \text{(B.41)}
\end{aligned}
$$

and the gluon-gluon splitting by

$$
\begin{aligned}
R_{gg} &= -4+12z-\frac{164}{9}z^2+\frac{92}{9z} \\
&\quad +\left[10+14z+\frac{16}{3}(z^2+\frac{1}{z})\right]\ln z+2(1+z)\ln^2 z \qquad \text{(B.42)} \\
S_{gg} &= \frac{27}{2}(1-z)+\frac{134}{18}(z^2-\frac{1}{z})+(\frac{11}{3}-\frac{25}{3}z+\frac{44}{3z})\ln z-4(1+z)\ln^2 z \\
&\quad +P_{gg}\left[4\ln z\ln(1-z)-3\ln^2 z+\frac{22}{3}\ln z-\frac{\pi^2}{3}+\frac{67}{9}\right]+2S_2M_{gg} \qquad \text{(B.43)} \\
T_{gg} &= 2(1-z)+\frac{26}{9}(z^2-\frac{1}{z})-\frac{4}{3}(1+z)\ln z-P_{gg}\left[\frac{20}{9}+\frac{8}{3}\ln z\right]. \qquad \text{(B.44)}
\end{aligned}
$$

In the expressions above S_1 is defined as

$$
S_1=-Li_2(1-z)=\int_0^{1-z}\frac{dx}{x}\ln(1-x) \qquad \text{(B.45)}
$$

and S_2 is given in equation (B.24).

Appendix C

Tables of cross sections

This appendix gives the list of cross sections measured with ALEPH. The scaled energy distribution for all flavours is listed in table C.1. Tables C.2, C.3 and C.4 list the corresponding distributions for light(uds)-, c-, and b-enriched flavours. Table C.5 lists the gluon distribution measured in three jet symmetric events and tables C.6 and C.7 the transverse and longitudinal cross sections.

For all but for the gluon distribution, the bin-to-bin errors are specified. They are separated in statistical and systematic errors. For the systematic errors, the three contributions considered (the limited statistics of the Monte Carlo used for the correction, the selection cut variation and the Monte Carlo model dependence) are listed explicitly. For the gluon distribution only the overall error is given. A 1% normalization error has to be added in quadrature to all distributions except the gluon one.

Interval	$\frac{1}{N_{ev}}\frac{dn^{tr}}{dx}$	E_{stat}	$E_{binsys}(= E_{MCstat} \pm E_{cut} \pm E_{MCmodel})$
0.008–0.012	501.3	0.4	7.8 ($= 0.25$ ± 7.6 ± 1.8)
0.012–0.020	392.69	0.24	0.97 ($= 0.15$ ± 0.48 ± 0.83)
0.020–0.030	274.81	0.18	0.99 ($= 0.11$ ± 0.39 ± 0.91)
0.030–0.040	191.05	0.15	0.48 ($= 0.09$ ± 0.25 ± 0.40)
0.040–0.050	139.94	0.13	0.44 ($= 0.08$ ± 0.19 ± 0.39)
0.050–0.060	107.33	0.11	0.30 ($= 0.07$ ± 0.12 ± 0.27)
0.060–0.070	85.09	0.10	0.17 ($= 0.06$ ± 0.07 ± 0.14)
0.070–0.080	68.96	0.09	0.19 ($= 0.07$ ± 0.06 ± 0.17)
0.080–0.090	56.81	0.08	0.13 ($= 0.05$ ± 0.06 ± 0.11)
0.090–0.100	47.875	0.075	0.095 ($= 0.047$ ± 0.049 ± 0.066)
0.100–0.120	37.655	0.047	0.074 ($= 0.030$ ± 0.036 ± 0.057)
0.120–0.140	28.061	0.041	0.046 ($= 0.026$ ± 0.037 ± 0.013)
0.140–0.160	21.379	0.035	0.054 ($= 0.022$ ± 0.039 ± 0.031)
0.160–0.180	16.661	0.031	0.042 ($= 0.020$ ± 0.030 ± 0.022)
0.180–0.200	13.233	0.028	0.027 ($= 0.018$ ± 0.020 ± 0.004)
0.200–0.225	10.376	0.022	0.023 ($= 0.014$ ± 0.017 ± 0.009)
0.225–0.250	7.928	0.019	0.020 ($= 0.012$ ± 0.007 ± 0.014)
0.250–0.275	6.197	0.017	0.016 ($= 0.011$ ± 0.006 ± 0.011)
0.275–0.300	4.874	0.015	0.012 ($= 0.010$ ± 0.006 ± 0.004)
0.300–0.325	3.862	0.014	0.013 ($= 0.009$ ± 0.003 ± 0.009)
0.325–0.350	3.054	0.012	0.018 ($= 0.008$ ± 0.016 ± 0.003)
0.350–0.375	2.461	0.011	0.009 ($= 0.007$ ± 0.002 ± 0.006)
0.375–0.400	1.995	0.010	0.011 ($= 0.006$ ± 0.007 ± 0.007)
0.400–0.430	1.5555	0.0079	0.0059 ($= 0.0049 \pm 0.0025 \pm 0.0021$)
0.430–0.460	1.2122	0.0070	0.0081 ($= 0.0043 \pm 0.0038 \pm 0.0057$)
0.460–0.490	0.9400	0.0061	0.0051 ($= 0.0038 \pm 0.0031 \pm 0.0014$)
0.490–0.520	0.7346	0.0054	0.0091 ($= 0.0034 \pm 0.0071 \pm 0.0046$)
0.520–0.550	0.5631	0.0047	0.0048 ($= 0.0029 \pm 0.0038 \pm 0.0005$)
0.550–0.600	0.4098	0.0031	0.0025 ($= 0.0019 \pm 0.0015 \pm 0.0008$)
0.600–0.650	0.2572	0.0025	0.0033 ($= 0.0015 \pm 0.0024 \pm 0.0018$)
0.650–0.700	0.1719	0.0020	0.0027 ($= 0.0012 \pm 0.0023 \pm 0.0007$)
0.700–0.750	0.1041	0.0015	0.0026 ($= 0.0009 \pm 0.0023 \pm 0.0007$)
0.750–0.800	0.0606	0.0011	0.0027 ($= 0.0007 \pm 0.0026 \pm 0.0004$)
0.800–0.900	0.0262	0.0005	0.0032 ($= 0.0003 \pm 0.0032 \pm 0.0002$)
0.900–1.000	0.0048	0.0002	0.0020 ($= 0.0001 \pm 0.0020 \pm 0.0001$)

Table C.1: All-flavour inclusive cross section for charged particles measured at $\sqrt{s} = 91.2\,\mathrm{GeV}$. The errors listed are the statistical and systematic bin-to-bin errors. The three sources of systematic uncertainties are specified. A normalization error of 1% has to be added in quadrature everywhere.

Interval	$\frac{1}{N_{ev}}\frac{dn^{tr}}{dx}$	E_{stat}	$E_{binsys}(= E_{MCstat} \pm E_{cut} \pm E_{MCmodel})$
0.008–0.012	492.6	0.4	7.3 (= 0.2 ±7.1 ±1.9)
0.012–0.020	383.1	0.2	1.2 (= 0.1 ±0.8 ±0.9)
0.020–0.030	266.5	0.2	1.2 (= 0.1 ±0.6 ±1.0)
0.030–0.040	184.38	0.15	0.72 (= 0.09 ±0.54 ±0.48)
0.040–0.050	134.60	0.12	0.64 (= 0.08 ±0.42 ±0.47)
0.050–0.060	103.06	0.11	0.46 (= 0.07 ±0.32 ±0.32)
0.060–0.070	81.42	0.10	0.39 (= 0.06 ±0.34 ±0.17)
0.070–0.080	66.11	0.09	0.34 (= 0.05 ±0.27 ±0.20)
0.080–0.090	54.76	0.08	0.20 (= 0.05 ±0.17 ±0.10)
0.090–0.100	46.05	0.07	0.17 (= 0.05 ±0.14 ±0.09)
0.100–0.120	36.50	0.05	0.13 (= 0.03 ±0.11 ±0.07)
0.120–0.140	27.468	0.039	0.074 (= 0.025 ±0.069 ±0.009)
0.140–0.160	21.199	0.035	0.061 (= 0.022 ±0.053 ±0.022)
0.160–0.180	16.730	0.031	0.044 (= 0.019 ±0.031 ±0.024)
0.180–0.200	13.359	0.028	0.035 (= 0.017 ±0.029 ±0.007)
0.200–0.225	10.644	0.022	0.053 (= 0.014 ±0.050 ±0.010)
0.225–0.250	8.249	0.020	0.042 (= 0.012 ±0.037 ±0.016)
0.250–0.275	6.532	0.017	0.037 (= 0.011 ±0.033 ±0.013)
0.275–0.300	5.196	0.016	0.031 (= 0.010 ±0.028 ±0.007)
0.300–0.325	4.136	0.014	0.026 (= 0.009 ±0.023 ±0.009)
0.325–0.350	3.323	0.012	0.030 (= 0.008 ±0.029 ±0.005)
0.350–0.375	2.678	0.011	0.022 (= 0.007 ±0.019 ±0.010)
0.375–0.400	2.190	0.010	0.024 (= 0.006 ±0.022 ±0.009)
0.400–0.430	1.717	0.008	0.018 (= 0.005 ±0.017 ±0.003)
0.430–0.460	1.353	0.007	0.017 (= 0.004 ±0.014 ±0.007)
0.460–0.490	1.0564	0.0064	0.0084 (= 0.0039±0.0072±0.0019)
0.490–0.520	0.8313	0.0057	0.0159 (= 0.0035±0.0143±0.0059)
0.520–0.550	0.6513	0.0050	0.0079 (= 0.0031±0.0072±0.0012)
0.550–0.600	0.4835	0.0033	0.0099 (= 0.0021±0.0096±0.0005)
0.600–0.650	0.3093	0.0026	0.0040 (= 0.0016±0.0027±0.0025)
0.650–0.700	0.2079	0.0021	0.0032 (= 0.0013±0.0027±0.0010)
0.700–0.750	0.1283	0.0017	0.0037 (= 0.0010±0.0034±0.0011)
0.750–0.800	0.0768	0.0012	0.0022 (= 0.0008±0.0020±0.0005)
0.800–0.900	0.0323	0.0006	0.0022 (= 0.0003±0.0022±0.0002)
0.900–1.000	0.0059	0.0002	0.0015 (= 0.0001±0.0015±0.0002)

Table C.2: uds-enriched inclusive cross section for charged particles measured at $\sqrt{s} = 91.2$ GeV. The flavour composition is of 78.9%, 14.5% and 6.6% of uds-, c-, and b-quarks, respectively. The errors listed are the statistical and systematic bin-to-bin errors. The three sources of systematic uncertainties are specified. A normalization error of 1% has to be added in quadrature everywhere.

Interval	$\frac{1}{N_{ev}}\frac{dn^{tr}}{dx}$	E_{stat}	$E_{binsys}(= E_{MCstat} \pm E_{cut} \pm E_{MCmodel})$
0.008–0.012	509.1	1.3	7.5 (= 0.8 ±7.2 ±1.8)
0.012–0.020	397.3	0.8	1.3 (= 0.5 ±1.0 ±0.8)
0.020–0.030	279.0	0.6	1.2 (= 0.3 ±0.7 ±0.9)
0.030–0.040	196.08	0.50	0.67 (= 0.29 ±0.45 ±0.40)
0.040–0.050	143.38	0.42	0.74 (= 0.24 ±0.60 ±0.36)
0.050–0.060	109.81	0.37	0.44 (= 0.21 ±0.26 ±0.28)
0.060–0.070	86.86	0.33	0.30 (= 0.19 ±0.20 ±0.13)
0.070–0.080	70.05	0.29	0.28 (= 0.17 ±0.17 ±0.14)
0.080–0.090	57.84	0.27	0.31 (= 0.15 ±0.24 ±0.13)
0.090–0.100	48.26	0.24	0.20 (= 0.14 ±0.13 ±0.06)
0.100–0.120	37.93	0.15	0.13 (= 0.09 ±0.08 ±0.06)
0.120–0.140	28.63	0.13	0.10 (= 0.08 ±0.07 ±0.02)
0.140–0.160	21.87	0.12	0.10 (= 0.07 ±0.06 ±0.04)
0.160–0.180	16.77	0.10	0.08 (= 0.06 ±0.06 ±0.02)
0.180–0.200	13.322	0.090	0.081 (= 0.053 ±0.058 ±0.019)
0.200–0.225	10.471	0.072	0.051 (= 0.043 ±0.028 ±0.007)
0.225–0.250	7.809	0.062	0.050 (= 0.036 ±0.031 ±0.017)
0.250–0.275	6.059	0.054	0.044 (= 0.032 ±0.027 ±0.013)
0.275–0.300	4.794	0.049	0.053 (= 0.029 ±0.044 ±0.008)
0.300–0.325	3.846	0.043	0.047 (= 0.026 ±0.036 ±0.013)
0.325–0.350	3.089	0.039	0.047 (= 0.024 ±0.040 ±0.007)
0.350–0.375	2.375	0.034	0.030 (= 0.020 ±0.022 ±0.004)
0.375–0.400	1.876	0.031	0.028 (= 0.018 ±0.020 ±0.008)
0.400–0.430	1.436	0.024	0.020 (= 0.014 ±0.014 ±0.001)
0.430–0.460	1.088	0.021	0.017 (= 0.012 ±0.010 ±0.008)
0.460–0.490	0.871	0.019	0.016 (= 0.011 ±0.011 ±0.003)
0.490–0.520	0.656	0.016	0.016 (= 0.010 ±0.012 ±0.004)
0.520–0.550	0.484	0.014	0.010 (= 0.008 ±0.006 ±0.001)
0.550–0.600	0.3479	0.0089	0.0099 (= 0.0053 ±0.0084 ±0.0008)
0.600–0.650	0.2157	0.0070	0.0060 (= 0.0041 ±0.0041 ±0.0017)
0.650–0.700	0.1321	0.0055	0.0050 (= 0.0032 ±0.0037 ±0.0008)
0.700–0.750	0.0900	0.0045	0.0060 (= 0.0028 ±0.0053 ±0.0006)
0.750–0.800	0.0387	0.0028	0.0034 (= 0.0015 ±0.0030 ±0.0003)
0.800–0.900	0.0173	0.0013	0.0013 (= 0.0007 ±0.0010 ±0.0001)
0.900–1.000	0.00324	0.00041	0.00049 (= 0.00022±0.00042±0.00009)

Table C.3: c-enriched inclusive cross section for charged particles measured at $\sqrt{s} = 91.2\,\mathrm{GeV}$. The flavour composition is of 38.2%, 35.1% and 26.7% of uds-, c-, and b-quarks, respectively. The errors listed are the statistical and systematic bin-to-bin errors. The three sources of systematic uncertainties are specified. A normalization error of 1% has to be added in quadrature everywhere.

Interval	$\frac{1}{N_{ev}}\frac{dn^{tr}}{dx}$	E_{stat}	$E_{binsys}(= E_{MCstat} \pm E_{cut} \pm E_{MCmodel})$
0.008–0.012	541.3	1.0	9.2 (= 0.6 ±9.0 ±1.6)
0.012–0.020	435.8	0.6	1.1 (= 0.4 ±0.5 ±0.9)
0.020–0.030	312.3	0.5	1.3 (= 0.3 ±0.8 ±0.9)
0.030–0.040	219.34	0.41	0.54 (= 0.24 ±0.41 ±0.25)
0.040–0.050	161.88	0.35	0.49 (= 0.20 ±0.40 ±0.19)
0.050–0.060	125.34	0.31	0.27 (= 0.18 ±0.12 ±0.15)
0.060–0.070	100.30	0.27	0.34 (= 0.16 ±0.28 ±0.12)
0.070–0.080	80.37	0.24	0.25 (= 0.14 ±0.15 ±0.15)
0.080–0.090	66.11	0.22	0.24 (= 0.13 ±0.08 ±0.19)
0.090–0.100	56.16	0.20	0.15 (= 0.12 ±0.09 ±0.02)
0.100–0.120	42.49	0.12	0.16 (= 0.07 ±0.13 ±0.06)
0.120–0.140	30.29	0.11	0.09 (= 0.06 ±0.05 ±0.04)
0.140–0.160	22.22	0.09	0.11 (= 0.05 ±0.08 ±0.06)
0.160–0.180	16.341	0.078	0.077 (= 0.046 ±0.059 ±0.021)
0.180–0.200	12.173	0.067	0.046 (= 0.039 ±0.017 ±0.016)
0.200–0.225	9.166	0.052	0.037 (= 0.031 ±0.019 ±0.009)
0.225–0.250	6.489	0.044	0.036 (= 0.025 ±0.020 ±0.016)
0.250–0.275	4.869	0.038	0.025 (= 0.022 ±0.010 ±0.007)
0.275–0.300	3.589	0.033	0.034 (= 0.019 ±0.018 ±0.022)
0.300–0.325	2.689	0.028	0.024 (= 0.016 ±0.005 ±0.017)
0.325–0.350	2.069	0.025	0.015 (= 0.014 ±0.005 ±0.002)
0.350–0.375	1.589	0.022	0.021 (= 0.013 ±0.011 ±0.012)
0.375–0.400	1.201	0.019	0.012 (= 0.011 ±0.003 ±0.003)
0.400–0.430	0.880	0.015	0.010 (= 0.008 ±0.004 ±0.003)
0.430–0.460	0.705	0.013	0.013 (= 0.008 ±0.006 ±0.009)
0.460–0.490	0.487	0.011	0.007 (= 0.006 ±0.002 ±0.002)
0.490–0.520	0.3566	0.0093	0.0068 (= 0.0055 ±0.0011 ±0.0038)
0.520–0.550	0.2548	0.0079	0.0081 (= 0.0046 ±0.0067 ±0.0004)
0.550–0.600	0.1543	0.0047	0.0047 (= 0.0027 ±0.0037 ±0.0010)
0.600–0.650	0.0768	0.0033	0.0022 (= 0.0019 ±0.0012 ±0.0003)
0.650–0.700	0.0348	0.0021	0.0022 (= 0.0012 ±0.0018 ±0.0004)
0.700–0.750	0.0164	0.0014	0.0017 (= 0.0008 ±0.0015 ±0.0001)
0.750–0.800	0.0074	0.0009	0.0013 (= 0.0005 ±0.0012 ±0.0002)
0.800–0.900	0.00160	0.00025	0.00023 (= 0.00013±0.00018±0.00006)
0.900–1.000	0.00030	0.00005	0.00009 (= 0.00004±0.00006±0.00003)

Table C.4: b-enriched inclusive cross section for charged particles measured at $\sqrt{s} = 91.2\,\mathrm{GeV}$. The flavour composition is of 2.2%, 7.3% and 90.5% of uds-, c-, and b-quarks, respectively. The errors listed are the statistical and systematic bin-to-bin errors. The three sources of systematic uncertainties are specified. A normalization error of 1 % has to be added in quadrature everywhere.

Interval	$\frac{1}{N_{ev}}\frac{dn^{tr}}{dx}$	Error
0.05–0.10	40.22	1.46
0.10–0.15	16.87	0.91
0.15–0.25	6.87	0.47
0.25–0.35	1.86	0.19
0.35–0.55	0.40	0.09
0.55–0.80	0.04	0.03

Table C.5: Gluon scaled energy distribution measured in three jet symmetric events [65].

Interval	$\frac{1}{N_{ev}}\frac{dn^{tr}}{dx}$	E_{stat}	$E_{binsys}(= E_{MCstat} \pm E_{cut} \pm E_{MCmodel})$
0.008–0.012	377.2	0.9	52.5 (= 0.5 ±34.0 ±40.0)
0.012–0.020	314.9	0.5	4.4 (= 0.3 ± 4.4 ± 0.7)
0.020–0.030	234.5	0.4	2.4 (= 0.2 ± 2.0 ± 1.2)
0.030–0.040	170.1	0.3	1.0 (= 0.2 ± 0.8 ± 0.6)
0.040–0.050	127.50	0.25	0.72 (= 0.15 ± 0.57 ± 0.42)
0.050–0.060	99.29	0.22	0.61 (= 0.13 ± 0.44 ± 0.40)
0.060–0.070	79.61	0.19	0.60 (= 0.12 ± 0.43 ± 0.40)
0.070–0.080	65.23	0.17	0.42 (= 0.11 ± 0.34 ± 0.22)
0.080–0.090	54.09	0.16	0.39 (= 0.10 ± 0.17 ± 0.33)
0.090–0.100	45.72	0.14	0.23 (= 0.09 ± 0.16 ± 0.15)
0.100–0.120	36.22	0.09	0.16 (= 0.06 ± 0.11 ± 0.09)
0.120–0.140	27.12	0.08	0.31 (= 0.05 ± 0.29 ± 0.09)
0.140–0.160	20.77	0.07	0.11 (= 0.04 ± 0.09 ± 0.02)
0.160–0.180	16.32	0.06	0.16 (= 0.04 ± 0.15 ± 0.04)
0.180–0.225	11.323	0.033	0.089 (= 0.021 ± 0.083 ± 0.026)
0.225–0.275	6.943	0.025	0.055 (= 0.015 ± 0.052 ± 0.011)
0.275–0.325	4.319	0.020	0.027 (= 0.012 ± 0.023 ± 0.008)
0.325–0.400	2.474	0.012	0.018 (= 0.008 ± 0.015 ± 0.008)
0.400–0.600	0.8439	0.0043	0.0068 (= 0.0027± 0.0056± 0.0027)
0.600–0.800	0.1516	0.0018	0.0067 (= 0.0011± 0.0065± 0.0014)
0.800–1.000	0.0175	0.0005	0.0057 (= 0.0003± 0.0057± 0.0004)

Table C.6: Transverse inclusive cross section for charged particles measured at $\sqrt{s} = 91.2\,\mathrm{GeV}$. The errors listed are the statistical and systematic bin-to-bin errors. The three sources of systematic uncertainties are specified. A normalization error of 1% has to be added in quadrature everywhere.

Interval	$\frac{1}{N_{ev}}\frac{dn^{tr}}{dx}$	E_{stat}	$E_{binsys}(= E_{MCstat} \pm E_{cut} \pm E_{MCmodel})$
0.008–0.012	123.6	0.5	16.4 (= 0.4 ±3.1 ±16.1)
0.012–0.020	77.2	0.3	2.8 (= 0.2 ±2.3 ± 1.5)
0.020–0.030	40.6	0.2	1.6 (= 0.1 ±0.8 ± 1.4)
0.030–0.040	21.1	0.1	1.2 (= 0.1 ±0.2 ± 1.1)
0.040–0.050	12.42	0.12	0.81 (= 0.09 ±0.13 ± 0.80)
0.050–0.060	8.00	0.10	0.58 (= 0.08 ±0.15 ± 0.55)
0.060–0.070	5.40	0.09	0.40 (= 0.07 ±0.08 ± 0.39)
0.070–0.080	3.81	0.08	0.31 (= 0.06 ±0.09 ± 0.29)
0.080–0.090	2.74	0.07	0.20 (= 0.05 ±0.05 ± 0.18)
0.090–0.100	2.14	0.06	0.20 (= 0.05 ±0.08 ± 0.17)
0.100–0.120	1.43	0.04	0.14 (= 0.03 ±0.04 ± 0.13)
0.120–0.140	0.90	0.03	0.10 (= 0.03 ±0.07 ± 0.07)
0.140–0.160	0.569	0.026	0.060 (= 0.022 ±0.021 ± 0.052)
0.160–0.180	0.393	0.024	0.082 (= 0.018 ±0.068 ± 0.042)
0.180–0.225	0.259	0.012	0.037 (= 0.012 ±0.025 ± 0.025)
0.225–0.275	0.115	0.008	0.024 (= 0.008 ±0.015 ± 0.018)
0.275–0.325	0.055	0.005	0.013 (= 0.005 ±0.011 ± 0.006)
0.325–0.400	0.0293	0.0032	0.0076 (= 0.0034 ±0.0058 ± 0.0040)
0.400–0.600	0.0067	0.0007	0.0023 (= 0.0012 ±0.0008 ± 0.0017)
0.600–0.800	0.00041	0.00020	0.00094 (= 0.00033±0.00087± 0.00008)
0.800–1.000	−0.0002	0.0002	0.0011 (= 0.0002 ±0.0011 ± 0.00003)

Table C.7: Longitudinal inclusive cross section for charged particles measured at $\sqrt{s}$ = 91.2 GeV. The errors listed are the statistical and systematic bin-to-bin errors. The three sources of systematic uncertainties are specified. A normalization error of 1% has to be added in quadrature everywhere.

Bibliography

[1] M. Gell-Mann, Act. Phys. Austriaca Suppl. IX (1972) 733;
H. Fritzsch, M. Gell-Mann and H. Leutwyler, Phys. Lett. B47 (1973) 365;
D. J. Gross and F. Wilczek, Phys. Rev. D8 (1973) 3633.

[2] S. L. Glashow, Nucl. Phys. B22 (1961) 579.
S. Weinberg, Phys. Rev. Lett. 19 (1967) 1264.
A. Salam, *Elementary Particle Theory*, ed. N. Svartholm, Almqvist and Wiksell, Stockholm (1968) 367.
S. L. Glashow, J. Iliopoulos and L. Maiani, Phys. Rev. D2 (1970) 1285.

[3] M. Gell-Mann, Phys. Lett. 8 (1964) 214;
G. Zweig, CERN-TH-401 and CERN-TH-412 (1964).

[4] R. P. Feynman, *Photon-Hadron Interactions*, Benjamin, New York (1972).

[5] E. D. Bloom *et al.*, Phys. Rev. Lett. 23 (1969) 930;
J. L. Friedman, Rev. Mod. Phys. 63 (1991) 615.

[6] M. Y. Han and Y. Nambu, Phys. Rev. B139 (1965) 1006.

[7] L. Montanet *et al.*, Phys. Rev. D50 (1994) 1173.

[8] L. Montanet *et al.*, Phys. Rev. D50 (1994) 1334;
G. d'Agostini, W. de Boer and G. Grindhammer, Phys. Lett. B229 (1989) 160.

[9] S. Weinberg, Phys. Rev. D8 (1973) 4482.

[10] D. J. Gross and F. Wilczek, Phys. Rev. D8 (1973) 3633;
H. D. Politzer, Phys. Rev. Lett. 30 (1973) 1346.

[11] R. D. Field, *Applications of Perturbative QCD*, Addison-Wesley Publishing Company, Redwood City (USA) (1989).

[12] ALEPH Collaboration, contributed Paper to ICHEP94, Glasgow, 20-27 July 1994, Ref. 0546;
D. Decamp *et al.*, ALEPH Collaboration, Phys. Lett. B284 (1992) 151;
P. Abreu *et al.*, DELPHI Collaboration, Z. Phys. C59 (1993) 357;
B. Adeva *et al.*, L3 Collaboration, Phys. Lett. B248 (1990) 227;
R. Akers *et al.*, OPAL Collaboration, Z. Phys. C65 (1995) 367.

[13] W. Pauli and F. Villars, Rev. Mod. Phys. 21 (1949) 434
G. t'Hooft and M. Veltmant, Nucl. Phys. B44 (1972) 189.

[14] N. N. Bogolinbov and O. S. Parasink, Acta. Math. 97 (1957) 227.

[15] K. G. Chetyrkin, J. H. Kühn, A. Kwiatkowsky, CERN 95-03.

[16] S. A. Lavin and J. A. M. Vermasseren, Phys. Lett. B303 (1993) 334.

[17] G. Altarelli, Phys. Rep. 81 (1982) 1.

[18] W. Celmaster and R. Gonsalves, Phys. Rev. Lett. 44 (1980) 560;
S. G. Gorishny, A. L. Kataev and S. A. Larin, Phys. Lett. B259 (1991) 144.

[19] V. N. Gribov and L. N. Lipatov, Sov. J. Nucl. Phys. 15 (1972) 78;
G. Altarelli, G. Parisi, Nucl. Phys. B126 (1977) 298;
Yu. L. Dokshitzer, Sov. Phys. JETP 46 (1977) 641.

[20] P. Nason and B. Webber, Nucl. Phys. B421 (1994) 473.

[21] E. G. M. Soldate, Nucl. Phys. B223 (1983) 61;
J. F. Gunion *et al.*, Phys. Rev. D29 (1984) 2491.

[22] R. Akrhoury and V. I. Zakharow, UM-TH-95-12 (1995).

[23] B. R. Webber, Phys. Lett. B339 (1994) 148.

[24] D. Decamp *et al.*, ALEPH Collaboration, Nucl. Inst. and Meth. A294 (1990) 121.

[25] W. Blum (ed.), *The ALEPH Handbook*, ALEPH internal report, ALEPH 89-77 (1989).

[26] P. Aarnio *et al.*, DELPHI Collaboration, Nucl. Inst. and Meth. A303 (1991) 233.

[27] B. Adeva *et al.*, L3 Collaboration, Nucl. Inst. and Meth. A289 (1991) 35.

[28] K. Ahmet *et al.*, OPAL Collaboration, Nucl. Inst. and Meth. A305 (1991) 275.

[29] *LEP Design Report*, CERN-LEP/84-01 (1984).

[30] P. Mató, *Data Processing for Large e^+e^- Experiments*, Ph.D. thesis, Univ. of Barcelona (1990).

[31] M. Delfino *et al.*, Comp. Phys. Comm. 57 (1989) 401.

[32] J. Knobloch, *JULIA Users and Programmers guide*, ALEPH internal report, ALEPH 90-11 (1990).

[33] G. Batignani *et al.*, Nucl. Phys. B23 (Proc.Suppl.) (1991) 291.

[34] R. Settles, *ALEPH in 1991*, ALEPH internal report, ALEPH 92-68 (1992).

[35] D. Buskulic *et al.*, (ALEPH Collaboration), Nucl. Inst. and Meth. A360 (1995) 481.

[36] G. J. Barber *et al.*, Nucl. Inst. and Meth. A279 (1989) 212.

[37] W. B. Atwood *et al.*, Nucl. Inst. and Meth. A306 (1991) 446.

[38] P. Némethy *et al.*, Nucl. Inst. and Meth. A297 (1983) 273.

[39] W. Witzeling *et al.*, *dE/dX - Recent Results from TPC*, Contribution to the V International Conference on Colliding Beam Detectors, Novosibirsk, Russia (1990).

[40] H. Videau, *The ALEPH Pictorial Electromagnetic Calorimeter - A High Granularity Gaseous Calorimeter Operated in a High Magnetic Field*, Invited talk at the 2nd Pisa Meeting on advanced detectors, Castiglione, Italy, June 1983.

[41] J. Knobloch and P. Norton (eds.), *Status of Reconstruction Algorithms for ALEPH. Version 3*, ALEPH internal report.

[42] I. R. Tomalin, *Track Finding Efficiency in the Central Detector*, ALEPH internal report, ALEPH 89-135 (1989).

[43] W. Wiedenmann, *Tracking with the ALEPH Time Projection Chamber*, Paper presented at the IEEE Nucl. Sci. Symp., Arlington, VA, (1990).

[44] R. Frühwirth, HEPHY-PUB 503/87 (1987).

[45] D. Brown and M. Frank, ALEPH internal note, ALEPH 92-135.

[46] D. Buskulic *et al.*(ALEPH Collaboration), Phys. Lett. B313 (1993) 549.

[47] S. Jadach *et al.*, *Z Physics at LEP I*, G. Altarelli, R. Kleiss and C. Verzegnassi (eds.), CERN/89-08, Vol. 3 (1989) 69.

[48] M. Böhm, A. Denner and W. Hollik, Nucl. Phys. B304 (1988) 687.
F.A. Berends, R. Kleiss and W. Hollik, Nucl. Phys. B304 (1988) 712.

[49] T. Sjostrand, LU TP 85-10.

[50] J. E. Campagne and R. Zitoun, Z. Phys. C43 (1989) 469.

[51] F. A. Berends *et al.*, Phys. Lett. B148 (1984) 489.

[52] F. A. Berends *et al.*, Nucl. Phys. B253 (1985) 421.

[53] B. Bloch-Devaux *et al.*, *KINGAL Users Guide*, ALEPH internal report, ALEPH 87-53 (1988).

[54] R. Brun *et al.*, *GEANT3 Users Guide*, CERN-DD/EE/84-1 (1987).

[55] F. Ranjard, *GALEPH-Monte Carlo program for ALEPH*, ALEPH internal report, ALEPH 88-119 (1988).

[56] H. Fesefeldt, *GHEISHA*, Aachen 3rd Inst. Nucl. Phys. A23 (Proc. Suppl.) (1991) 291.

[57] T. Sjostrand, Comp. Phys. Comm. 39 (1986) 347.

[58] B. Anderson, G. Gustafson, G. Ingelman and T. Sjostrand, Phys. Rep. 97 (1983) 31.

[59] C. Peterson, D. Schlatter, I. Schmitt, P. Zerwas, Phys. Rev. D27 (1984) 105.

[60] T. Sjostrand and M. Bengtsson, Comp. Phys. Comm. 43 (1987) 367;
M. Bengtsson and T. Sjostrand, Phys. Lett. B185 (1987) 435;
M. Bengtsson and T. Sjostrand, Nucl. Phys. B289 (1987) 810.

[61] K. Kato and T. Munehisa, Phys. Rev. D36 (1987) 61;
K. Kato and T. Munehisa, Comp. Phys. Comm. 64 (1991) 67.

[62] G. Marchesini and B. R. Webber, Nucl. Phys. B310 (1988) 461;
I. G. Knowles, Nucl. Phys. B310 (1988) 571;
G. Marchesini *et al.*, Comp. Phys. Comm. 67 (1992) 465.

[63] U. Petterson, LU TP 88-5;
L. Lönnblad and U. Petterson, LU TP 88-15;
L. Lönnblad, LU TP 91-11.

[64] D. Buskulic *et al.* ALEPH Collaboration, Phys. Lett. B313 (1993) 535.

[65] D. Buskulic *et al.* ALEPH Collaboration, *Quark-Gluon Jet Properties with a Lifetime Tag in ALEPH*, contribution to the 27th Intl. Conf. on High Energy Physics, Glasgow, Scotland, July 1994 (Ref. GLS0539).

[66] R. Akers *et al.* OPAL Collaboration, CERN/PPE-95-57

[67] D. Decamp *et al.*, ALEPH Collaboration, Phys. Lett. B273 (1991) 181.

[68] W. Braunschweig *et al.*, TASSO Collaboration, Z. Phys. C47 (1990)187.

[69] A. Petersen *et al.*, MARK II Collaboration, Phys. Rev. D37 (1988) 1.

[70] G. D. Cowan, TPC/2γ Collaboration. internal note TPC-LBL-94-01,

[71] O. Podobrin, CELLO Collaboration, Ph.D. thesis Universität Karlsruhe.

[72] Y. K. Li *et al.*, AMY Collaboration, Phys. Rev. D41 (1990) 2675.

[73] P. Abreu *et al.*, DELPHI Collaboration, Phys. Lett. B311 (1993) 408.

[74] M. Schmeling, *Analysis of scaling violations in fragmentation functions*, ALEPH internal report, ALEPH 94-96.

[75] W. H. Press, B. P. Flannery, S. A. Teukolsky and W. T. Vetterling, *Numerical Recipes* , Cambridge University Press, 1989.

[76] G. Altarelli, R. K. Ellis, G. Martinelli and So-Young Pi, Nucl. Phys. B160 (1979) 301.

[77] Yu. L. Dokshitzer, V. A. Khoze, A. H. Mueller and S. I. Troyan, *Basics of Perturbative QCD*, Editions Frontières, Gif-sur-Yvette (France), 1991; and references therein.

[78] Ya. I. Azimov, Yu. L. Dokshitzer, V. A. Khoze and S. I. Troyan, Z. Phys. C27 (1985) 65.

[79] C. P. Fong and B. R. Webber, Nucl. Phys. B355 (1991) 54.

[80] M. Virchaux and A. Milsztajn, Phys. Lett. B274 (1992) 221.

[81] D. Decamp *et al.*, ALEPH Collaboration, Phys. Lett. B284 (1992) 163; Phys. Lett. B255 (1991) 623; Phys. Lett. B257 (1991) 479.

[82] E. Martin, *Measurement of heavy flavours leptons'b purity*, ALEPH internal report, ALEPH 94-157 (1994).

[83] G. Gurci, W. Furmanski and R. Petronzio, Nucl. Phys. B175 (1980) 27.

[84] W. Furmanski and R. Petronzio, CERN-TH 2933 (1980);
W. Furmanski and R. Petronzio, Phys. Lett. B97 (1980) 437.